Ultrafast electron dynamics in chemically doped complex materials analyzed by time-resolved photoemission spectroscopy

Von der Fakultät für Physik
der Universität Duisburg-Essen genehmigte

Doktorarbeit

zur Erlangung des akademischen Grades eines Doktors der
Naturwissenschaft
(Dr. rer. nat.)

von
Isabella Avigo
aus Brescia, IT

Referent: Prof. Dr. Uwe Bovensiepen
Korreferent 1: Prof. Dr. Kai Rossnagel
Korreferent 2: Prof. Dr. Axel Lorke

Prüfer: apl. Prof. Dr. Hermann Nienhaus

Vorsitzender des Prüfungsausschusses: Prof. Dr. Ralf Schützhold

Tag der mündlichen Prüfung: 31. August 2017

Hiermit erkläre ich,

- dass ich die eingereichte Dissertation selbstständig verfasst habe.
- dass ich die Erlangung des akademischen Grads eines Doktors der Naturwissenschaften (Dr. rer. nat.) anstrebe.
- dass ich nur die angegebenen Hilfsmittel verwendet habe und alle wörtlich oder inhaltlich überernommenen Stellen als solche kenntlich gemacht habe.
- dass die vorliegende Arbeit wurde weder im Aus- noch im Inland in gleicher oder ähnlicher Form einer anderen Prüfungsbehörde vorgelegt wurde.

Duisburg, März 2017

Kurzfassung

Komplexe Materialien, in denen elektronische Korrelationen eine Schlsselrolle in dem reichhaltigen Zusammenspiel der verschiedenen mikroskopischen Freiheitsgraden spielen, sind von wesentlicher wissenschaftlicher und technischer Bedeutung, da sie oftmals neuartige und/oder exotische Eigenschaften besitzen. Ein vielversprechender Ansatz zur Untersuchung dieses komplexen Zusammenspiels ist die Untersuchung von Nichtgleichgewichtszuständen und deren Relaxation in der Zeitdomäne, da unterschiedliche Kopplungskanäle Signaturen auf unterscheidbaren, femto- bis pikosekunden Zeitskalen aufweisen können. In der vorliegenden Arbeit wird die ultraschnelle elektronische Dynamik zweier komplexer, chemisch dotierter Modellsysteme mit Hilfe von femtosekunden zeit- und winkelaufgelöster Photoemission (trARPES) direkt in der Zeitdomäne untersucht.

Co-dotiertes $BaFe_2As_2$ gehört zu der Familie der vor kurzem entdeckten Fe-basierten Hochtemperatursupraleiter. Ein Verständnis der mikroskopischen Ursachen der elektronischen Phasen in derartigen Materialien ist wichtig, um die Mechanismen der Hochtemperatursupraleitung zu verstehen. Die ultraschnelle Relaxation heißer Elektronen wird für drei verschiedene Co-dotierungen und oberhalb der antiferromagnetischen Übergangstemperatur untersucht. Der wichtigste Befund ist die Signatur einer Kopplung des elektronischen Systems an eine bosonische Anregung, die sich bei allen drei Dotierungen in einem fluenzabhängigen Sprung der Relaxationsraten bei der Energie $E - E_F = 200\,\mathrm{meV}$ äußert. Aufgrund der energetischen Position dieser Signatur und durch Vergleich mit Ergebnissen von Neutronenstreuexperimenten wird ein magnetischer Ursprung dieses Bosons nahegelegt.

Eine systematische temperatur- und fluenzabhängige Untersuchung zur Charakterisierung des transienten, photo-induzierten Zustandes wird an $1T$-TaS_2 durchgeführt; ein Material, in dem gleichermaßen starke e-e- und e-ph Kopplung präsent sind. Der Hauptbefund ist die Beobachtung einer transienten Doppelbesetzung von Zuständen, dem “upper Hubbard band” (UHB), in der isolierenden Mott-Phase. Aus der Auswertung des zeitlichen Verhaltens wird die relevante Zeitskala für photo-induzierte Unordnung und der anschließenden Dynamik im elektronischen Subsystem zu einem oder mehreren ”hopping cycles” bestimmt. Während Elektron-Phonon-Wechselwirkung eine wichtige Rolle spielt und als Energieverlustkanal für das angeregte Elektronensystem auf langen Zeitskalen dient, ist die Dynamik, Thermalisierung von Ladungsträgern im UHB und der anschließende Zerfall der Besetzung nicht auf eine derartige Kopplung angewiesen. Es wird geschlussfolgert, dass das elektronische und phononische Subsystem in frühen Zeiten nach der Anregung entkoppelt sind, was zu einer Reduzierung der Komplexität theoretischer Modellierungen führt. Zudem wird über erste Photoemissionsexperimente zur Erzeugung und Untersuchung der statischen und dynamische Eigenschaften des metastablien ”hidden states” berichtet.

Für beide Modellsysteme ist der Ansatz in der Zeitdomäne essentiell, um physikalische Eigenschaften aufzudecken, die unter Gleichgewichtsbedingungen nicht zugänglich sind.

Abstract

Complex materials, in which electron correlations play a key role in favoring a rich interplay among the various microscopic electronic, structural and magnetic degrees of freedom, are of deep scientific and technological interest as they often lead to the appearance of novel, exotic phases. One promising approach to investigate this complex interplay is the study of non-equilibrium states and their relaxation in the time domain, since signatures of different coupling channels can result on distinguishable femto- to picosecond timescales. In the present work the ultrafast electron dynamics of two complex, chemically doped model systems are investigated by means of time- and angle-resolved photoemission spectroscopy (trARPES) on femtosecond timescales directly in the time-domain.

Co-doped $BaFe_2As_2$ belongs to the family of the newly discovered Fe-based high-T_c superconductors and understanding the microscopic origins of electronic phases in such materials is important for elucidating the mechanism of high-T_c superconductivity. The ultrafast relaxation of the excited hot electron populations was investigated for systems with three different Co-contents and above the antiferromagnetic transition temperature. The major findings is the signature of the coupling of the electronic system to a bosonic excitation that manifests itself in a fluence-dependent step occurring in the relaxation rates at the same energy of $E - E_F = 200\,\mathrm{meV}$ for all dopings. Due to the energetic position of such a feature and after comparison with neutron scattering experiments in literature, the magnetic origin of such a boson was suggested.

A systematic temperature- and fluence-dependent study was performed on $1T$-TaS_2, in which simultaneously strong electron-electron (e-e) and electron phonon (e-ph) interaction are present, aiming at the characterization of the photoinduced state. The major finding is the observation of a transient population of doubly occupied states in the Mott-insulating phase, that is, the upper Hubbard band (UHB). From the analysis of its temporal evolution, the relevant timescales for photo-induced disorder and the subsequent dynamics in the electronic subsystem could be estimated to be of the order of the hopping cycle. While electron-phonon coupling plays a significant role and serves as an energetic loss channel for the excited electronic system on longer time scales, the dynamics, thermalization of carriers in the UHB and subsequent decay of its occupation do not require such coupling. It was concluded that the electronic and phononic subsystem are decoupled at early times after photo perturbation, which lead to a consistent reduction of complexity in the theoretical modeling. Finally a first photoemission experiment aiming at reaching the metastable hidden state and investigating its properties looking directly at both static and dynamical changes in the electronic structure is reported.

For both model systems, the time domain approach was crucial to unveil physical properties that wouldn't have been accessible under equilibrium conditions.

Contents

Chapter 1

Introduction

Complex materials

The matter shaping our world is formed by many interacting particles and understanding the microscopic behavior of different materials is at the core of science's philosophy and key condition for technological progress. While scientists succeeded in describing most of the fundamental properties of certain materials like conventional metals, semiconductors, band insulators and semimetals, there are other classes of materials which properties are still far from being understood. Such materials are "complex", in the sense that they exhibit a rich (and indeed complex) interplay among the microscopic electronic, orbital, structural and magnetic degrees of freedom, often leading to the emergence of new and intriguing properties such as high-temperature superconductivity, magnetism, emergence of broken symmetry ground states or orbitally ordered states. The result is a competition (sometimes even a co-existence) between distinct ground states, with different symmetries and low energy excitations. New phases often appear near quantum phase transitions, when tuning a parameter such as carriers density, pressure, or when magnetic field tips the balance between one energy scale and one of its competitors. These phases can have surprising and useful properties and the transitions between such phases can have technologically relevant features, such as orders-of-magnitude changes in electrical conductivity (i.e. metal-insulator transitions), perhaps tuned by magnetic field (i.e. colossal magnetoresistance).

One of the key points for the emergence of such novel phenomena is the degree of the electron-electron interaction strength and at such cusps in behavior, strong correlations can act as a sort of lever arm, through which small changes in controllable parameters can have dramatic consequences on material properties [2]. On the other hand, electron correlations are also responsible for the difficulties encountered when studying these systems, due to the no longer applicability of established single particle band theo-

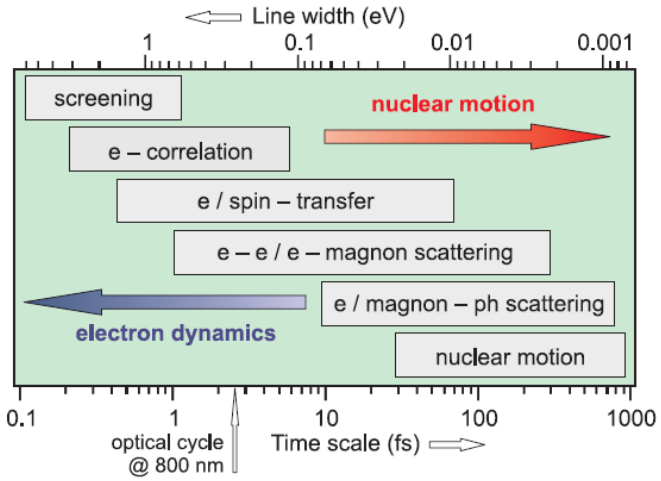

Figure 1.1: Typical time scales and respective line widths of elementary excitations and processes in solid materials. While the various electronic processes cover the full sub-picosecond range and reach far into the attosecond range, dephasing and decay of ion core vibration is limited to timescales faster than several tens of fs, dependent on the atomic mass. From [1]

ries. Therefore, joint efforts among different approaches in experiment and theory that can complement each other are absolutely necessary. With the fast developing experimental, theoretical and material growth techniques, the possibility of being able to understand, predict, engineer, and control materials with desired electronic properties and tunable transitions between various phases is becoming more and more promising.

Time-resolved spectroscopy

If we think, for instance, to device manufacturing, any process that involves a directed change of material properties is characterized by a non-equilibrium starting point and its dynamical evolution towards a ground state. Thus, a deeper understanding of and a proper theoretical description for the non-equilibrium properties and the related dynamical processes are crucial for expanding our understanding of the physics and predict the behavior of complex systems, which might lead to the development of novel materials. In general, the dynamical processes as well as emergent properties such as new ground states of broken symmetry are governed by the interplay of the various elementary interactions of the conduction electrons present in a solid, which occur on intrinsically different energy and time scales, determined by the strength of the respective force. In the case of complex matter, where many simultaneously strong interactions between different microscopic degrees of freedom are present, it is difficult to disentangle the various contributions in the energy domain, close to equilibrium, as they are mostly present

all the time. Interactions quite generally give rise to a finite quasiparticle lifetime, or equivalently an excitation energy line width and a related band renormalization. Some examples of the typical time scales and respective line widths of different processes occurring in solid materials are shown in figure 1.1. Such quantities can in some cases be directly measured using, for instance, angle-resolved photoemission spectroscopy (ARPES) [3, 4, 5, 6] by studying the line width $\Gamma(E)$ or effective dispersion $E(k)$, obtaining the imaginary or real parts of the self-energy, respectively. In contrast, the investigation of systems far from equilibrium and of the dynamics following optical excitation provides a way to separate different interactions owing to their different intrinsic time scales. This requires the use of proper methods of investigation, as time-resolved spectroscopies. Figure 1.1 suggests that ultrafast time-resolved spectroscopic techniques are particularly useful for the investigation of complex materials, because they deliver direct dynamical information at the fundamental time scale of elementary electronic processes [7, 1]. They allow to determine the nature and strength of the interactions between the coupled underlying degrees of freedom, to identify the dominant interactions and thus to gain important insights into ground-state properties [8, 9, 10]. In addition to that femtosecond time-resolved spectroscopies enable to unearth fascinating effects, which do not exist at equilibrium, and possibly reveal novel hidden states [11, 12, 13, 14].
In this work, femtosecond time- and angle-resolved photoemission spectroscopy (trARPES) is used, which combines the direct access to the electronic structure in momentum space with the non-equilibrium regime. With this technique, the system is photoexcited by femtosecond laser pulses and subsequently probed with time-delayed UV or XUV pulses, analyzing the ultrafast changes in the electronic structure and the relaxation dynamics. We will report on our trARPES studies of the non-equilibrium properties of two complex materials, that we introduce here below.

Investigated Model systems

1*T*-TaS_2 belongs to the family of layered transition metal dichalcogenides which, due to their reduced electronic dimensionality, are prone to electronic instabilities and therefore exhibit a wide diversity of ordered ground states and metal-insulator transitions, providing an ideal playground to explore how various ordering processes emerge from one other and how they cooperate or compete. This manifold of coexisting or competing phenomena, ranging from Mott transitions [15, 16] to charge density wave (CDW) formation [17] and superconductivity [18], indicates that the electron-phonon and the electron-electron interactions are equally important in the shaping of the physics of these compounds. Such materials also often display photoinduced phase transitions, wherein light pulses can create new transient states by driving ultrafast changes in the macroscopic properties [19, 20, 21, 22].

Recently, a metastable hidden photo-induced state, unaccessible under normal equilibrium conditions, was reported in $1\,T$-TaS_2 [11, 23].

The second material under investigation is $\mathbf{Ba(Fe}_{1-x}\mathbf{Co}_x)_2\mathbf{As}_2$ and belongs to the family of the more recently discovered Fe-based high-T_c superconductors (FeSCs), which have a similarly rich phase diagram as the well-known cuprates. However, the ground state of FeSCs parent compounds is an antiferromagnetic metal, which exhibits spin density wave (SDW) ordering, contrary to the insulating Mott-Hubbard phase in the cuprates, suggestive of a smaller degree of electronic correlations in the FeSCs. Nevertheless, the importance of electron correlation in these systems can be understood by considering the observation that their metallic phases are all characterized as bad metals, for instance, they have a rather large electrical resistivity compared to a conventional metal with the T-dependent term of the resistivity scaling linearly and not quadratically with the temperature [24, 25], suggesting the important role of electron-electron (e-e) interaction. A considerable reduction in the weight of the Drude peak in the optical conductivity is found, which is about 30% of the value expected from non-interacting electrons [26, 27, 28]. These features are common also to cuprates and V_2O_3, for which strong e-e correlations are very established and of primary importance. Mass renormalization observed by ARPES, where the ratio of the observed effective mass of the electron in the paramagnetic phase to the bare band mass (m^*/m_b) is roughly 3-4 [29, 28], and the linear dependence of the quasiparticle scattering rates with respect to the binding energy [30, 31] also indicates the importance of the correlation-induced mass enhancement.

Another important aspect is related to the chemical doping of these systems. As mentioned in the beginning of this introduction chapter, these materials exhibit a phase diagram in which the various ground state can be entered as function of temperature and another control parameter, such as the carrier density, pressure or magnetic field. In order to vary the carrier density, the usual procedure consists in the systematic substitution (doping) of one of the constituent of the material with another element having a different number of valence electrons, leading to an increase (electron doping) or decrease (hole doping) of the number of electrons in the system. Doping allows not only to "span"the phase diagram, but can also have implications on the transition temperatures of the various phases. In high temperature superconductors, for instance, doping can lead to a lower or higher critical temperature T_c. Doping can have dramatic consequences on the properties of a strongly correlated material. For instance, when a Mott-insulator is doped, the system is turned to a weakly correlated metal and becomes conductive. Since doping is such an important mean of modifying the macroscopical physical properties of the systems, doping dependent studies are very important. In this work, a systematic doping dependent

study was conducted in the case of the FeSC electron doped compound, unveiling some effects on the relaxation of the excited electronic population. In $1\,T$-TaS_2, although no doping dependent study was performed, we will show how our results on the Mott-insulating state can be explained and discussed taking into account the effective band filling, that is not only influencing the equilibrium properties but also the dynamics of the system.

Outline

In chapter 2 we will introduce some selected theoretical concepts, functional to the topics treated in the present work, in particular the Mott-Hubbard insulator, the physics of CDW and SDW (mostly in the frame of the Pierls model) and the basics of angle-resolved photoemission spectroscopy in its static and time-resolved versions. In chapter 3 we will then proceed giving a survey of the ground state properties of the materials under investigation, describing the state of the art and addressing some open questions. After a detailed description of the main components of the experimental setup, given in chapter 4, chapter 5 and 6 eventually enter the core of this dissertation, wherein the results of the experiments on $Ba(Fe_{1-x}Co_x)_2As_2$ and $1\,T$-TaS_2, respectively, are reported and discussed extensively. In chapter 5 the ultrafast relaxation of the excited electron population in $Ba(Fe_{1-x}Co_x)_2As_2$ is analyzed at the Brillouin zone center, for compounds with three different dopings, as a function of binding energy. The main results is the observation of a boson-window effect occurring at low excitation density, indicative of the coupling of the excited electronic system to a boson. The fingerprint of such coupling was already observed in the case of cuprates HTSCs **[32]** but contrary to the latter, no counterpart in the equilibrium electronic structure is present for the investigated FePn. In addition, a doping dependence of the relaxation times is found and discussed in comparison to the results obtained by other experimental techniques, transport and static ARPES.
In Chapter 6, we characterize the transient photoinduced state of the Mott-insulator $1\,T$-TaS_2 and then focus on the weak excitation regime, where we observe the transient population of the upper-Hubbard band and monitor its time evolution. From our analysis we could conclude on the decoupling of the electronic and phononic system at early stages after photo-perturbation, which might lead to a significant reduction in complexity for the modeling of Mott-systems. We report on a first theoretical description of our results, developed by our collaborators at the Max Planck research department of Structural Dynamics in Hamburg and at the University of Fribourg, based on a time-resolved dynamical mean-field theory approach. The model shows how the doublon dynamics are influenced by the effective band filling and our results are best reproduced in the case of slightly hole-doped systems. At last we show the switching to a metastable hidden state occurring in this

material and the corresponding changes in its electronic structure.
At the beginning of both these chapters, a short introduction page will provide the motivation, with more specific open questions relative to the investigated problem. In addition, a summary is provided at the end of both chapters. Finally, in chapter 7 the conclusions and outlooks are reported.

In addition to the topics covered in the present dissertation, trARPES experiments on $Bi_2Sr_2CaCu_2O_{8+\delta}$ were performed in collaboration with J.D. Rameau and P.D. Johnson from the Brookhaven National Laboratory (New York, USA), that will not be covered here. ARPES experiments at Bessy II (Berlin, Germany) were performed on other Fe122 pnictides systems, in collaboration with J. Fink from the Leibniz-Institute for Solid State and Materials Research Dresden (Dresden, Germany) and Emile Rienks from the Helmholtz-Zentrum Berlin. In the first section of chapter 5, some selected results obtained from this experimental effort are briefly shown in the context of the main results object of this thesis work.
Scientific works to which the present author contributed are marked with bold fonts, whenever cited. At the beginning of chapter 5 and 6, in the introduction page, the scientific papers (published or submitted) where part of the reported results can be found, are explicitly mentioned.

Chapter 2

Brief Theoretical Survey

2.1 Consequences of electronic correlations

In conventional materials the Pauli exclusion principle and the delocalized character of their electronic states, built primarily from s and p orbitals, results in the predominance of the kinetic energy of the electrons, which determines their ability of quantum-mechanically tunnel around in the crystal. As a consequence, they can be treated as effectively non-interacting particles, which is the base assumption for conventional band theories in solid state physics. In strongly correlated materials, instead, the repulsive Coulomb interaction among electrons becomes so sizable that it cannot be neglected anymore and one can no longer consider any electron as being in a "sea" of the averaged motion of the others but each single electron has a complex influence on its neighbors. This class of materials includes rare-earth and transition metals in which, on the atomic level, the most convenient energetic configuration has open d and f shells, where electrons occupy narrow orbitals. The complex interplay between electronic, structural and magnetic degrees of freedom results in the emergence of various physical phenomena, such as high-temperature superconductivity, metal-insulator phase transitions, changes in magnetic order which are of deep scientific and technological interest and, thus, object of intense theoretical and experimental research. However, the strong electron correlations make them difficult to study, because of the non applicability of perturbative methods, such as the local density and Hartree Fock approximation, Thomas-Fermi screening, etc. Although band theories like Landau-Fermi liquid (FL) [33] or density functional theory (DFT) [34] methods, where the interactions of the individual particles are replaced by an effective mean interaction, are a good starting point to understand weakly correlated electrons systems, they fail in the case of systems with strong correlations. For such systems, model Hamiltonian approaches (as the Hubbard model) are used, which reduce the full many-body hamiltonian to a simpler effective model retaining the

essence of the physical phenomena one wants to understand and neglecting other aspects. However it is itself a complicated problem. To get more insight, we will proceed by describing the model system which comes into mind when thinking about correlated-electron systems and inspiration behind what later became the Hubbard model, that is the Mott insulator. A brief survey on the properties of such a system is also propedeutical to the discussion about the results reported for the $1T$-TaS_2 compound.

2.1.1 Mott-Hubbard insulator

In the presence of electronic correlations, band theories fail in capturing the emergent properties arising from the complex many-body interaction. One example are the so-called Mott insulators [35, 36]. Materials belonging to this class are incorrectly predicted to be metallic as their electronic configuration would lead to a partially filled band, but they actually behave like insulators. The failure of band theory was first noticed in insulators such as NiO [36, 37] and extends to a variety of transition metals and their oxides, characterized by open d or f shells where electrons occupy narrow orbitals. The reason is that the electrons experience strong Coulombic repulsion because of their spatial confinement in those orbitals. One of the simplest model, and still the most successful one, used to describe materials with electronic correlations is the Hubbard model [38], which describes a system of interacting electrons by a Hamiltonian consisting of two terms:

$$H = \sum_{ij,\sigma} t_{ij} c^{\dagger}_{i,\sigma} c_{j,\sigma} + U \sum_{i} n_{i\uparrow} n_{i\downarrow} \tag{2.1}$$

This Hamiltonian describes electrons with spin $\sigma =\uparrow$ or $\downarrow$ moving between localized states at lattice sites i and j. The kinetic energy and the interaction energy are characterized by a hopping term t_{ij} and the local Coulomb repulsion U, respectively. These two terms compete because the kinetic part favors the electrons' mobility, while the interaction U is minimal when electrons stay apart from one other (localized on atomic different sites). The parameters that determine the properties described by the Hubbard model are the Coulomb interaction U, the bandwidth W (which is determined from the hopping term t_{ij}), the temperature T and the density of electrons. In particular, depending on the ratio U/W a metal-to-insulator transition (MIT) might occur. Figure 2.1 shows the evolution of the electronic density of states (DOS) according to the ratio U/W.

For the case in which electrons are completely independent, the DOS reflects the situation of a metal with the Fermi level E_{F} located in the middle of the band (Fig. 2.1(a)). With increasing correlations, the bandwidth becomes narrower and the spectrum shows a characteristic three-peak structure: the Hubbard bands, which originate from local atomic excitations and are broadened by the hopping of electrons and the quasiparticle peak near

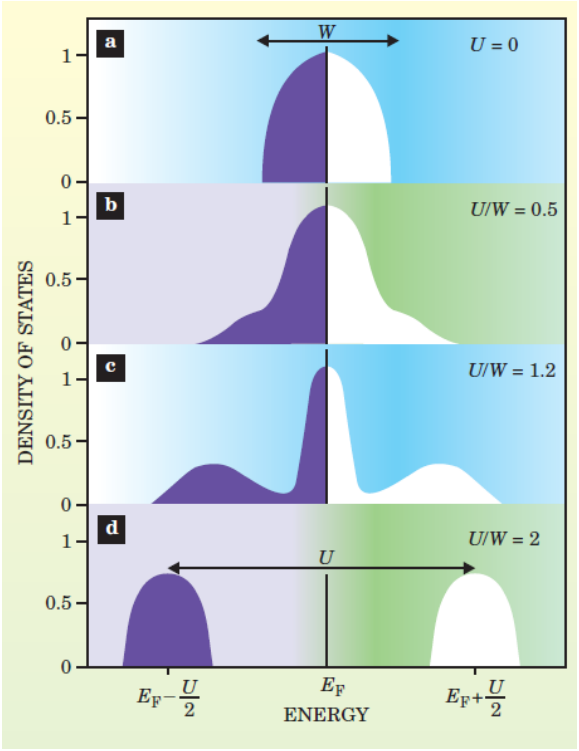

Figure 2.1: Evolution of the density of electronic states with the ratio U/W, as given by the dynamical mean-field solution of the Hubbard model at $T = 0$ and half filling. From [39]

the Fermi level (Fig. 2.1(b) and (c)). The MIT occurs when the electron interactions are sufficiently strong to cause the quasiparticle peak to vanish and the spectral weight is entirely transferred into the upper and lower Hubbard bands (UHB and LHB, respectively), separated by an energy gap $\Delta \approx U$ (Fig. 2.1(d)). In the Mott insulating state, the charge degrees of freedom are frozen, and the accompanying spin degrees of freedom are referred to as local moments. These local moments are coupled with each other through exchange interactions and often take on an antiferromagnetic order. Figure 2.2 schematically shows, in a very simplified manner, such a real space picture in the case of half filling ($\langle n_{i\uparrow} \rangle = \langle n_{i\downarrow} \rangle = 1/2$), where each single electron occupies a single lattice site. Such electrons have a certain probability to hop to a neighboring lattice site, with a certain hopping rate J, as depicted in the second raw of figure 2.2 and here the electrons feel the on-site Coulomb repulsion U. Empty and doubly occupied sites in a Mott-Hubbard insulator give rise to states referred to as holons and doublons, respectively. One common picture to describe the MIT involves the binding of doublons and holons, which would occur under a certain critical value

of U and leads to the opening of the gap, while in the conductive regime, holons and doublons can move independently [40, 41].

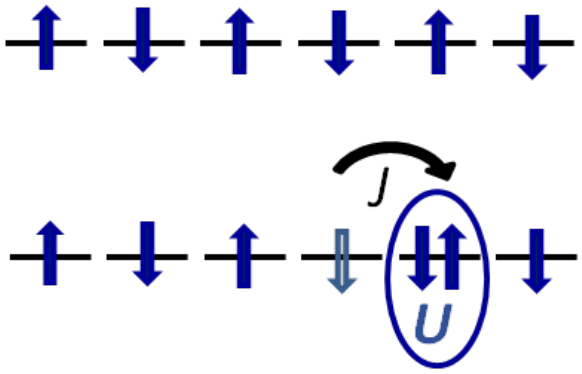

Figure 2.2: Schematics of a real space picture of a Mott-insulator at half filling. The blue arrows indicate the spins of the electrons which occupy single lattice sites. The second raw schematically reproduce the J-mediated hopping of one electron from its original position to the neighboring lattice site, where they will feel a strong on-site Coulomb repulsion U. The vacant site represents holon states and the doubly occupied site represents doublon states.

The simplest excitation we can consider of a Mott insulator, as the one depicted in figure 2.2, is the one where a quantum of energy equal (or slightly exceeding) the Mott gap is deposited into the system, leading to the hopping of electrons and the population of doubly occupied states. However, the above illustrated concepts are an extreme simplification, meant to provide a first intuitive approach to describe the system. In reality, understanding the non-equilibrium dynamics of a quantum many-body system is a major challenge in physics [42]. First of all, the pumping process drives the formation of so called Hubbard-excitons, i.e. bound states between doublons and its neighboring empty sites holons, which rapidly dephase as a consequence of electron-electron and electron-boson scattering processes. Since the timescale of this process is of the order of a hopping cycle (few femtoseconds), extremely high temporal resolution is required in the experiment. Second, the excitation has an effect on the whole system, including phonons, magnons, etc. and approaches by which electronic DOS and Fermi-Dirac distribution can be disentangled frequently fails.
Since Mott insulators can become conductive by changing some external parameters like pressure, doping or magnetic field, they are of deep scientific and technological interest. Examples of this kind of materials are the parent compounds of the well known cuprates High-T_c superconductors and some organic compounds. An example of a Mott insulator treated in this work is $1T$-TaS_2, in which Mott physics coexist with broken symmetry phases like CDWs. In the case of Fe-based High-T_c superconductors, orbital-selective

Mott physics has been proposed, in which the interplay among the kinetic energy, U and the Hund's coupling parameter can lead to different behavior for the various orbitals [28].

2.1.2 Charge and spin density waves

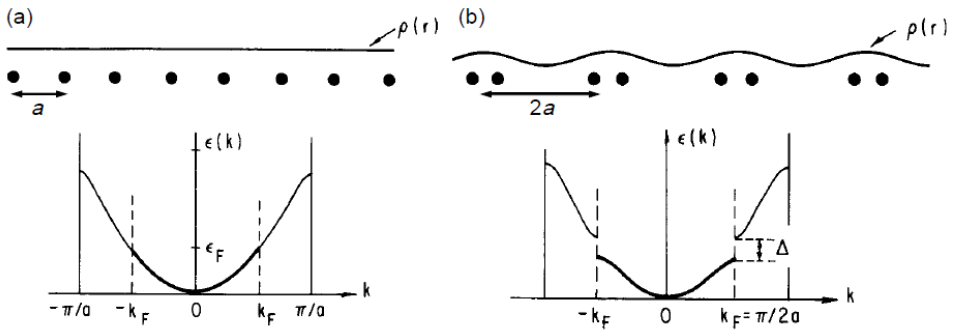

Figure 2.3: Peierls transition in a linear atomic chain. (a) A linear chain of atoms with lattice constant a and constant charge density $\rho(r)$ results in a nearly-free electron parabolic band $\epsilon(k)$, which is half-filled up to the Fermi wave vector $k_{\mathrm{F}} = \pi/a$. (b) The periodic distortion of the charge density $\rho(r)$ by the CDW with period $2a$ introduces a new Brillouin zone boundary at $k_{\mathrm{F}} = \pi/2a$, which leads to the opening of an energy gap Δ at the Fermi energy E_{F}. After [43]

One of the most surprising results in condensed matter physics is that a Fermi liquid (i.e. an ordinary metal) ground state is quite unstable in systems with reduced dimensionality. If electrons at the Fermi level can lower their energy via a gap opening at the Fermi level, they will do this, under certain conditions like low temperature. Charge density waves (CDWs) and spin density waves (SDWs) are some common example. Transition metal chalcogenides like $NbSe_3$, $TaSe_3$ and TaS_2, transition metal bronzes, and quasione-dimensional (1D) inorganic and organic conductors like Krogmann's salt KCP are some of the materials forming CDWs, while SDWs have been studied in e.g. Chromium and Bechgaard's salt TTF [43]. The parent compounds of many Fe-based superconductors (included the one investigated here) also display SDW transition. As the name implies, in the broken symmetry ground state, the charge or the spin density is not uniform but displays a periodic spatial variation and leads to gap openings at the Fermi level. For this reason when the transition to CDW was introduced by R. Peierls and Fröhlich [44, 45], it was referred to as metal-to insulator transition. Key ingredients for the formation of charge density waves and spin density waves ground states are strong and anisotropic $e - ph$ or $e - e$ coupling and a high density of states at the Fermi level $n(E_{\mathrm{F}})$. The basic description of CDW formation is usually given within the Peierls model which

considers at first an infinite linear chain of atoms and discuss the instability of such system to an external stimulus. Here we will briefly concentrate on the description of the charge density wave ground state and its implications for the band structure; however, similar concepts hold for the SDW formation [43].

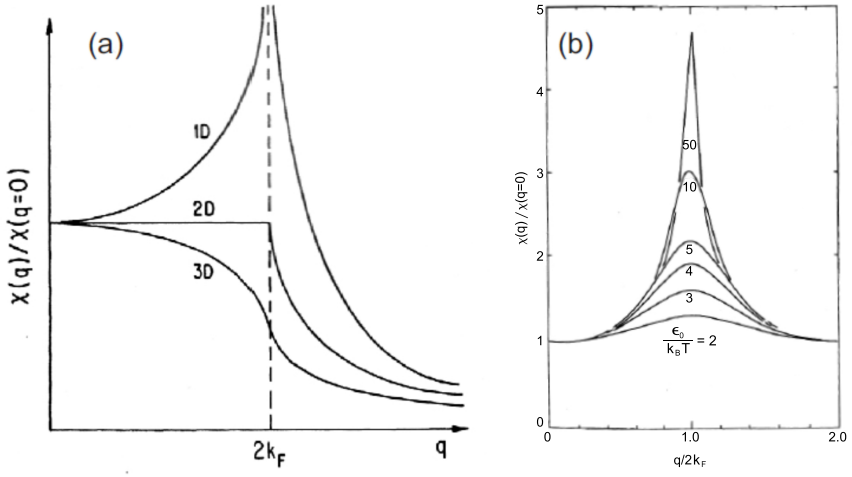

Figure 2.4: Dependence on dimensionality and temperature of the Lindhard response function. (a) $\chi(\vec{q})$ at $T = 0$ for one, two and three dimensions. In the 1D case, the response function diverges at $q = 2k_F$. (b) Temperature dependence of the 1D Lindhard response function. For $T > 0$, the divergence is replaced by a finite value. From [43]

If we consider a 1D linear chain of atoms with the lattice constant a and a constant charge density $\rho(r)$, the band model of a nearly-free electron gas leads to parabolic bands, as sketched in figure 2.3(a). Assuming one valence electron per atom of the chain, these bands are half-filled up to the Fermi wave vector $k_{\mathrm{F}} = \pi/2a$. The particular topology of the Fermi surface (FS), consisting of two points at $-k_{\mathrm{F}}$ and $+k_{\mathrm{F}}$, leads to a response to an external perturbation which is dramatically different from that obtained in higher dimensions. The response of an electron gas to a time independent potential of the form

$$\phi(\vec{r}) = \int_q \phi(\vec{q}) e^{iq'r'} d\vec{q} \tag{2.2}$$

is usually treated in the framework of linear response theory. The rearrangement of the charge density, expressed in terms of induced charge

$$\rho^{ind}(\vec{r}) = \int_q \rho^{ind}(\vec{q}) e^{iq'r'} d\vec{q} \tag{2.3}$$

is related to $\phi(\vec{r})$ through

$$\rho^{ind}(\vec{r}) = \chi(\vec{q})\phi(\vec{q}) \tag{2.4}$$

where $\chi(\vec{q})$, the so-called Lindhard response function, is the general susceptibility of the electron gas and in d dimensions is given by

$$\chi(\vec{q}) = \int \frac{d\vec{k}}{(2\pi)^d} \frac{f_k - f_{k+q}}{\epsilon_k - \epsilon_{k+q}} \tag{2.5}$$

where $f_k = f(\epsilon_k)$ is the population of states at momentum k. In 1D the susceptibility takes the form:

$$\chi(\vec{q}) = -e^2 n(\epsilon_F) \ln\left|\frac{q + 2k_\mathrm{F}}{q - 2k_\mathrm{F}}\right| \tag{2.6}$$

where $n(\epsilon_F)$ is the DOS for one spin direction. Contrary to the higher-D case, solving the integral in 1D leads to a response function that diverges at $q = 2k_\mathrm{F}$ (see figure 2.4 a). An important consequence is that the electron system is unstable with respect to the formation of a periodically charge (or spin) modulated structure.
Going back to figure 2.3, the introduction of a periodic distortion of the atomic position with period $2a$ leads to an additional modulation of the charge density $\rho(r)$. This new periodicity of $2a$ corresponds to a new BZ boundary and the opening of an energy gap Δ in the nearly-free electron bands at $k = \pi/2a$, the former value of k_F in the half-filled band, as sketched in figure 2.3(b). The result is an energy gain of the electronic states near E_F, which is the driving force for the CDW formation. The size of Δ is proportional to the amplitude of the distortion u, and it is simple to show that the decrease in the total electronic energy is proportional to $u^2 \ln u$. The cost in elastic energy is proportional to u^2, which is smaller than $u^2 \ln u$ for small u, hence some distortion will always occur [46]. Due to the opening of the energy gap Δ at the Fermi energy, the FS is destroyed and the CDW ground state becomes insulating.

As previously mentioned, a pronounced dependence of the response function on the dimensionality of the system comes from the topology of the Fermi surface. The denominator in eq. 2.5 is suggestive of a divergence of $\chi(q)$ for $\epsilon(k) = \epsilon(k + q)$. This condition is the so-called FS nesting and it is fulfilled if there are large segments of a Fermi surface that can be connected by a single $\vec{q}$-vector. This condition strongly depends on the dimensionality of the system, as shown in figure 2.5. In a 1D freely-electron gas, since the Fermi surface consists of two lines at $\pm k_F$, the nesting is perfect, while in 2D there is no nesting[1], as the FS is a circle. For a three-dimensional (3D) system, χ is a smooth function of q and exhibits a discontinuity of the first derivative at $q = 2k_\mathrm{F}$ in two dimensions. In contrast, for a 1D system, χ

[1] nesting can only occur for two points on the FS by a single vector $\vec{q}$,

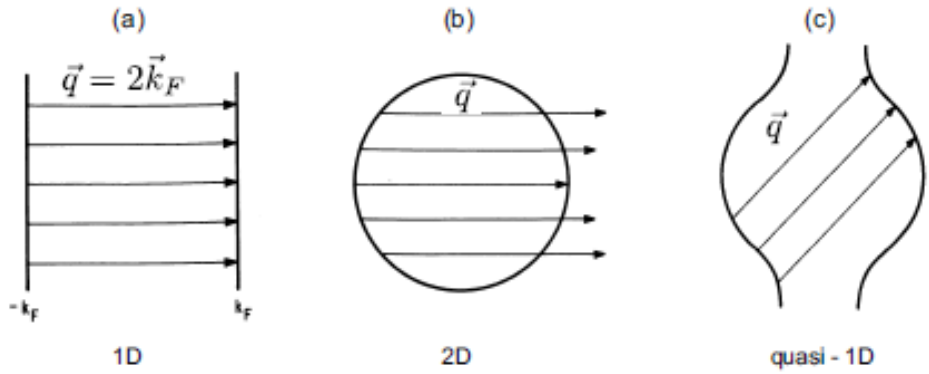

Figure 2.5: Fermi surface topology in various dimensions. (a) In the 1D case, the FS is perfectly nested by a single nesting vector $\vec{q}$. (b) For a 2D system, the nesting is reduced to two points on the FS. (c) A quasi-1D system can exhibit perfect nesting for a larger part of the FS despite some 2D dispersion. From [43]

shows a divergence at $q = 2k_{\mathrm{F}}$, which describes a critical susceptibility to a disturbance with $\vec{q} = 2\vec{k}_{\mathrm{F}}$ and can induce an instability of the electron density in such systems, leading to the formation of the density wave ground state. However, a 1D system is just a model and it is never present in reality, while CDW or SDW transition occur indeed in real systems. Here, the case of a quasi-one dimensional FS is of importance, as shown in figure 2.5(c), which occurs for layered materials, as the one studied in this work. In such systems , with only weakly 2D dispersions, perfect nesting can still be obtained for large parts of the FS. For higher temperatures $T > 0$, the divergence in χ is replaced by a large finite value, dependent on T and takes the form

$$\chi(2k_F, T) = e_0^2 n(\epsilon_F) \ln \frac{1.14\epsilon_0}{k_B T} \tag{2.7}$$

where ϵ_0 is an arbitrary cutoff which is usually chosen as $\epsilon_0 = \epsilon_F$ [43]. This behavior indicates that the CDW state only occurs below a transition temperature T_{CDW}. The response function can be evaluated for q values different from $2k_F$ and $\chi(\vec{q}, T)$, obtained for different values of $\epsilon_0/k_B T$ is displayed in figure 2.4 (b).
$BaFe_2As_2$, common to other FeSCs, shows SDW transition, caused by nesting of the FS (see chapter 3). However, not all density waves are driven by nesting, and not all Fermi surface topologies with a good nesting condition result in a CDW instability. For instance in $1T$-$TiSe_2$ the cause of CDW is supported by exciton condensation, rather than FS nesting [47, 48]. Also in the case of $1T$-TaS_2 (see chapter 3), the Peierls mechanism is insufficient to explain the CDW phase, which in addition, coexist with a Mott phase. Indeed it has been proposed that electronic correlations play a much more

central part in the CDW ordering itself [48, 8].

2.2 Photoelectron Spectroscopy

The experimental method employed to investigate the materials which are the objects of this work is ultrafast time- and angle-resolved photoelectron spectroscopy (trARPES). In this chapter an overview of the basic concepts concerning this technique, based on the photoelectric effect [49], will be provided. Photoelectron (or photoemission) spectroscopy measures the kinetic energy and momentum of a photoelectron emitted from a solid, gas or adsorbate system and has been established as a standard tool in solid state research[2], which provides direct access to the electronic structure of the investigated system. In a photoemission experiment, electrons are emitted by photons of a certain energy $\hbar\omega$ exceeding the work function Φ, or ionization potential, of the sample material. The so called photoelectrons are then analyzed in an electrostatic analyzer with respect to their kinetic energy E_k, given by:

$$E_k = \hbar\omega - \Phi - |E_b| \tag{2.8}$$

where E_b is the binding energy of the electrons with respect to the Fermi level. In addition, the emission angle of photoelectrons allows to determine the in-plane momentum component $\vec{k_\parallel}$, which is conserved in the photoemission process, while the momentum component perpendicular to the surface $k_\perp$ is altered by the inner potential and generally not conserved. Thus, by systematically changing the photoemission angle it is possible to map out the electronic band structure of the system with respect to the in-plane momentum, as it will be explained in section 2.2.1 concerning angle-resolved photoemission (ARPES).
The photoemission intensity $I(E_k)$ obtained from the analyzed photoelectrons in an ARPES experiment is given by [50]:

$$I(E, \vec{k_\parallel}) = M(E, \vec{k_\parallel}) f(E, T) A(E, \vec{k}) \tag{2.9}$$

where M is a (generally angle- and photon-energy-dependent) photoemission matrix element, $f(E, T)$ is the Fermi-Dirac distribution function and $A(E, \vec{k})$ is the single-particle spectral function. The latter is the imaginary part of the Green's function $G(\vec{k}, E)$, a fundamental property of an N-electron system, used to describe the transition probability of an electron from an initial to a final state due to a scattering process with energy transfer E:

[2]The Nobel prize 1981 was awarded to Kai M. Siegbahn "for his contribution to the development of high-resolution electron spectroscopy".

$$A(E,\vec{k}) = \frac{1}{\pi}|\mathrm{Im}G(\vec{k},E)| \tag{2.10}$$

The interaction among electrons is taken into account by considering them as quasiparticle, i.e. electrons which are "dressed" by virtual excitations that move with them coherently. This is achieved by adding the so-called self-energy $\Sigma(\vec{k},E) = \mathrm{Re}\Sigma + i\mathrm{Im}\Sigma$ to the single-particle electron energy $E^0(\vec{k})$, yielding to:

$$A(E,\vec{k}) = \frac{1}{\pi}\frac{\mathrm{Im}\Sigma}{(E - E^0(\vec{k}) - \mathrm{Re}\Sigma)^2 + (\mathrm{Im}\Sigma)^2} \tag{2.11}$$

where $\mathrm{Re}\Sigma$ renormalizes the binding energy in the screened potential and $\mathrm{Im}\Sigma$ represents the line width and is proportional to the inverse lifetime of the quasiparticle. Thus, via the spectral function, ARPES is sensitive to many-body effects like electron correlation or electron-boson interaction.

It has to be considered that photoemission is an electron removal spectroscopic technique. Thus, it does not directly measure the electron energies of the unperturbed N particle system but the energy of the $N-1$ particle system, where one electron has been removed. In this context, an important approximation is used, the so-called sudden approximation, which assumes that the photoemission process occurs much faster than it takes for the electronic system to relax the excited electronic state. In reality, the relaxation of the $N-1$ excited states can result in final state effects, such as incoherent background or satellite peaks appearing in the photoemission spectrum. However, the influence of these effects on the binding energies are rather small and the sudden approximation is widely used. Its validity has been questioned at small kinetic energies , as the one obtained from pulse energies below 7 eV. However, recent investigations comparing spectra using different photon energies seem to confirm its validity even for very low kinetic energies such as the ones used in this thesis [51].

2.2.1 Static angle-resolved photoemission spectroscopy

A typical scheme of an ARPES experiment is shown in fig. 2.6. Electrons emitted with a certain angle θ with respect to the surface's normal are detected and their kinetic energy is calculated. In the case of our setup E_k is obtained from the time of flight (TOF). The momentum of the electrons is given by $\vec{k} = \sqrt{2mE_k}/\hbar$ and the respective components can be calculated by means of the angle θ and ϕ. In an ARPES experiment, the momentum of the photon is significantly smaller than the Brillouin zone $2\pi/a$ and can be neglected. Thus, the optical transitions are considered to be vertical ($\Delta\vec{k} = 0$) and the momentum component parallel to the surface $k_{\|}$ is conserved, as depicted in fig. 2.6, and is given by:

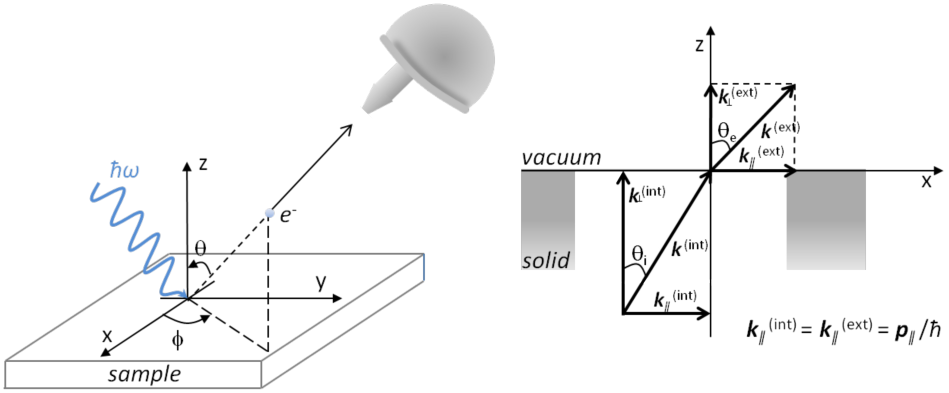

Figure 2.6: The picture on the left shows a schematics of an ARPES experiment in which a photon of energy $\hbar\omega$ photoemits an electron with a certain direction with respect to the sample surface defined by the angles θ and ϕ. The photoelectron is subsequently detected and its kinetic energy is determined. On the right, the conservation of the parallel momentum $k_{\parallel}$ is shown.

$$k_{\parallel}(\theta, E_k) = \frac{\sqrt{2mE_k}}{\hbar}\sin\theta_e = 0.5123[\text{Å}\,\text{eV}^{-1/2}]\sin\theta_e\sqrt{E_k[\text{eV}]} \tag{2.12}$$

where m is the free electron mass. Measuring the photoemission intensity as function of kinetic energy and photoemission angle allows to map out the complete electronic band structure parallel to the surface, which results in detailed information on the electronic dispersions. The momentum component perpendicular to the surface $k_{\perp}$ is in general not conserved, due to breaking of symmetry in the presence of the surface, which modifies the potential in the z direction. However, the final state momentum is known and assuming a transmission into parabolic free-electron states above the vacuum level, the perpendicular momentum is accessible:

$$\begin{aligned} E_k &= \frac{\hbar^2}{2m}(k_{\parallel} + k_{\perp})^2 - V_0, \\ k_{\perp} &= \sqrt{\frac{2m(e_k + V_0)}{\hbar^2}} - k_{\parallel} \end{aligned} \tag{2.13}$$

Here, V_0 is an inner potential, which determines the offset of the free-electron final state dispersion with respect to the vacuum level. In practice, V_0 is determined either from band structure calculations or experimentally from the periodicity of electron dispersions as a function of incident photon energy. Combining eq. (2.12) and (2.13) enables to effectively map out the entire 3D band structure by measuring the ARPES intensity as a function of kinetic energy, emission angle and photon energy.

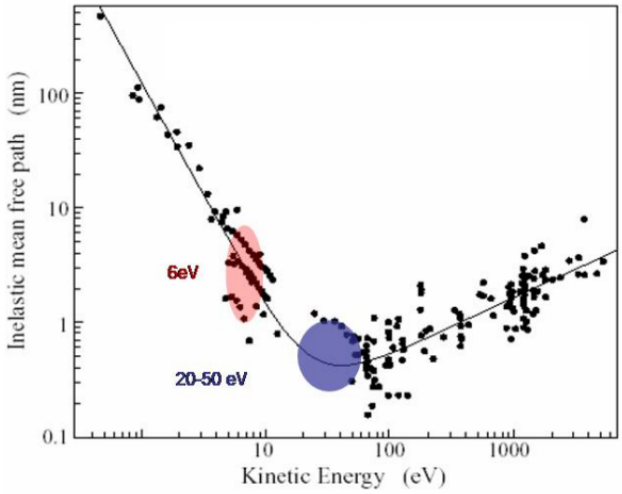

Figure 2.7: Universal curve of the mean free path of electrons [52]. It displays a minimum at around 30 eV (marked in blue). The red mark indicates the mean free path for the kinetic energy of 6 eV, used in our experiment

ARPES is a well established surface sensitive technique, resulting from the limited escape depth of the electrons in solids [52]. The mean free path of an electron as a function on kinetic energy is depicted in Fig. 2.7 and it is, in first approximation, independent of the material. It displays a minimum between $\sim 20 - 50\,\mathrm{eV}$, where the electron's mean free path is only a few Å and ARPES is most surface sensitive. At the probe photon energy of 6 eV, used in our experiments, the electron's mean free path amounts to $\sim 30\,\text{Å}$. In general, for laser photoemission experiments employing the low photon energy of $6 - 7\,\mathrm{eV}$ [53, 51, 54], a bulk sensitivity can be considered due to a larger mean free path of excited electrons. The enhanced bulk sensitivity could be exploited, for instance, for detection of states at buried interfaces [55] and for evidencing superconductive gap anisotropy in f-electron superconductors [53]. On the other hand, a sensitivity to electronic surface states for these small kinetic energies of photoelectrons is well established [56, 57]. Therefore, the degree of surface versus bulk sensitivity might be highly material specific and the photoemission matrix elements need to be considered in detail [58]. In the case of the 122 Fe-based materials investigated in this work, a considerable k_z dispersion, which further increases with doping, was established [59, 60] and its implication on our experimental observations will be discussed in details (see chapter5). For $1T$-TaS_2, the other material under investigation here, the surface layer exhibits very similar properties to the bulk [61], nevertheless combined surface

and bulk sensitivity was reported [19].

Considering the final width of the Fermi-Dirac distribution function (of the order of $\sim$ meV), ARPES mainly probes occupied states. Knowledge of the spectral function above E_F is of considerable interest as states in the unoccupied part of the electronic structure determine important material properties, such as e.g. the optical absorption. Although some information above the Fermi level can be gained by dividing through a Fermi-Dirac distribution function, broadened by the instrument resolution, or by symmetrization around E_F, these methods are fairly limited and restricted to small energy windows. For the spectroscopy of the unoccupied states, two-photon photoemission (2PPE) has been established, which employs two photons with an energy below the work function of the system. The first photon promotes electrons from initial occupied states into unoccupied intermediate states above E_F and the second one photoemits them.
Finally, the introduction of a pump-probe scheme leads to the time-resolved (tr) 2PPE and trARPES techniques, that will be treated in section 2.2.2.

2.2.2 Pump-probe photoemission spectroscopy

The use of ultrashort laser pulses allows for a natural implementation of a pump-probe scheme in photoemission experiments. In 2PPE, this is achieved by varying the delay between the two pulses with femtosecond resolution, enabling unique access to the non equilibrium dynamics of the unoccupied electronic structure. 2PPE and tr2PPE have been established as powerful tools to study unoccupied electronic states, surface- and image potential states and their dynamics [62, 63, 64, 65, 66] as well as excitonic states [67, 68].
In contrast, time- and angle-resolved direct photoemission (trARPES), using a probe photon energy that is larger than the work function, allows for the spectroscopy of both occupied and unoccupied electronic states. In trARPES, an ultrashort laser pulse (pump pulse) excites the sample and a subsequent ultrashort probe pulse photoemits electrons after a variable time-delay, yielding access to the time-dependent spectral function $A(E, k, t)$ with a time resolution given by the convolution of the pump and probe pulse widths. Hence, compared to purely optical pump-probe schemes, trARPES has the advantage to detect the non-equilibrium dynamics of the occupied electronic structure directly in the reciprocal space, with no need of any model assumptions. The fairly strong pump pulse excites the sample and perturbs the system stronger than in tr2PPE, generating a significant amount of excited carriers. Typical excitation fluences ranges from $\sim 50\,\mu\mathrm{J/cm^2}$ to $\sim 2\,\mathrm{mJ/cm^2}$ and the pulse duration is of the order of few tens of fs. A much weaker UV probe pulse, with a photon energy $h\nu$ higher than the work function Φ of the sample, subsequently photoemits electrons out of the excited system, thus taking a "snapshot" of the electronic states

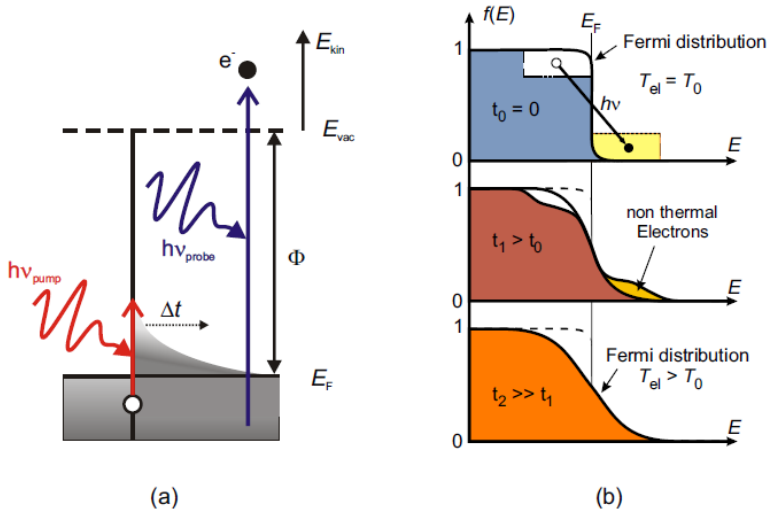

Figure 2.8: (a) sketch of trARPES experiment. An intense IR pulse excites the system and generates an electron population above E_{F}. A UV pulse photoemits electrons from the excited sample at different time delays. (b) Sketch of the time-dependent electron distribution and of the thermalization process typical for metals. Taken from [69]

at time t after the initial excitation, as depicted in fig 2.8 (a). By varying the time delay between the pump and the probe pulse, the transient changes of the electronic structure are mapped as a function of kinetic energy, momentum and time-delay. The overall time resolution ranges about $90 - 110$ fs in the case of our experiments.

In fig. 2.8 b, the excitation and subsequent equilibration of the transient electron population around E_{F} is schematically discussed, in the simple case of metals, considering a constant DOS at the Fermi level and rigid bands. At equilibrium, the system is characterized by a Fermi-Dirac distribution with an electronic temperature equal to the macroscopic base temperature $T_{\mathrm{el}} = T_{\mathrm{eq}}$. With the excitation of the pump pulse, part of the electrons in the occupied part are suddenly excited to states above E_{F}, resulting in a strongly non-thermal distribution, that manifests in a deviation from the approximately exponential decrease of the Fermi-Dirac distribution for energies $E \gtrsim k_B T$. Within several tens to some hundreds of femtoseconds, the excited electrons population redistributes mainly via $e - e$ scattering, re-establishing a (hot) Fermi-Dirac distribution with a transient electronic temperature $T_{\mathrm{el}} > T_{\mathrm{eq}}$ [70, 71], which can reach up to several thousands of K. This whole process, which leads to the creation of a large number of secondary electron-hole $(e - h)$ pairs, is termed thermalization of electrons. Finally, the process through which the photoexcited populations release the excess energy and relax at surfaces are mainly electron-phonon $(e-ph)$, or in general electron-boson $(e - b)$ scattering, and diffusion [72, 62]. While $e - e$

scattering is responsible for electron thermalization, it does not contribute to the energy dissipation, which is achieved by transferring the energy from the electronic to the phononic system through $e - ph$ scattering.
TrARPES is a powerful tool for studying the time evolution of the electronic structure [47, 8, 73, 74] and has recently come to the forefront as a method for studying the quasiparticle lifetimes of complex materials through analyzing their population dynamics [75, 1, 76, 77] and thus the related interactions. While the lifetime analysis of the laser-excited population relaxation has proven successful for high quasiparticle energies down to $\sim 0.5\,\mathrm{eV}$, at energies close to the Fermi level, the situation is more challenging. At higher energies, relaxation is dominant at all times and quasiparticle lifetimes can indeed be determined in the time domain, but close to E_F the redistribution of secondary excitations deriving from $e - e$ scattering of the primarily excited carriers, during the thermalization process, becomes important. Subsequently, coupling to phonons becomes in general the dominant contribution. Such effects hinder the lifetime determination as all the contributions to the relaxation of the totally excited population do not add additively, as it is instead the case for single-particle lifetimes, determined by e.g. ARPES through line width analysis [78]. On the other hand, through an energy dependent analysis of the population relaxation, as the one provided in this dissertation, coupling of the electronic system to specific bosonic mode can be unveiled, which are instead obscured in equilibrium. An example will be provided in the study of $Ba(Fe_{1-x}Co_x)_2As_2$ (see chapter 5).

In trARPES the excitation of a large number of charge carriers and the resulting high electronic temperatures can have drastic influence on the occupied and unoccupied electronic structure. Sudden changes of the electronic DOS at E_F can change the electronic screening and modify the Coulomb interaction. This can lead to effects like photodoping and the excitation of coherent phonons [79, 80, 19][**81**], directly visible in the transient spectra. Moreover, through the analysis of the time-dependent spectral function $A(E, k, t)$, trARPES allows the observation of transient phase transitions far from thermal equilibrium [19, 20, 21, 8, 54] and the identification of the underlying timescales and interactions. In addition, by employing weaker excitation densities that do not perturb the electronic system significantly, trARPES allows access to the unoccupied electronic structure close to E_F. One such example is also reported in this thesis, which is the transient population of the UHB in $1T-TaS_2$ (see chapter 6).

Chapter 3

Materials description and properties

3.1 Iron-based superconductors

In 2008, the discovery of superconductivity in LaFeAs($O_{1-x}F_x$) [82] ignited an explosion of research activities that uncovered a new class of HTSCs based on iron. This family turned out to have an expansive selection of material variations, including Fe pnictides (pnictogens are elements in group 15 of the periodic table, like arsenic) and Fe chalcogenides (chalcogens are elements from group 16, like selenium), which are usually labeled according to the stoichiometry of their prototype compound [83, 84].

The crystal structure of these families is shown in figure 3.1. They all have a layered structure where the main components are slabs made of Fe ions forming a square lattice, with pnictogen or chalcogen atoms located above and below the planes. This reflects, in momentum space, in a complex electronic structure, having all the Fe 3d orbitals contributing to the states near the Fermi level, which can be different for different families and compounds. The Fermi surface (FS) of most iron pnictides consists of hole pockets (i.e. bands that are almost completely filled and show a dispersion with negative effective electron masses) at the Brillouin zone center and electron pockets (i.e. bands that are almost completely empty and show a dispersion with positive effective electron masses) at the zone boundaries, while for Fe chalcogenides, the hole pockets are absent [28]. Another common feature to all Fe-based superconductors is the presence of antiferromagnetic (AFM) order in proximity to the superconductive dome in the phase diagram [85, 84] and the emergence of superconductivity from the suppression of the AFM order, achieved by tuning a control parameter, like doping or pressure.

As one can see from the exemplary phase diagrams in figure 3.2, iron pnictides exhibit several competing phases and it is possible to tune from one

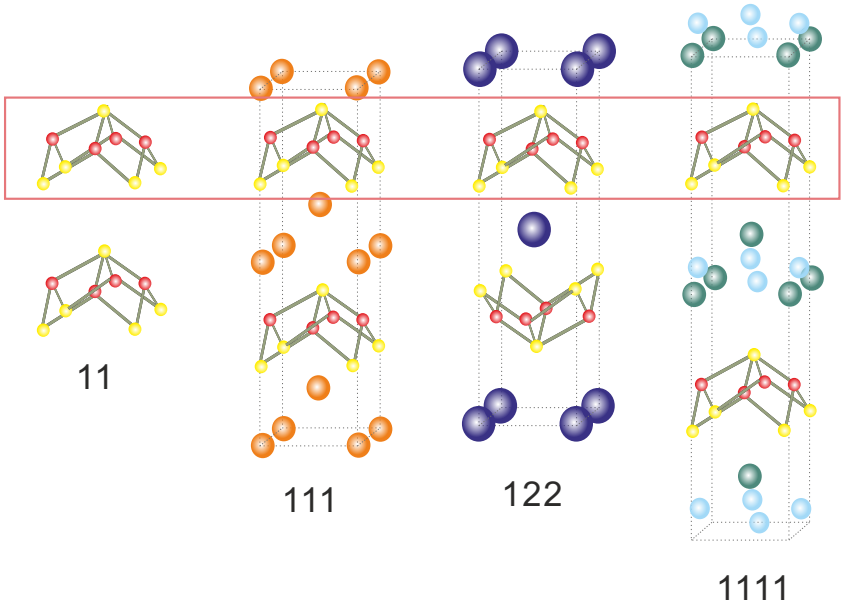

Figure 3.1: Crystal structure of several iron-based superconductors. All these subfamilies share the common trilayer block (highlighted by the red box) formed by Fe (red dots) and the pnictogens or chalcogens located above and below the Fe-plane. From right to left: Examples of Fe pnictides are the so called 1111 systems RFeAsO (R represents a rare earth element), the 122 systems XFe_2As_2 (X represents an alkaline earth metal), and the 111 systems such as LiFeAs. The 11 systems are an example of Fe chalcogenides like FeSe or FeTe. Other examples of Fe chalcogenides are the 122 systems $A_xFe_{2-y}Se_2$ (A can be alkali atoms) [84].

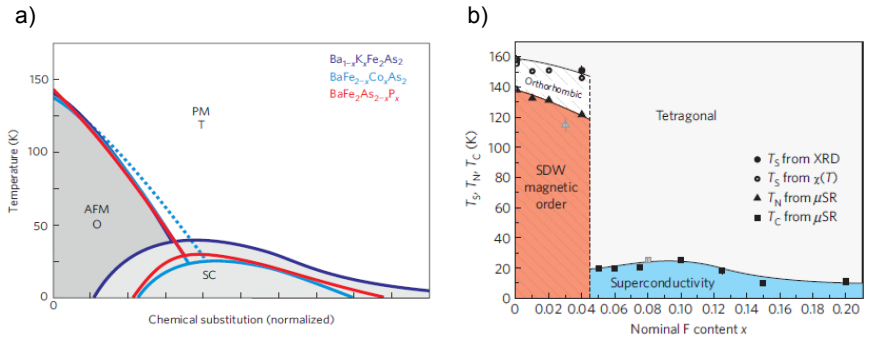

Figure 3.2: (a) Phase diagram of 122 compounds as a function of electron-, hole- and isovalent doping. In the case of electron- and isovalent underdoped compound, a coexistence of AFM and superconductive state is visible (from [83]). (b) Phase diagram of electron doped $LaO_{1-x}F_xFeAs$ as a function of the Fluorine concentration. The transition from AFM to superconductive phase is a sharp first order transition (from [86]).

to another by adjusting some control parameter (like doping or pressure). The fact that superconductivity appears at the end of the antiferromagnetic range might suggest that the pairing could be mediated by antiferromagnetic quantum fluctuations. One view is that the point in the phase diagram where the transition takes place is potentially a quantum critical point (QCP) and the dynamical fluctuations of the order parameter occurring there are important for determining the behavior of the system in the neighboring regions. Although quantum phase transitions between distinct ground states occur at absolute zero temperature, their effects may be observed over a range of non-zero temperatures and might also effect the normal state properties. A QCP has been theoretically predicted [87, 88], measurements of the London penetration depth [89] support a quantum critical point of view and experimental efforts have observed anomalous normal state electronic properties in the resistivity [90, 91], optical conductivity [92], thermal [93] and NMR [94] studies that would explain the non Fermi liquid behavior of the metallic state and therefore support the quantum critical scenario. On the other hand, other explanation related to a co-action between correlation effect and the particular Fermi surface topology could be plausible to explain the emergence of high-T_c superconductivity and the strange normal state properties. Thus, despite many years of intense research, there is still no consensus and a universally accepted scenario explaining superconductivity in these materials has not emerged.

Co-substituted $BaFe_2As_2$

In this work, the focus is on parent and Co-substituted (i.e. electron doped) $BaFe_2As_2$, which belongs to the '122' family of the Fe pnictides. Therefore, a more specific description of the properties of this material will be supplied in this section.

A typical phase diagram is shown in fig. 3.3(a). At high temperatures the parent compound has body-centered tetragonal structure and is a bad paramagnetic metal, characterized by non-Fermi liquid behavior. Below the Néel temperature $T_N = 140\,\mathrm{K}$ the system experiences an antiferromagnetic transition and the magnetic moments of the Fe ions form a commensurate stripe-like spin density wave (SDW) modulation [96]. The SDW transition is accompanied or slightly preceded by a structural tetragonal-to-orthorhombic transition [97, 98, 9], with antiferromagnetic ordering along the slightly longer a-axis and ferromagnetic alignment along the shorter b-axis. Both these structures are schematically shown in fig 3.3(b). In the undoped 122 compounds, the structural and magnetic transitions occur simultaneously and gradually become distinct upon doping [95], whereas in the 1111 compounds, the structural transition precedes the magnetic transition also in the undoped compounds. Moreover, above the structural transition, nematic order sets in [99, 100, 101], characterized by broken rotational

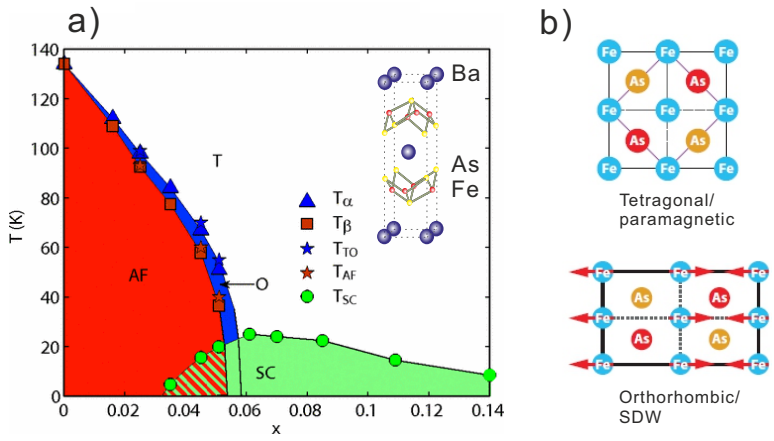

Figure 3.3: (a) phase diagram of $Ba(Fe_{1-x}Co_x)_2As_2$, adapted from [95]. The red dome is the antiferromagnetic state and the green dome is the superconductive state. For underdoped compound a coexistence of these two states is found. The blue area mark the tetragonal to othorhombic transition occurring slightly before the AFM phase. A schematic of the crystal structure is reported in the inset. (b) schematic structure of the tetragonal paramagnetic phase at $T > T_{Neel}$ and of the orthorhombic SDW phase, where the magnetic moments of the Fe ions align antiparallel to each other.From [9].

symmetry while preserving the translational one. By doping the system with electrons, namely systematically substituting Fe with Co, the AFM order is gradually suppressed and superconductivity sets in, although a coexistence with the AFM phase is found for slightly underdoped compounds [102, 103]. In general, superconductivity can be achieved also by hole-doping (i.e. substituting Ba with K) or by isovalent doping (substituting As with P), as well as macroscopically applying pressure to the system.

Fig 3.4 shows the band structure in the vicinity of the Fermi level for the parent compound, above and below the AFM transition temperature and the corresponding Fermi surfaces. In the normal state (Fig. 3.4(a) and (b)), the multiband structure has a semi-metallic character and forms a Fermi surface consisting of three hole pockets at the center of the Brillouin Zone (Γ-point) and two electron pockets at the zone corner (X-point), which are partially nested by the wave vector $\mathbf{q}_{SDW} = (0, \pi)$ [104]. Due to this particular Fermi surface topology, at sufficiently low temperature (below T_N), the SDW transition occurs and, as a consequence, the electron bands backfold to Γ, where they strongly hybridize with the non-folded states, leading to the opening of energy gaps (Fig. 3.4(c) and (d)). In this respect, ARPES has proven to be a powerful tool in the studies of these materials, due to its ability to resolve complex band structure [9]. An important remark is that the Fermi surface is often considered in the purely 2D Brillouin zone of the one-iron unit cell. In reality, they are quasi-2D and warp (disperse) along the third direction of the wave-vector space, to a different degree depending

on the material [83, 28]. Figure 3.4 (e) shows the 3D Brillouin zone with the high symmetry points. Consideration about the 3D character of the Fermi surface will be taken into account in chapter 5 describing and discussing our results as, due to our photon energy of 6 eV, photoemission is performed at a finite $k_z \neq 0$, which has some implications on the effects we observe.

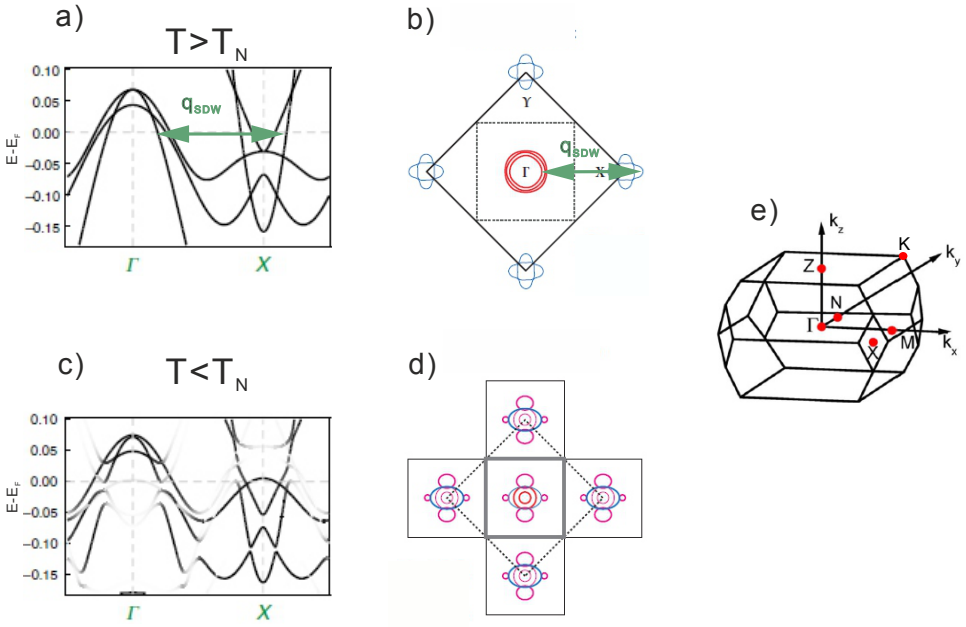

Figure 3.4: (a) and (c) schematic of the expected evolution of the band structure across T_N, along the high symmetry direction $\Gamma - X$. The band structure in the tetragonal paramagnetic state shows hole pockets at Γ and electron pockets at X, visible in the correspondent FS in (b) and (d). The green arrows represent the nesting vector. In the antiferromagnetic phase, SDW folding and gapping are shown. Adapted from [105, 9]. (e) 3-dimensional Brillouin zone in the paramagnetic, tetragonal phase. High symmetry points are labeled. Taken from [97]

3.2 Properties of the 1T-TaS$_2$ System

1T-TaS$_2$ is a layered transition metal dichalcogenide. This class involves materials with the general formula MX$_2$ with M being a transition metal (Mo, Ta, W, etc.) and X a chalcogen (S, Se, Te, etc.). The common structure consists of X-M-X planes forming "sandwiches"that can stack in a variety of ways, from pure octahedral ($1T$) or pure trigonal prismatic ($2H, 3R, 4Hc$) or mixed coordination polytypes. The bonding within the sandwiches is covalent, while between them, it is weak and of van der Waals type. The crystal structure of 1T-TaS$_2$ in the inset of figure 3.5(a) shows the planes of Ta atoms, surrounded in an octahedral arrangement by S

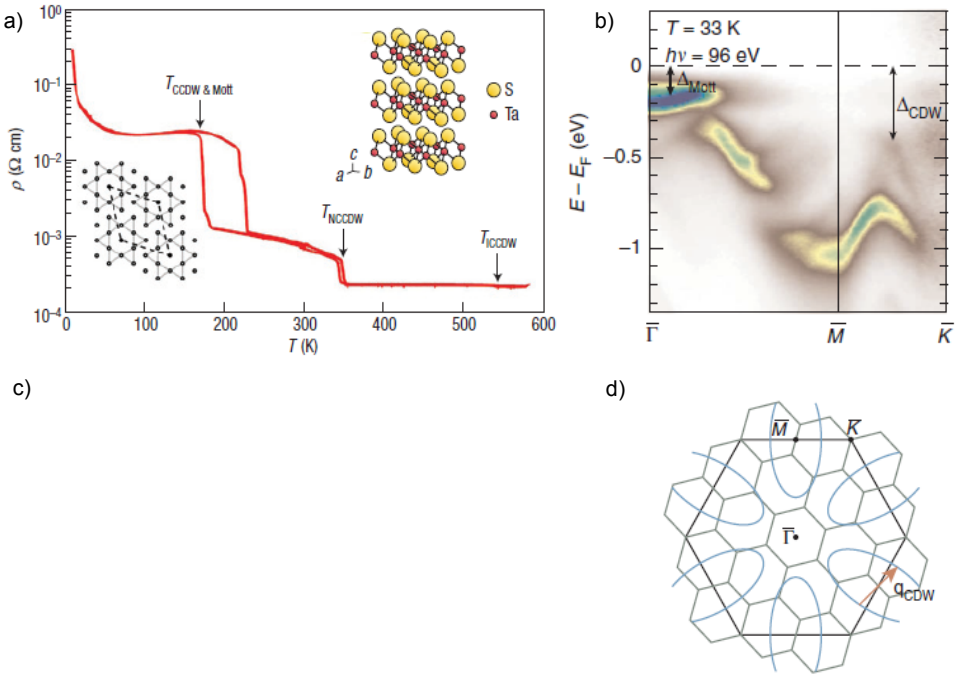

Figure 3.5: (a) Ambient pressure phases of $1T - TaS_2$ and crystal structure (inset), from [18]. (b) Ta atom distortion in the cCDW phase, where the new superstructure $\sqrt{13} \times \sqrt{13}$ is formed (yellow area). The arrows depict the direction of atom movement. From [22]. (c) Measured band dispersions along the $\Gamma - M - K$ high-symmetry path for the $\sqrt{13} \times \sqrt{13}$ phase of $1T - TaS_2$. (d) Reconstructed (cCDW phase) and original (metallic phase) projected Brillouin zone. High symmetry points are indicated. From [8]

atoms. Already at ambient pressure, a variety of phases have been documented [15, 106, 107], from metallic to charge-density-wave (CDW) and Mott-insulating. An overview of these phases is given by the temperature dependent resistivity shown in figure 3.5(a). At high T the system is a metal. Upon cooling, the material forms CDW transitions of different commensurability, accompanied by periodic lattice distortion [15, 108]. Below $T = 550\,K$ there is an incommensurate CDW (iCDW), followed by a nearly commensurate (nCDW) below $T = 350\,K$ and a commensurate (cCDW) phase occurring at $T < 180\,K$. The associated periodic lattice distortion consists in the contraction of the hexagonal arrangement of Ta atoms, forming domains of "David-star"-shaped polaron clusters, as sketched in figure 3.5(c), where twelve of the Ta atoms within the layer move inwards towards a thirteenth central Ta atom. These domains start being locally confined in the iCDW and evolve in a more long range structure across the nCDW phase, until the stars interlock in the cCDW phase by forming a $\sqrt{13} \times \sqrt{13}$ triangular superstructure. This distortion reduces the size of the Brillouin zone leading

to the backfolding of the Ta 5d band manifold, splitting off several umklapp "shadow" bands [109, 18]. CDW-induced gaps open at the new Fermi crossing and only a narrow band is left at the Fermi level [110, 111]. At the same time, intracluster Coulomb repulsion among electrons increases and the system stabilizes by developing a Mott-Hubbard transition which further splits the topmost band in an unoccupied upper Hubbard band (UHB) and an occupied lower Hubbard band (LHB), separated by a few hundreds meV gap [112], turning the system into an insulator. The occupied band structure of the material in this phase is shown in figure 3.5(b), where the Mott gap at Γ and the CDW gap between $M - K$ are also indicated, while the corresponding projected Brillouin zone is depicted in figure 3.5(d). Recent experiments [18] have shown that at elevated pressure the cCDW-Mott phase melts in favor of a textured nCDW state and by applying a pressure larger than 2.5 GPa, 1T-TaS_2 is driven into a superconductive state with the critical temperature $T_c = 5\,\mathrm{K}$.

The above scenario, in which the cCDW coexist with Mott states is widely accepted and experimental evidence for the presence of Mott physics in 1T-TaS_2 has indeed been obtained by time-resolved spectroscopies, which observed the ultrafast collapse of a charge excitation gap, which has been interpreted as a fingerprint of significant electron-electron interaction [19, 20, 48, 8]. However, a recent work [113] challenges this view, offering an alternative explanation for the gap opening at Γ, involving a complex orbital texturing that would develop within the two-dimensional TaS_2 layers and is intertwinned with the CDW. Although the findings in [113] do not exclude the presence of electron-electron interactions, they strongly argue against U being the main cause for the gap at Γ. In this frame, our time-resolved photoemission study is a valid contribution and we already anticipate that our results are partially incompatible with this recent established explanation (see chapter 6.

Chapter 4

Experimental details

TrARPES combines the experimental approaches of femtosecond pump-probe techniques with photoemission spectroscopy, resulting in a unique tool that enables access to the non-equilibrium electronic structure of solids, monitoring their dynamics as function of energy, momentum and time. The experiments presented in this thesis work were performed in the trARPES laboratory at the University of Duisburg-Essen by the group of Prof. Uwe Bovensiepen and consists of three major parts that will be discussed in the present chapter, that is, the laser system, the ultrahigh vacuum (UHV) chamber and the time-of-flight (TOF) spectrometer. The vacuum vessel, as well as the TOF analyzer, were moved at the University of Duisburg-Essen in 2011 from the group of prof. Martin Wolf at Free University of Berlin, while the commercial laser system was bought and set up in the same year.

4.1 Laser source

The various elements of the laser system and the generation of the 1.5 eV pump and 6 eV probe pulses are sketched in figure 4.1 and will be briefly introduced in the following. Further details can be found in previous phD theses [114, 69, 115, 116] and in the technical documentation [117, 118, 119]. Prerequisites for the generation of ultrashort laser pulses in the time-domain are a large bandwidth of the laser spectrum in the energy domain and the realization of phase-coherence of the various cavity modes, the so-called mode-locking. The first requirement is fulfilled by the Ti-doped sapphire (Ti:Sa) crystal, the gain medium of the oscillator cavity, which has a broad emission spectrum 670−1070 nm and low absorption efficiency in the infrared range, allowing efficient pumping with a frequency doubled solid state laser (at 532 nm). Passive modelocking is achieved in Ti:Sa based oscillators with the linear optical Kerr effect [120]. The system is pumped by the output of a 18 W continuous wave (cw) solid state laser (Coherent Verdi V-18). A smaller fraction (about 5 W) is used to pump the Ti:Sa seed oscillator

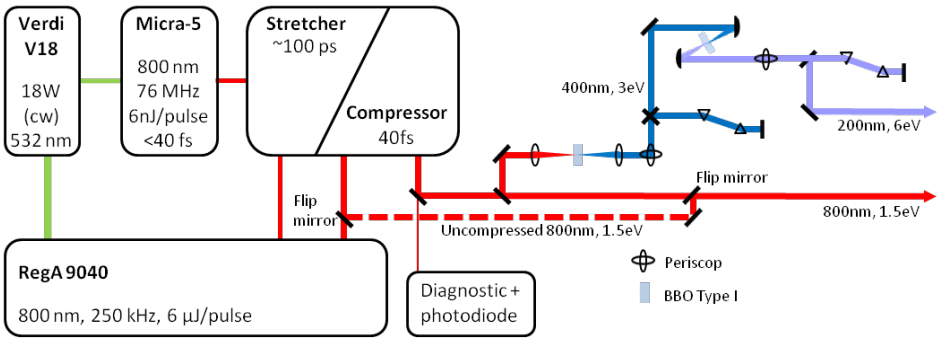

Figure 4.1: Sketch of the amplified laser system and optical setup for the generation of the 6 eV probe beam. Femtosecond IR laser pulses are generated in the Ti:Sa Micra oscillator and subsequently amplified. A flipping mirror placed between the amplifier and the compressor can be used to collect the uncompressed RegA output, used for the switching experiment on $1T$-TaS_2. The beam is split and one part is used as IR pump, while the rest is used to generate the 6 eV probe through a double consecutive SHG process.

(Coherent Micra-5), which delivers femtosecond laser pulses with a central wavelength of $\lambda_0 = 800$ nm and a pulse duration of 40 fs at a pulse energy of ≈ 6 nJ. The central wavelength λ_0 can be tuned from 780 nm to 830 nm. In order to study samples under strong optical excitation conditions, that allow e.g. to induce optical phase transitions, and in particular for the case of $1T$-TaS_2 (see chapter 6), pulse energies of a few μJ are necessary. This is achieved in the regenerative amplifier (Coherent RegA 9040), which is pumped by the remaining output of the Verdi V-18 pump laser. In order to avoid peak powers exceeding the damage threshold of the Ti:Sa crystal in the RegA, the pulses of the seed oscillator are stretched in time before amplification to ~ 100 ps pulse duration. For amplification of the seed pulses in the RegA cavity, a large population inversion is built up in the Ti:Sa crystal due to the suppression of spontaneous lasing by an acousto-optic modulator (Q-switch). This population inversion is used to amplify a seed pulse during several round trips (typically 20-25) in the RegA cavity, which is coupled in and out by another acousto-optic modulator (Cavity dumper). After this process, IR pulses with an energy per pulse of $\approx 6\,\mu$J and the repetition rate of 250 kHz are obtained. The amplified pulses are finally re-compressed to around 40 fs pulse duration by a grating compressor. The RegA pulses are linearly polarized with the polarization vector parallel to the laser table (p-polarization).

Laser setting for different experiments

For the trARPES experiments, 50% of the RegA output was used as pump and the other half of the beam was used to obtain the 6 eV probe beam

by two subsequent second harmonic generation (SHG) processes employing two type 1-BBO crystals. As the SHG process yields s-polarized second harmonic radiation, after each SHG stage, the polarization is flipped back to p-polarization by periscopes and the pulses are recompressed using prism pair compressors, as shown in figure 4.1.
For the trARPES experiments on the Co-doped $BaFe_2As_2$ samples, the central wavelength of the Micra output was set to 830 nm, which yielded a final output from the RegA of 820 nm (1.5 eV), in order to better fulfill the phase matching conditions in the second SHG process. The time resolution achieved in this case was about 90 fs. However, for this setting of the Micra oscillator, the output power is usually reduced with respect to the standard setting providing $\lambda_0 = 800$ nm. While this was not an issue for the experiment on Co-doped $BaFe_2As_2$, where the amount of energy deposited in the system was sufficient to observe the effect discussed later in chapter 5, for the experiment conducted on $1T$-TaS_2 a higher amount of energy was required, in particular to achieve the switching to a metastable state. Therefore, the standard setting of the oscillator were used in this case, which led to a slightly lower time resolution of around 110 fs. During the switching experiment on $1T$-TaS_2 it was necessary to illuminate the sample with an intense train of ps pulses before proceeding with the pump-probe measurements (see Chapter 6). For this purpose, the uncompressed output beam of the RegA amplifier was collected by a flipping mirror, placed before the compressor and redirected towards the last part of the laser table for the beam incoupling (section 4.3) as sketched in figure 4.1.

4.2 UHV chamber and TOF spectrometer

Since ARPES is a surface sensitive technique (see section 2.2), the use of ultrahigh vacuum (UHV) conditions, with pressure $p < 10^{-10}$ mbar, is essential in order to preserve the desired clean sample's surface. In addition, the mean free path of electrons has to be larger than the distance between the sample and the detector, which is only fulfilled for sufficiently good vacuum conditions. The second main part of our experimental setup is the UHV chamber, depicted in figure 4.2, which is divided into two levels, separated by a gate valve. The chamber is equipped with a sample transfer and storage system (not shown), which allows to exchange samples without breaking the UHV conditions.
The upper level is evacuated by a turbo-molecular pump to $p < 1{\cdot}10^{-10}$ mbar, which is connected to a pre-vacuum of $p \sim 10^{-6}$ mbar obtained by a drag-turbo pump and a four-stage membrane pump. In this upper part, samples are inserted from the magazine compartment and connected to the bottom of a 400 mm liquid helium flow cryostat which is equipped with a heating coil and a silicon diode for temperature control, performed by a proportional-

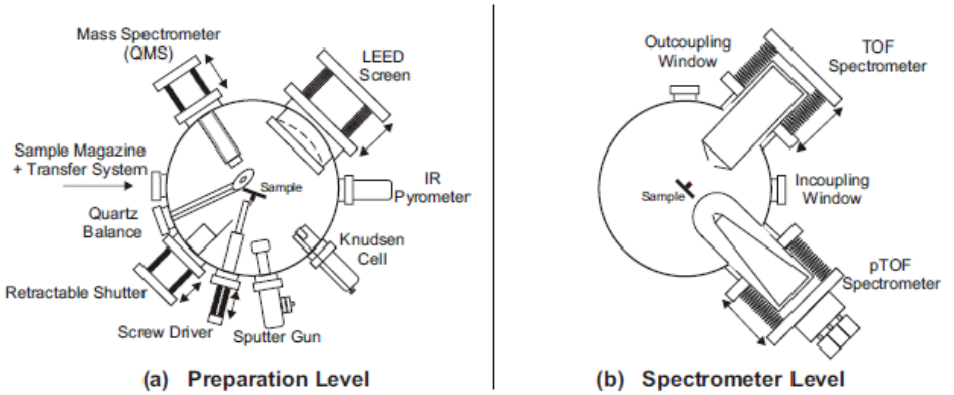

Figure 4.2: Sketch of the UHV chamber. (a) The upper preparation level is connected to a sample transfer system and is equipped with various tools for sample preparation and characterization. A screw driver is used to cleave small crystals of layered materials. (b) The lower level is separated from the preparation level by a gate valve and houses the TOF and pTOF electron spectrometers. Taken from [69]

integral differential (PID) controller (Lakeshore 330). Thereby, the sample temperature can be controlled and stabilized within a temperature range from $\sim 350\,\mathrm{K}$ down to $\sim 30\,\mathrm{K}$, necessary for T-dependent measurements. The cryostat is mounted on a sample manipulator allowing for 400 mm vertical and $\pm 12.5\,\mathrm{mm}$ lateral movements. In addition, a differentially pumped rotation feedthrough enables free 360° rotation around the vertical axis of the manipulator. All linear movements are equipped with computer controlled stepper motors which allow for sample positioning with $\sim 10\,\mu\mathrm{m}$ precision. In the upper level samples are prepared and for this purposes the chamber is equipped with several devices as a Pb- or In-evaporator, two gas dosers and a sputter gun. To check the sample quality a low-energy electron diffraction (LEED) device is used and a quadrupole mass spectrometer (QMS) is available for the preparation of noble metal surfaces, as well as for checking the presence of residual gas in the chamber. The samples under investigation for this thesis work, were all single-crystal layered materials which required no special preparation inside the chamber but only cleaving. The sample was fixed on the sample holder and a ceramic post was glued on the sample upper surface. After inserting the sample in the chamber, it was cleaved *in situ* with the help of a screw driver attached to a movable bellow used to remove the post.
The lower level is evacuated by an ion getter pump and a titan sublimation pump to a base pressure of $p < 3 \cdot 10^{-11}\,\mathrm{mbar}$, which allows to maintain clean sample surfaces over very long measurement times of several hours up to days, necessary for trARPES measurements. It houses the two time-of-flight (TOF) spectrometers used for electron detection, the conventional

TOF spectrometer, used for the present work, and the newly built position-sensitive time-of-flight (pTOF) spectrometer.

The time-of-flight spectrometer

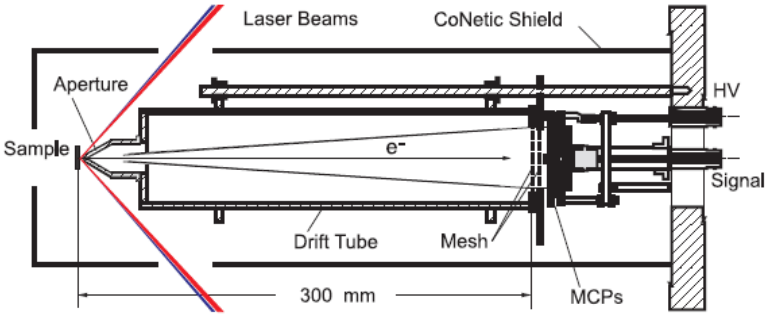

Figure 4.3: The conventional time-of-flight (TOF) spectrometer with 300 mm drift length and an angular acceptance of $\pm 3.8^o$. Taken from [114].

The conventional TOF spectrometer was used for all the measurement presented in this thesis and is depicted in figure 4.3. The kinetic energy of the photoelectrons that enter the spectrometer through the entrance tip is detected by their flight time t in the field-free drift tube of length $L = 300\,\text{mm}$. For non-relativistic electrons, with mass m_e, the kinetic energy is given by

$$E_{kin} = \frac{1}{2} m_e v^2 = \frac{m_e L^2}{2t^2} \tag{4.1}$$

which is determined with respect to the vacuum potential of the spectrometer. The electrons have to overcome a potential $e_0 U$ which is determined by the offset of the work functions of sample and spectrometer Φ_{sample} and Φ_{spec}, respectively, as well as an optionally applied bias voltage U_{Bias}:

$$e_0 U = \Phi_{sample} - \Phi_{spec} + e_0 U_{Bias}. \tag{4.2}$$

A schematic energy diagram of the potentials between sample and spectrometer is shown in figure 4.4.

Photoelectrons are detected by a pair of micro channel plates (MCPs) in a chevron configuration with 40 mm diameter, which defines the acceptance angle of 3.8°. Drift tube and entrance aperture are coated by graphite to ensure a homogeneous work function of the spectrometer of $\Phi_{spec} \approx 4.3\,\text{eV}$. In addition, the whole spectrometer is housed in a μ-metal shielding to avoid external magnetic fields, which distort the trajectories of the slow photoelectrons of a few eV kinetic energy. The energy and momentum resolution of the TOF spectrometer depend on the kinetic energy of the

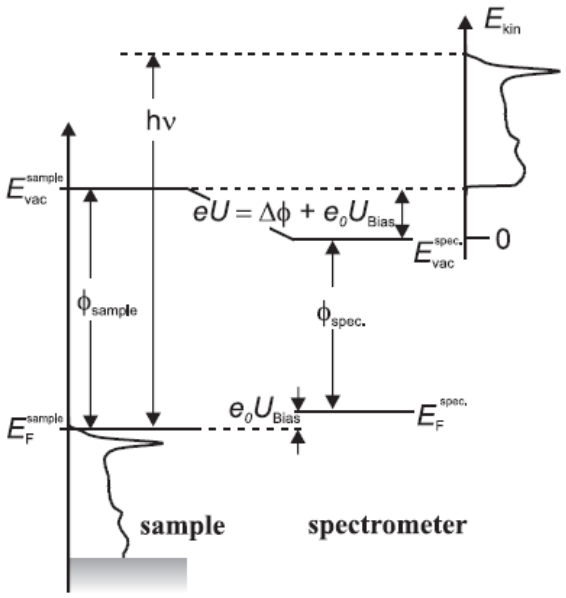

Figure 4.4: Potential gradients between sample and spectrometer. If sample and spectrometer are directly connected ($U_{\mathrm{Bias}} = 0$), both Fermi levels aligned. A finite value of U_{Bias} allows to compensate a difference in sample and spectrometer work function and to eliminate electric fields between sample and spectrometer entrance, important for the angle-resolved detection of electrons. The kinetic energy is referenced to the vacuum level of the spectrometer, and the vacuum level of the sample defines the secondary cutoff position. Taken from [114].

photoelectrons and amounts to $\Delta E_{kin} \approx 20\,\mathrm{meV}$ and $\Delta k_{\parallel} \approx 0.01\,\mathrm{\AA}^{-1}$ at $E_{kin} = 2\,\mathrm{eV}$, respectively [Hot99]. The effective energy resolution of the experiment is determined not only by the spectrometer resolution but also by the spectral width of the probe pulses and amounts to typically 50 meV with the 6 eV probe beam used for trARPES.

The pTOF spectrometer was not used for the measurement shown in this thesis. However it is a unique device widely used in the performance of trARPES and tr2PPE experiments on several materials. For this device a two-dimensional position-sensitive detection scheme was realized, allowing for an angle dispersive detection of photoelectrons without rotating the sample. The system has been described in details in [121, 114].

4.3 Beam incoupling and measurement preparation

In figure 4.5 a more detailed sketch of the last part of the optical setup shows how the beam incoupling is achieved in our experimental geometry. The

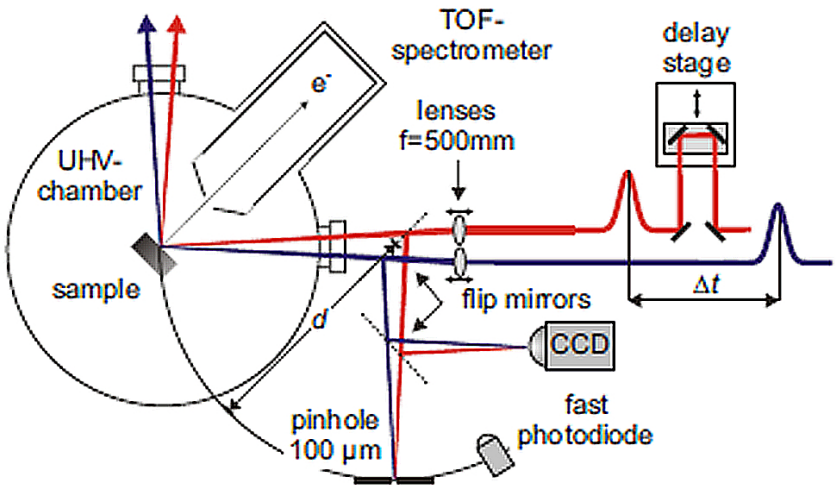

Figure 4.5: Beam incoupling into the UHV chamber. Pump (red) and probe (blue) beams are independently focused onto the sample in front of the TOF spectrometer by two lenses. A computer controlled delay stage is used to vary the time delay between the pump and probe pulses. The spatial overlap of pump and probe beams on the sample is verified by a pinhole outside the UHV chamber and the beam profile is monitored by a CCD. To establish the coarse temporal overlap of pump and probe beam, a fast photodiode is used. Taken from [69].

pump beam traverses a computer controlled motor stage with a minimum step size of 0.5 fs (Physik Instrumente), which controls the temporal delay between the pump and the probe pulses. The two beams are then focused separately by two lenses ($f = 500\,\mathrm{mm}$) onto the sample surface inside the UHV chamber in front of the TOF spectrometer aperture, allowing for the independent control of the focal diameters on the sample. To verify the spatial overlap of the two beams outside the UHV chamber, a flipping mirror can be used to reproduce the sample position onto a 100 μm pinhole, which is mounted at the same distance d to the mirror as the sample position. The quasi-collinear geometry allows to maintain the spatial overlap even for slight sample movements that are unavoidable in angle-dependent measurements. In addition, a CCD can be used to monitor the beam profiles of the two beams (figure 4.6) and the temporal overlap of the two pulses is established within $\sim 100\,\mathrm{ps}$ using a fast photodiode. The femtosecond temporal overlap is found from the transient photoemission signal.

The incident pumping fluence on the sample is determined by the beam profile of the pump beam at the sample position, which can be measured by the CCD mounted in a similar manner as the pinhole at the sample distance to the focusing lenses. Typical beam profiles of pump and probe beams are shown in figure 4.6, which are fitted with Gaussian line profiles to determine the beam diameters. Here, the probe beam diameter is usu-

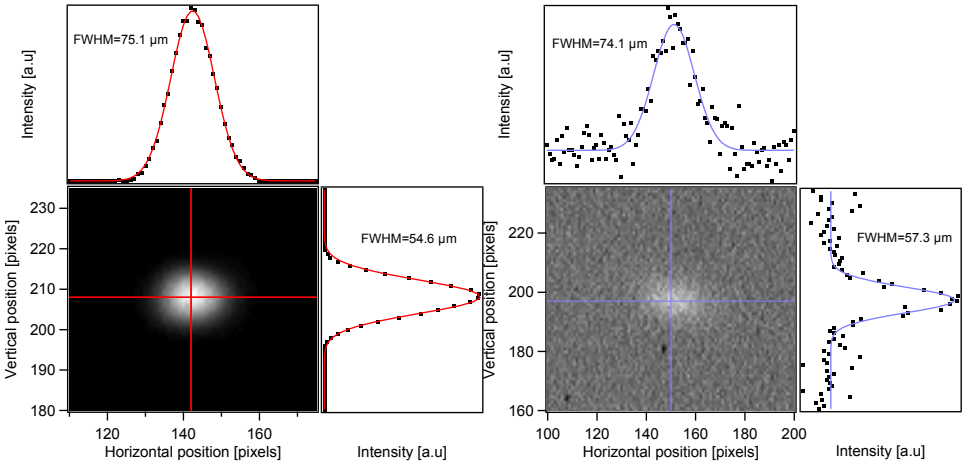

Figure 4.6: Exemplary pump ($h\nu = 1.5\,\mathrm{eV}$) and the probe ($h\nu = 6\,\mathrm{eV}$) beam profiles, recorded with the CCD in the focal plane of the sample. Horizontal and vertical beam diameters are determined by the FWHM of Gaussian line fits.

ally chosen smaller than that of the pump beam to ensure a homogeneous pumping within the probed region of the sample. For the determination of the incident pumping fluence F_{in}, the horizontal and vertical FWHM of the pump beam is taken as the beam diameters a and b and the incident pumping fluence is determined by

$$F_{\mathrm{in}} = T\frac{P\cos\alpha}{f}\frac{1}{\pi ab}, \tag{4.3}$$

where $T = 0.95$ is the transmission of the UV transmitting incoupling window, f the repetition rate, P the laser power as measured with a power meter in front of the UHV chamber and α the angle of incidence on the sample, which corresponds to 45^o in normal emission geometry. Typical pumping fluences in the trARPES measurements ranged from few tens of $\mu\mathrm{J/cm^2}$ to few $\mathrm{mJ/cm^2}$ and could be adjusted by using a combination of non dispersive filters. The error on the absolute fluences is estimated to be around $10 - 20\%$ and is mainly determined by the sensitivity of the power meter ($0.1\,\mathrm{meV}$) and the error in determining the beam size.

Chapter 5

TrARPES on FePn

The discovery of Fe-based high-T_c superconductivity is one of the breakthroughs in the last two decades of condensed matter research because in addition to the cuprates scientists identified a second class of compounds displaying superconductivity with high T_c enhancing the interest and hope in explaining this phenomenon. However, the richness of the physics contained in these materials does not make things smoother and continuously triggers new challenges in the research [84]. Understanding the microscopic origins of electronic phases in high-T_c superconductors is important for elucidating the mechanism of superconductivity.
The material properties, phase diagrams, and the electronic structure of the various compounds of the pnictide family, and of this compound in particular, were discussed in chapter 3. There, we mentioned that both quantum criticality, which focuses on the role of magnetic fluctuations at the QCP, and other properties related to correlation effect together with the particular topology of the Fermi surface are at the center of the current debate in explaining the origin of superconductivity and "bad metal" properties of the normal state. In this frame, further study is required and unraveling the elementary excitations governing the semi-metallic ground state and the coupling between low energy excitations like spin fluctuations and lattice vibrations may be an important step towards the understanding of superconductivity in the HTSCs. One promising approach to do so is to analyze the transient state of the optically excited materials and their relaxation. Tr-optical reflectivity [122, 123, 124, 125, 126] and trARPES [54, 127][81] had been important to quantify the electron-phonon coupling strength in the system under non-equilibrium conditions, as well as to characterize the AFM phase. However, no systematic doping dependent studies have been reported in the case of trARPES. The importance of such studies becomes obvious if we consider that chemical doping is the key parameter enabling the system to evolve through its different thermodynamic phases.

In this chapter we report on a systematic trARPES study on parent

($T_N = 140\,K$) and Co-substituted, i.e. electron doped $BaFe_2As_2$ with optimal ($x = 0.06$, $T_c = 23\,K$) and overdoped ($x = 0.14$) Co concentration x, to investigate the influence of doping on the dynamics of the system. By analyzing the hot electron population decay as a function of binding energy we find a trend of the relaxation for different doping in agreement with transport measurements and a blocking of the relaxation at energies below 200 meV. The latter indicates coupling to a boson which is most probably of magnetic origin. We discuss our results in the context of the latest developed scenarios. Part of the results reported in section 5.2 have been published in [**128**], which was entirely written by myself.

5.1 Equilibrium electronic structure

In the first subsection we will show some selected results from static ARPES measurements conduced at the synchrotron radiation facility BESSY II. The outcome of such experimental efforts, performed in collaboration with Prof. Jörg Fink from the Leibniz-Institute for Solid State and Materials Research Dresden and Emile Rienks from the Helmholtz-Zentrum Berlin, which are the main contributors, where published in **[30, 31]**. Here, we will not show the complete analysis of such data, which is beyond the scope of this thesis, but only the relevant aspects in the context of the trARPES results object of this dissertation.

5.1.1 Electronic structure from high-resolution ARPES

Before proceeding with the description and analysis of the trARPES data, we first discuss the equilibrium electronic structure. Since with the 6 eV probe photon energy available in the trARPES setup, the accessible momentum range is only limited to the BZ center, and only the hole pocket can be observed, we will first provide some exemplary high-resolution ARPES dispersions that were recorded at the synchrotron radiation facility BESSY II together with Prof. Jörg Fink from the Leibniz-Institute for Solid State and Materials Research Dresden and Emile Rienks from the Helmholtz-Zentrum Berlin. The employed photon energies between $h\nu = 20 - 130\,\mathrm{eV}$ allowed to reach all the high symmetry points and a more complete view of the electronic structure can be given. The measurements were carried out at the UE112-PGM2a beam line with the "1^2"-ARPES end station, equipped with a Scienta R8000 analyzer. The total energy resolution was $10 - 15\,\mathrm{meV}$, while the angular resolution was $0.2°$. All measurements were performed in the paramagnetic and non-superconducting range near $T = 30\,\mathrm{K}$. In figure 5.1 representative intensity plots as a function of binding energy and parallel momentum are shown for the optimally doped compound ($x = 0.06$), measured near the four high-symmetry points Γ, Z, X, and K (see figure 3.4 (e)), along the k_y-direction (parallel to the Fe-Fe direction). The dispersions at Γ, X and K were recorded using s- (perpendicular to k_x) polarized light, while at Z, p (parallel to k_x) polarized light. At Γ and Z bands having predominantly Fe 3d xz/yz orbital character are detected, that forms two inner hole pockets. which are almost degenerate at Γ (5.1(a)). For p-polarization we detect in addition bands with predominantly xy and z^2 orbital character, forming the outer hole pocket. While the inner and outer hole pockets are almost degenerate at Γ (for both s and p polarization), they are clearly separated at the Z point (5.1(c)). At X and K the electron pockets are detected which are formed from d bands with predominantly xz/yz character, while (not shown) for p-polarization the spectral weight is rather small due to matrix element effects. Using momentum distribution curves the dispersion

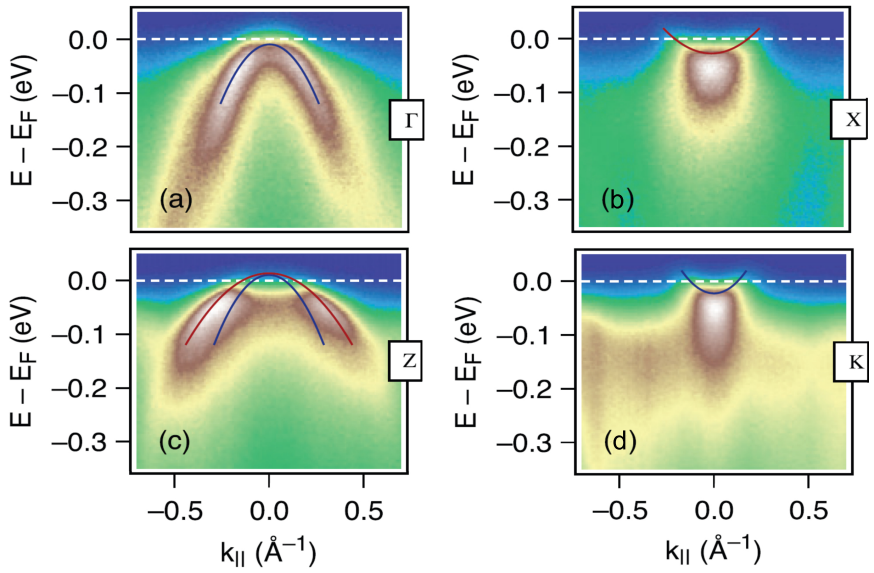

Figure 5.1: Intensity plots as a function of binding energy and wave vectors along the k_y-direction for $x = 0.06$ near the high-symmetry points Γ(a), X (b), Z (c) and K (d). The spectra near , X, and K were recorded with s-polarized photons, while the spectrum near Z was measured with p-polarized photons. The red/blue lines represent parabolic bands derived from least-squares fits. From **[30]**

of the bands was determined, approximated by a second-degree polynomial, and the results are shown in figure 5.1 by red and blue lines indicating the inner and outer pockets, respectively. Here we intend to remark one aspect that will be useful in discussing the results presented in the next section, that is, the different size of the hole pockets at the two different high symmetry points. While at Γ the bands forming the hole pockets are tangential to the Fermi level, and the hole pocket is thus reduced to a point, at Z the pockets structure is still visible. The reason is that for this compound, and especially at optimal doping, a strong dispersion along the k_z direction is found [60, 59, 104] mainly affecting the hole pockets. As a consequence, there is a Lifshitz transition [129, 130]**[31]**, consisting in the change of the Fermi surface from a cylinder along the k_z-direction to an ellipsoid around the Z-point, as we will show more in detail in the next section. The momentum distribution curves (MDC) at different binding energies were fitted with lorentzian lines, which corresponding line widths Γ yields values for the imaginary part of the self energy $\Sigma'' = \Gamma/2 = \hbar/2\tau$, that contains the information on the broadening of the lifetime τ of the corresponding states (see section 2.2). Therefore, the line widths analyzed in ARPES, are a direct measure of the scattering rates. In figure 5.2 (a) the imaginary part of the self energy is shown for the optimally Co-doped compound (red cir-

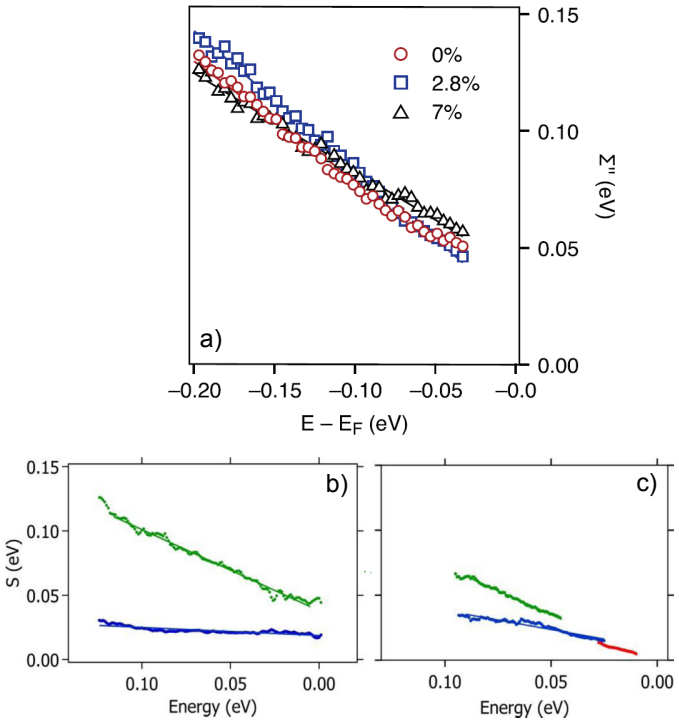

Figure 5.2: (a) Σ'' for the inner hole pocket near the Γ-point as a function of binding energy, obtained from MDC of figure 5.1(a) (optimally Co-doped $BaFe_2As_2$, red circles). The blue square and black triangles indicate the same quantities analyzed from other data on Mn-substituted compounds, which are not discussed here. From **[30]**. (b) Scattering rate $S(E)$ of inner (green) and outer (blue) hole pockets obtained from analogous analysis conduced on $BaFe_2(As_{1-x}P_x)_2$, $x = 0.27$ measured near the Z point with a photon energy $h\nu = 62\,\text{eV}$. (c) Scattering rates of inner (green), central (blue) and outer (red) hole pockets for $NaFe_{1-x}Rh_xAs$, $x = 0.027$ near Γ measured with $h\nu = 21\,\text{eV}$. The corresponding data can be found in **[31]**.

cles) and two others Mn-substituted compounds, which will not be discussed here. The values of Σ'' start from a constant offset of $\approx 50\,\text{meV}$ determined by energy-independent elastic scattering processes [3] and increase linearly with binding energy, which is one manifestation of the "bad-metal" behavior in the normal state of this compounds, as mentioned in the introduction chapter. The slope of $\Sigma''(E)$ is governed by inelastic scattering processes related to electron-electron interaction. In figure 5.2 (c) and (d) scattering rates as a function of binding energy are reported also for a P-doped (isovalent doping) compound, derived from inner and outer hole pockets, and $NaFe_{(1-x)}Co_xAs$, derived from inner, central and outer hole pockets. Also for these compounds a linear dependence from the binding energy is found. In the following sections we will compare such quantities with the scattering rates determined from the analysis of the energy dependent hot electrons

dynamics of parent and Co-doped $BaFe_2As_2$ investigated by trARPES (see section 5.2.2) and discuss the differences in detail.

5.1.2 Electronic structure with 6 eV photon energy

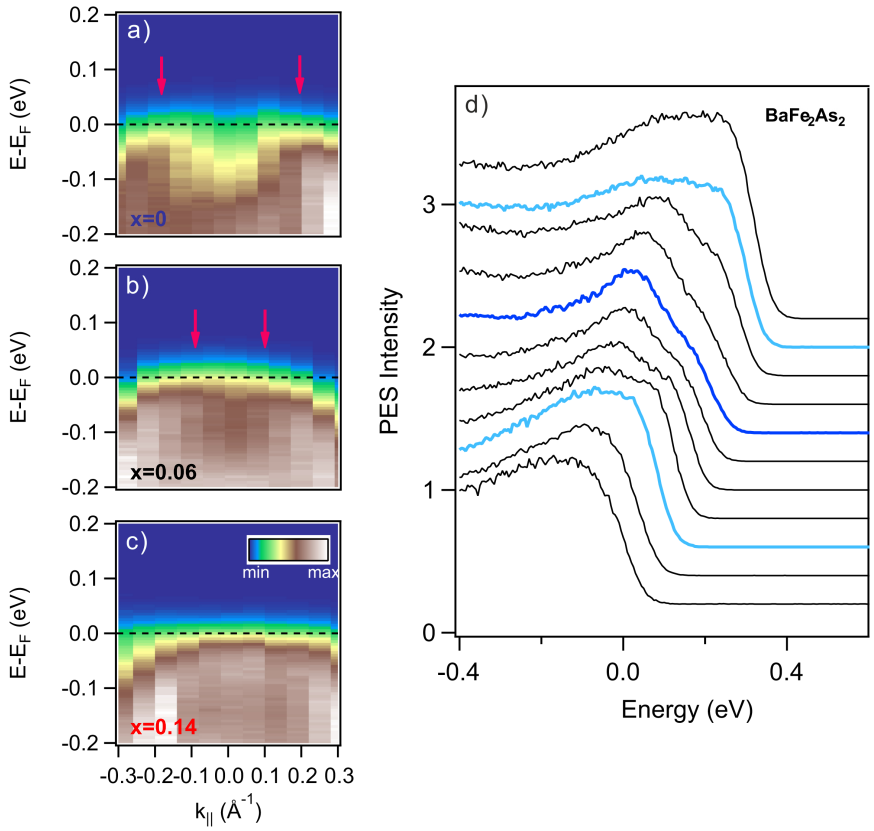

Figure 5.3: (a)-(c) ARPES dispersion around the Γ-point for all compounds, at $T = 30\,\mathrm{K}$. Photoemission spectra taken with a photon energy $h\nu = 6\,\mathrm{eV}$ are plotted as a function of binding energy $E - E_F$ and parallel momenta $k_{\|}$, the red arrows are an indication of the Fermi momenta k_F. The hole pocket structure is clearly visible in the case of the undoped compound (a). With increasing Co-substitution, the chemical potential shifts upwards causing a reduction of the pocket, which is barely visible for the $x = 0.06$ compound (b) and completely disappears for overdoping (c). (d) EDCs of the data in (a), the dark blue and the light blue EDCs are taken at Γ and k_F, respectively. For better clarity the curves are vertically and horizontally offset

A major challenge in investigating the electron dynamics in FeAs compounds with the trARPES setup using 6 eV probe photon energy is the small photoemission cross-section of Fe-derived states at low photon energies, in comparison to the As states [131] and the limited momentum range accessible at low kinetic energies, which limits our investigation to the hole pockets at the Brilloiun zone center. ARPES spectra taken at $T = 30\,\mathrm{K}$ as

a function of parallel momentum are depicted in figure 5.3 in a false color representation, to show the hole pockets' dispersion around the Γ point. For better illustration, panel (d) depicts the Energy distribution curves (EDCs) for the parent compound. Although our energy resolution of $\approx 50\,\mathrm{meV}$ does not enable to resolve the single contributions of the three d-like bands crossing the Fermi level, the overall pocket structure is clearly visible for the parent compound in figure 5.3 (a). The red arrows are an indication of the band crossing and the corresponding spectra at k_F are marked in turquoise in panel (d), while the spectrum at $k_\parallel = 0$, in correspondence of the Γ point, is dark blue. An important point is that in the case of Co-substituted $BaFe_2As_2$, it is reasonable to assume a rigid shift of the bands upon doping. According to the rigid-band model, upon Co-substitution, electron carriers are added to the system, gradually filling the pockets and therefore shifting the chemical potential to higher energies (see figure 5.4 (a)), according to the number of extra electrons x. Several ARPES studies [104, 60, 132] support this assumption and increasing deviations from the rigid-band model are found for Ni and Cu substitution [133] and for isovalent doping [130]. In fact, figure 5.3 (b) shows that the hole pocket is still visible for the optimally doped compound, but with k_F located at smaller values, indicating the shift of the Fermi energy due to electron doping. Finally, panel (c) shows the overdoped compound, where the band is totally located below E_F, as the pocket has been completely filled up. Our observation of a small hole pocket in the optimally doped compound deserves a more detailed discussion where the three dimensionality of the Fermi surface has to be considered. As mentioned in the previous section, several ARPES studies on Co-doped $BaFe_2As_2$ unveiled a strong doping-dependent k_z dispersion of the hole pockets, while the electron pockets are less affected [60, 59, 104]. In order to clarify this point, in figure 5.4 (b) we report exemplary results from literature [60], which shows a comparison of the k_z dispersion of the hole pockets on parent (left panel) and optimally doped (right panel) $BaFe_{2-x}Co_xAs_2$, obtained with high-resolution ARPES measurements at different photon energies. Such figure nicely shows the warping of the hole cylinders along the vertical direction, which is more pronounced in the case of the optimal doping. At optimal doping (right panel of 5.4 (b)) in correspondence of the Γ-point, the top of the hole pocket sinks below the Fermi level and is tangential to E_F, while at Z the hole pocket is still present. This is supported also from the ARPES data shown in figure 5.1 (a) and (c). Thus, the corresponding Fermi surface at Γ would consists of four circles at the BZ boundary (formed by the electron pockets) and one point at the BZ center. By proceeding away from Γ, towards Z, the point at the BZ center should instead evolve in a small ellipse. Our observation of a small remnant hole pocket at optimal doping depends on the k_z position at which we probe. Assuming an inner potential V_0 of 15 eV [59], we

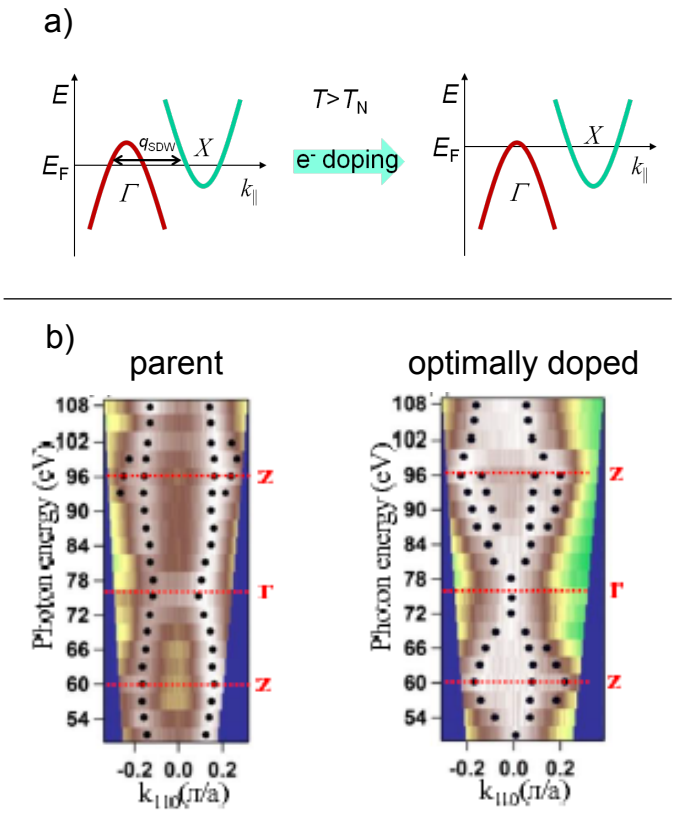

Figure 5.4: (a) Simplified schematics of the band filling effect upon electron doping. The bands at the BZ center and BZ boundary are indicated with a red and green parabola, respectively, with opposite Fermi velocities. In the undoped case, the chemical potential at E_F is crossed by such bands, resulting in a hole and electron pocket, respectively, which are nested by the wave vector $\vec{q}_{SDW}$. By adding electrons to the system, the chemical potential shifts rigidly upwards, the hole pocket reduces in size and the electron pockets enlarge. (b) Photon energy dependent ARPES measurements performed on $BaFe_{2-x}Co_xAs_2$ to reveal the k_z dispersion of the hole pockets as a function of doping concentration, from reference [60]. The cases of the parent and optimally doped compound are reported for comparison.

calculate $k_\perp$ from eq. (2.13), being $k_\perp = 0.512\sqrt{E_{kin} + V_0} = 2.1\,\text{Å}^{-1}$ with a kinetic energy $E_{kin} = 1.6\,\text{eV}$ resulting from the difference of the probe photon energy (6 eV) and the sample work function, which can be determined from the width of the photoemission spectrum. The lattice constant is $c = 13.02\,\text{Å}$ [134, 104], corresponding to $c^* = 2\pi/c = 0.483\,\text{Å}^{-1}$. Therefore, $k_\perp = 4.3c^*$ and we probe a region of the momentum space between the Γ and the Z point (see figure 5.4 (b), right). We will come back to this point later on as it will have some implication in discussing the energy-dependent relaxation times (section 5.2.1).
Due to the warping of the hole cylinders, a Lifshitz transition occurs at

optimal doping [129][**31**], that is, the Fermi wave vector (the radius of the hole pocket) at $k_{\|} = 0$ (Γ) decreases with increasing doping concentration until the pocket vanishes, while at $k_{\|}$ corresponding to Z the Fermi wave vector increases. The huge mass enhancement which derives at this point from the crossing of a flat band at E_{F}, in co-action with correlations effect is discussed as one of the possible ways to explain the non-Fermi Liquid normal state and possibly the superconductivity [135, 136], in contrast to other scenarios, where instead coupling of the charge carriers to magnetic fluctuations at low temperatures in presence of a QCP would play a main role [88, 89].
After the determination and verification of the equilibrium band structure, we could proceed with the investigation of its ultrafast changes after photoexcitation. Since one of our aims was a comparison among different dopings, we carried out our measurement at 160 K in normal emission, to which, for simplicity, we will refer as the Γ-point in the following. Thus, all the compounds have been initially, before optical excitation, in the paramagnetic phase and the only tuned parameter was the electron doping concentration.

5.2 Relaxation of hot electron populations

Having described the static electronic properties, and the ARPES spectra around the Γ-point, the focus will now turn to the dynamics of the system, analyzing the transient pump-induced modifications as function of doping for different fluences. Exemplary trARPES results are shown in figure 5.5 (a) for the parent compound as a function of binding energy and pump-probe delay, at an incident laser pump fluence $F = 540\,\mu\mathrm{J/cm^2}$. Upon photoexcitation one observes an increase of spectral weight up to 1 eV above E_{F} generated by electrons excited from outside the hole-pockets, which subsequently relax to the Fermi level. The modulation of the photoemission signal, superimposed to the incoherent exponential decay is due to the dominant excitation of the A_{1g} phonon mode [122, 78][**81**]. Depletion of spectral weight below E_{F} could also be resolved for intense excitations down to ≈ 100 meV, although it is a much weaker effect due to the presence of a huge background signal. The changes around the Fermi level can be also appreciated by comparing two single spectra taken at negative delay and some tens of femtoseconds after the arrival of the pump pulse, respectively, as shown in figure 5.5 (b). Here we focus on the analysis of the relaxation mechanism of the excited electrons as a function of doping concentration, investigated for pump fluences ranging from $50\,\mu\mathrm{J/cm^2}$ to $540\,\mu\mathrm{J/cm^2}$. As a first step we obtained time-dependent photoemission intensity integrated over the whole energy range of the pump-induced modification, from about $10 - 30$ meV above E_{F} to about 1 eV. The lower limit for the integration was chosen in order to minimize the influence of the transient shift of the chemical potential, induced by the co-

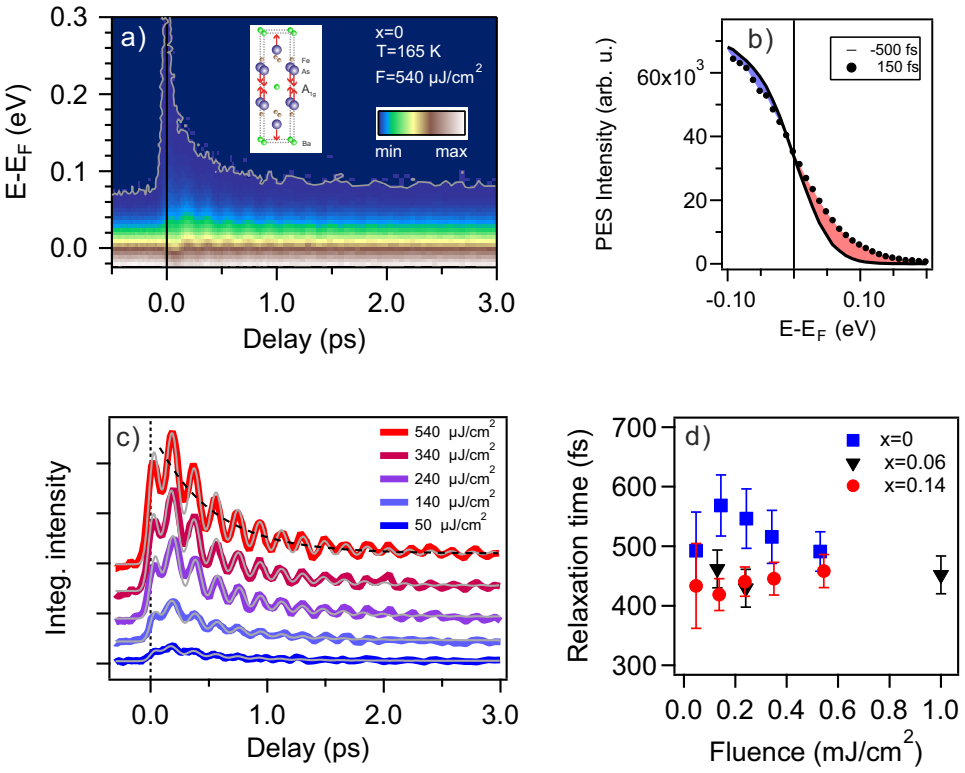

Figure 5.5: (a) trARPES intensity of $BaFe_2As_2$ around the Fermi level as a function of $E - E_F$ and pump-probe delay. The grey contour has been added to further evidence the pump-induced changes. The inset is a schematic of the A_{1g} breathing mode, responsible for the coherent modulation of the signal around E_F. (b) EDC around E_F at negative and positive delay. After excitation, spectral weight is shifted from below to above E_F. (c) Integrated trARPES intensity over an energy range of $\approx 1\,\text{eV}$ above E_F for different fluences as indicated; solid grey lines are fits to the data and the dashed black line shows the exponential decay component of the fit. (d) Relaxation time constants extracted from the fits in c) for the investigated doping concentrations are plotted as a function of incident pump-fluence. From **[128]**

herent oscillations [78]. We describe the obtained time-dependent data with a single exponential decay plus a damped sine function (to account for the coherent oscillations) convoluted with the temporal pump-probe envelope, see figure 5.5 (c). Although here we will not concentrate on the coherent phonons, it was necessary to include their contribution in the fit function in order to obtain a more precise estimation of the maximum amplitude of the pump-induced change (amplitude of the exponential function). The resulting exponential decay fits are in the sub-picosecond timescale, in agreement with previous time-resolved studies [54, 123] and are summarized in figure 5.5 (d) for all samples and for different incident pump fluences. At low fluences, up to $\sim 400\,\mu\text{J/cm}^2$, the parent compound relaxes clearly slower

than the Co-substituted compounds, showing also a dependence on fluence where, except for the first data point, we see a decrease from 570 fs to 490 fs for more than a tripling of F. Such an F-dependence is not observed in this analysis in the case of the optimally doped (OP) and overdoped (OD) compounds, where the relaxation times remain constant but even up to 200 fs shorter. At higher fluences different relaxation times for different doping merge to joint values below 500 fs. At this point we emphasize that the previous analysis accounts for the decay of the energy integrated hot electron population. The dominant contribution comes from the intensity close to E_{F} which is mostly determined by secondary electrons (see section 2.2.2), generated from the $e-e$ scattering at higher energy in a sort of "Auger-like" process [71, 137], which contribute in a far from trivial manner to the relaxation, in addition to $e-ph$ scattering that mediates energy dissipation close to E_{F} [127, 75, 138, 139]. Therefore, the total relaxation times should be considered as an effective characteristic quantity that cannot be compared with single-particle decay times, for example, determined in static ARPES from line width analysis. The reason is that ARPES line widths, which are proportional to the single-particle scattering times, are determined by elastic and inelastic scattering processes of individual quasiparticle excitations, as explained in the previous section, while trARPES analyzes the population decay to which secondary electrons contribute in a complex manner after energy integrating the transient population [62, 140]. We will come back to this point later on, however we remark that nevertheless these effective relaxation times already exhibit a clear doping dependence.
Given these considerations, we can gain further insight from an energy resolved analysis, as different contributions to the relaxation of the excited population dominate at different energies.

5.2.1 Energy-dependent relaxation times and rates

We analyze time-dependent photoemission intensities in different energy windows starting from $\approx 20\,\mathrm{meV}$ to about 1 eV above E_{F}, to obtain energy-dependent relaxation times. For this analysis, it was not necessary to include the contribution of the coherent oscillations, as they strongly affect the photoemission signal only at energies very close to E_{F}. We used a single exponential decay fit function $I = A\exp(t/\tau) + B$ convoluted with a Gaussian function representing the pump-probe envelope, where A is the excitation amplitude, τ the relaxation time and B is a constant accounting for an increased temperature of the electronic system that establishes at long delay time. A detailed inspection of figure 5.5 (a) provides support for this analysis. At $E - E_{\mathrm{F}} = 0.1 - 0.3\,\mathrm{eV}$ an energy dependent relaxation is observed, while below 0.1 eV, where heating will take an effect on the electron distribution, the intensity barely decays up to 3 ps. Some exemplary curves for the fluence of $240\,\mu\mathrm{J/cm^2}$ are shown in figure 5.6 (a)-

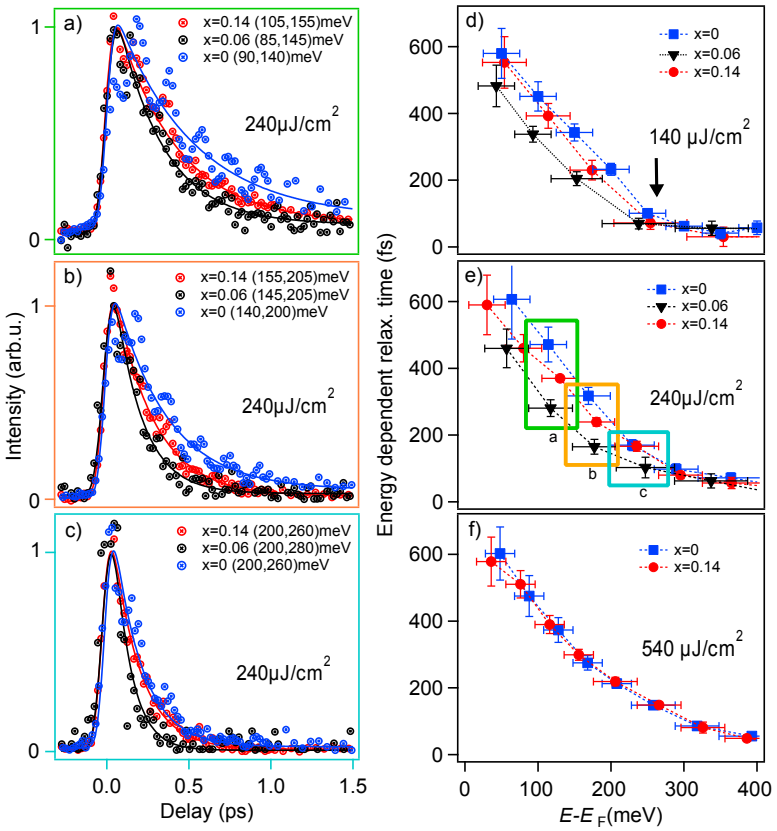

Figure 5.6: (a)-(c) Normalized time-dependent intensity extracted in three consecutive energy interval starting from $\sim 100\,\text{meV}$ above E_F to $\sim 250\,\text{meV}$ at $F = 240\,\mu\text{J/cm}^2$. For each energy interval, all three doping concentrations are shown. Solid lines are exponential fits to the data, convoluted with the pump and probe cross-correlation. (d)-(f) Relaxation times extracted from the fit for all curves at three different fluences as a function of binding energy. Error bars on the energy axis mark the energy intervals of integration, the colored boxes, as well as the letters, in figure 5.6 (e) compare the results of the fits in comparable energy windows for the three dopings to the corresponding experimental data and fit in figure 5.6 (a-c). The integration windows for the curve slightly differ from each others in order to match statistics. The colored boxes in (e) represent the corresponding results of the fits reported in (a)-(c) as indicated by the frame colors and letters. From [**128**]

(c) comparing dynamics of samples with different doping concentration in similar energy windows. The results of the complete analysis on all compounds are shown in figure 5.6 (d)-(f). We observe a dependence on doping until $E - E_\text{F} = 250\,\text{meV}$. As for the total energy-integrated intensities, the parent compound relaxes on a longer timescale than the Co-substituted compounds but it becomes now evident that the $x = 0.06$ (optimally doped) relaxes faster than the $x = 0.14$ (overdoped) compound. If we compare, for example, τ at $E - E_\text{F} = 0.1\,\text{eV}$ we get 280 fs for the $x = 0.06$, while we obtain 370 fs and 470 fs for $x = 0.14$ and $x = 0$, respectively. These differences

in τ for different dopings are clearly visible at $140\,\mu\mathrm{J/cm^2}$ and $240\,\mu\mathrm{J/cm^2}$ but they vanish at the highest F of $540\,\mu\mathrm{J/cm^2}$. Two effects are noteworthy: first, the relaxation times do not depend monotonically on x and the fastest relaxation is found at optimal doping. In the limit of Fermi liquid (FL) theory for a three dimensional metal, the scattering probability due to $e-e$ scattering is proportional to $n^{-5/6}$, with n being the number of carriers [141]. We remark that for this compound we assume a rigid-band model, as discussed in section 5.1, according to which the volumes of the FSs change according to the number of extra electrons x and the chemical potential is shifted accordingly. Therefore, at $T > T_N$, where the system is metallic, one would expect a monotonic dependence of the relaxation on x. Second, the difference in the energy-dependent relaxation times for different Co-substitution is only present until $E - E_\mathrm{F} = 250\,\mathrm{meV}$. At this energy a change in the curves of τ vs $E - E_\mathrm{F}$ appears as a discontinuity, which is more pronounced at the lowest F as marked by the arrow in figure 5.6(d) and absent at the maximal F. In figure 5.7 (a) and (b), time dependent intensities of the $x = 0.06$ compound for energy windows centered around 150 meV (orange) and 250 meV (light blue) are compared for $140\,\mathrm{mJ/cm^2}$ and $240\,\mu\mathrm{J/cm^2}$, respectively. It is obvious from the data that the difference in relaxation time between the two subsequent energy windows is more pronounced at the lowest F, while it is weaker at the intermediate F.
This effect manifests very clearly if we consider the relaxation rates as function of binding energy, obtained from $\Gamma = 1/\tau$ and shown on the lower panel of figure 5.7. At the lowest F (figure 5.7(c)) a step-like increase in the energy-dependent relaxation rates from $E - E_\mathrm{F} < 200\,\mathrm{meV}$ to the next values above this energy is observed for all x, at the same energy where the discontinuity in the correspondent relaxation times is found. The visibility of the step is fluence dependent, as it reduces with increasing F (figure 5.7 (d)) until it completely vanishes (figure 5.7 (f)).

5.2.2 Doping-dependence of the relaxation times

We will start here discussing the doping dependence of the relaxation times found in the first energy interval $0 < E - E_\mathrm{F} < 250\,\mathrm{meV}$ and the correspondent relaxation rates. We shift the discussion of the effect found at higher energies, i. e. the fluence-dependent step in the relaxation rates, to the next section.
As already mentioned in the discussion about the equilibrium electronic structure, the effect of Co-substitution is to add electrons to the system shifting the chemical potential upwards causing the electron pockets to enlarge and the hole pockets to reduce until they completely disappear below E_F for Co-concentrations higher than optimal. In this doping region ($0 < x < 0.15$), where two types of competing carriers are present, other properties than for a conventional metal are found. We have shown that the

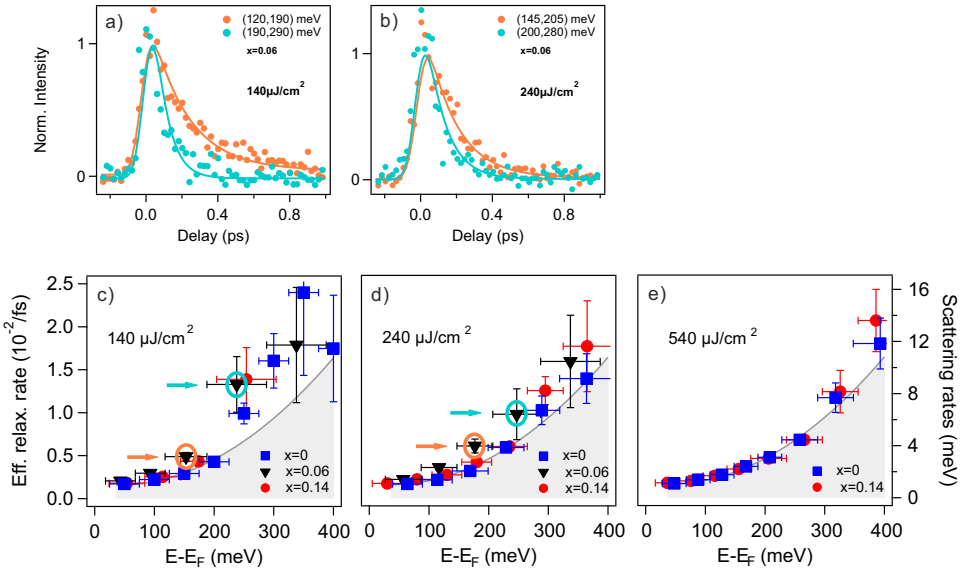

Figure 5.7: (a), (b) Normalized time-dependent intensity of the $x = 0.06$ (OP) compound for subsequent energy intervals around $\sim$ 200 meV for the fluences of (a) 140 μJ/cm^2 and (b) 240 μJ/cm^2. Solid lines are fit to the data.(c)-(e) Relaxation rates determined by taking the inverse of the measured relaxation times vs binding energy for different fluences. The blue and orange circles highlight the data point extracted from the data in (a) and (b). Values of scattering rates in meV are also reported on the right axis in (e). The contour of the grey-shaded area present in all the three graphs is a guide to the eye illustrating the high F behavior, and is shown in order to emphasize the different F-dependence for the scattering rates at $E > 200$ meV. [128]

doping dependence of the energy-dependent relaxation times do not scale monotonically with the carrier concentration (see figure5.6(e)), having the optimally doped compound the fastest decay.
It is not straightforward to unambiguously identify the relaxation channels responsible for this behavior, as for an excited population close to the Fermi level various interactions contribute to the relaxation in a complex manner. As we mentioned above, the dynamic redistribution of excited electrons has to be considered in addition to electron-boson scattering. We proceed by comparing our results with the ones obtained by other experimental techniques, starting from the static ARPES results introduced in section 5.1.1. These studies on the same class of compounds investigated in this work (as well as P-doped and $NaFe_{(1-x)}Co_xAs$) report values of the imaginary part of the self-energy Σ^{II}, or rather the scattering rates, for binding energy ranging from E_F down to 150 meV. This results, shown in figure 5.2, are independent of doping **[30, 31]** and increase linearly from 5 meV to 150 meV. The scattering probabilities obtained in the present work, in the time domain, from $\Gamma = \hbar/\tau$, shown on the right axis of figure 5.7, are of

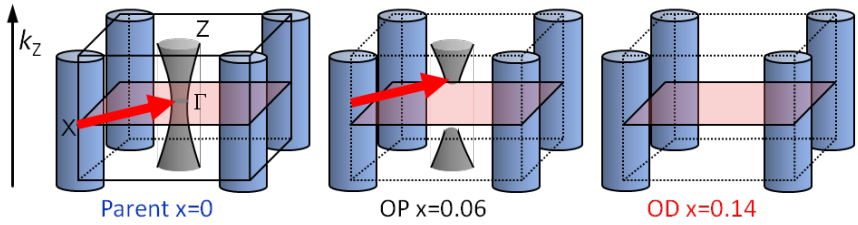

Figure 5.8: Schematic of the 3D character of the Fermi surface for the three different Co-substitution considered in this work. The high-symmetry points of the brillouin zone are indicated and the $k_Z = 0$ plane is shown in red. The hole pockets show a dispersion in the vertical momentum direction, while the effect is negligible in the case of the electron pockets. The red arrows are an indication of the momentum transfer due to possible interband scattering which, in the case of optimal doping, would not be present on the $k_z = 0$ plane, but in a region between Γ and Z. In the case of an overdoped compound, this scattering channel would be completely absent.

the order of 1 meV at energies $0 < E - E_F < 200$ meV. This difference, reaching about two orders of magnitude, between the values obtained from static ARPES in the energy domain and trARPES in the time-domain is in agreement with [140], where the same analysis was applied to a cuprate HTSC, comparing single particles lifetimes from equilibrium photoemission and energy-resolved population rates from trARPES. This is a confirmation of the fact that the lifetimes measured by static ARPES and the relaxation times obtained here close to E_F represent two different quantities. In the case of trARPES, relaxation of the laser-excited non-equilibrium electron population is analyzed, while in static ARPES the scattering probability of a single particle excitation is determined. As discussed in [140], Auger like processes within the valence band contribute negatively to the population decay by refilling of states and this need to be considered in explaining the large quantitative difference of the decay times obtained in ARPES and trARPES.
On the other hand, in the doping range under investigation, qualitative agreement is found with transport measurements, where the same trend with doping found in this work is observed in resistivity measurements, and the determined $e-e$ scattering times [25, 24] are larger near optimal doping than at over doping.

A widely shared interpretation [25, 90, 142, 92, 89, 91], sees antiferromagnetic fluctuations as being mainly responsible for these anomalies, because they occur near the QCP. The deviation of the T-dependent term of the resistivity from a quadratic to a linear scaling, accounting for the non-Fermi liquid behavior in the normal state, would qualitatively alter the T-dependence of the relaxation rate in the quantum critical regime, leading to the maximum scattering rate at optimal doping discussed above. Alter-

native explanation for the strange normal state properties of these systems near a QCP involves the influence of the Lifshitz transition, occurring at optimal doping [130, 129], and correlation effects on the scattering rates of the charge carriers **[31]**[136].
Given these considerations, the deviation from the behavior of a conventional metal which we observe in our trARPES study is not surprising, considering that the Fermi liquid theory does not hold. In discussing the relaxation process, the 3D character of the Fermi surface in these materials has to be taken into account. A schematic of the 3D Fermi surface for the case of the three considered Co-substitution is shown in fig. 5.8. As shown in section 5.1, the electronic structure is strongly doping dependent and, in particular, the k_z dispersion increases with increasing Co concentration [60]. That means that the observation of a Lifshitz transition, where the top of the hole pocket just touches the Fermi level is detectable only at $k_z = 0$, in the case of optimal doping. The Fermi surface at this point would consists of electron pockets at the zone corners and only a point at the zone center. However, due to our 6 eV pulse energy, we probe at a finite k_z value corresponding to a region between Γ and Z where we detect some remnant of the hole pocket in the case of the optimally doped compound (see figure 5.3 (b)). Hence, we point out that at the particular momentum where we probe, phase-space for interband $e-e$ scattering is available, which contributes to the relaxation in addition to intraband processes. This additional channel is instead absent in the case of the overdoped compound, because the hole pocket has completely sank below E_{F}, as we have shown in figure 5.3 (c). Hence, although we work at $T > T_N$, coupling between electron and hole pockets through interband scattering has to be considered as a possible additional contribution to the relaxation, which could play a role for the optimally doped but not for the overdoped compound, in agreement with our observation of a faster relaxation at optimal doping.
Clearly, the phase space argument for the relaxation discussed above applies also to the undoped compound, where coupling between electron and hole bands should be even stronger. However, we have shown that this system has the slowest relaxation, observable even in the case of the total integrated intensities (fig. 5.5). For the parent compound, due to the proximity in the phase diagram to the SDW transition, it is reasonable to assume that other processes contribute to the relaxation, competing with the one determining the relaxation in the Co-substituted compounds and resulting in an effective longer relaxation time. For instance, some region of the Fermi surface might be still partially gapped, due to the proximity of the AFM transition occurring at $T_{\mathrm{N}} = 140\,\mathrm{K}$. For the parent compounds, it has been shown that the relaxation times increase with lowering the temperature through the SDW state [54] and it is known that also other AFM fluctuations of different origin, including also nematic fluctuations, are present and persist above T_N [143, 99, 101, 144]. Therefore, at the temperature of 160 K, where

our measurements are performed, all these effect might play an important role, and effectively reduce the efficiency of the relaxation. This would not be the case for the $x = 0.06$ and $x = 0.14$ compounds, which do not undergo the SDW nor the nematic transition.

5.2.3 Signature of electron-boson coupling

Our second important observation manifests in the energy dependent relaxation rates, where a step is recognized at low F (Fig. 5.7 (c)) around $E - E_F = 200\,\text{meV}$ for all x. This is an indication that at these energies an additional relaxation channel contributes, causing the system to suddenly relax faster. Interestingly, this effect is fluence dependent, because the step is more pronounced at the lowest excitation and gradually reduces with increasing pump-fluence. Band structure calculations predict the presence of an unoccupied $4p$ As band at Γ to be 0.1 to 0.3 eV above the Fermi level [97, 145]. This could provide phase space for additional inelastic interband scattering due to a peak in the density of states around that energy. However, if this was the origin of the step visible in our data, we would expect the central energy at which the step occurs to change with doping, due to the shift of the chemical potential. In addition to that, no signature of such a feature is visible in our trARPES intensities spectra (analogous to Fig. 5.5 (a)) for any of the dopings and fluences.
A second possibility, is that an additional relaxation channel is provided by a bosonic excitation of a certain energy $\hbar\Omega$ that would couple to the excited electronic system. Theoretical modeling of the effects of electron-boson ($e-b$) coupling in trARPES [146] has shown to lead to a characteristic change in the decay rates, in the form of a step. A further confirmation of the presence of $e-b$ coupling, comes from the fluence dependence as we explain below with the help of Fig. 5.9. Electrons excited at $E-E_F > \hbar\Omega$ and the respective holes injected at $E-E_F < -\hbar\Omega$ would relax faster than those excited within the energy region $-\hbar\Omega < E - E_F < \hbar\Omega$, as shown originally in [148] in the case of a coupled electron-phonon system, and subsequently by Kemper et al. [147] for electron-boson coupling in general. According to this description, at equilibrium, scattering from inside the bosonic energy region to states below the Fermi level is suppressed, as the electron occupation does not provide the necessary phase space for the excited electrons to relax back to energies below E_F (Fig.5.9 left). Therefore the relaxation times inside the boson window are larger compared to those at energies outside, at $E - E_F > \hbar\Omega$. In the time-domain analysis the infrared pump redistributes the electronic population, which modifies the phase space. In particular, relaxation channels which were blocked in equilibrium become now available, leading to shorter relaxation times under non-equilibrium conditions (Fig.5.9 right). If we look at our data in Fig. 5.7(a) and (b) we notice that with increasing F, the relaxation becomes faster for the curve

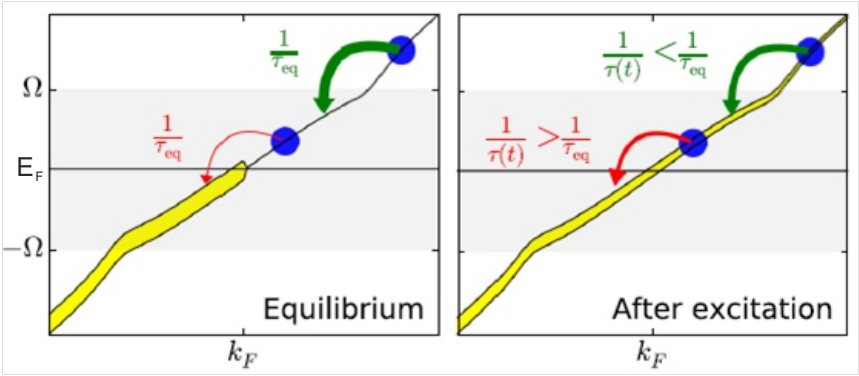

Figure 5.9: Illustration of the effects on the scattering rate caused by the infrared pump-induced spectral weight redistribution. The grey shades area indicates the boson window $(+\Omega, -\Omega)$; the thickness of the yellow lines indicates the electronic occupation of the band. In equilibrium and at low temperatures, scattering from inside the boson window is suppressed due to a lack of phase space for the final state given the high occupation below the Fermi level, with the opposite behavior for scattering outside the window. After excitation and spectral weight rearrangement, these phase space considerations are modified with an increase (decrease) of the scattering rate inside (outside). Taken from [147]

at lower energy (below $E - E_F = 200\,\text{meV}$) and slower for the curve at higher energy (above $E - E_F = 200\,\text{meV}$), in agreement with the behavior described above. At small F one expects a situation similar to equilibrium where the signatures of the boson window in the relaxation times and the electron population are only weakly perturbed [146, 147]. Indeed our data in Fig. 5.7(c) show that at the smallest excitation density the step is larger showing higher (lower) scattering probability above (below) a boson energy of $\hbar\Omega = 200\,\text{meV}$. With increasing F (Fig. 5.7 (d)) this step reduces as the pump-induced phase space redistribution provides more relaxation channels until the signature of the boson window completely disappears at the highest F (Fig. 5.7 (e)). Such an effect was also experimentally observed in the case of cuprates **[32]**, where the fluence-dependent step observed in the relaxation times originates from a single bosonic mode at an energy of 70 meV, corresponding to the well-known kink in the occupied part of the d-band. Contrary to the cuprates, our observation of the same effect occurring in FePn HTSC has no correspondence in the equilibrium occupied part of the electronic structure, suggesting the great potential of non-equilibrium studies, that can unveil new additional processes beyond the one observed in equilibrium.

To assign the origin of the bosonic excitation, we exclude phonons as a possible coupling candidate because the energy of 200 meV at which the effect is found exceeds the high energy cutoff of the phononic spectrum, which is located around 35 meV [149, 150]. A possible candidate is then a bo-

son of magnetic origin. Spin fluctuations in this high energy region were reported in literature for electron doped compounds [151, 152] and for the parent compound [143], where they are shown to persist also at $T > T_N$. Electron-magnon coupling was also observed in ARPES measurements on ferromagnetic Fe [153], showing a saturation of the increase of the imaginary part of the self-energy at 160 meV, consistent with the energy of spin waves in Fe.

5.3 Summary

We have performed a femtosecond trARPES study on Co-substituted $BaFe_2As_2$ at $T > T_N$ with different doping concentration. From the analysis of the energy dependent relaxation times we found a doping dependence that does not monotonously follows the carrier concentration. The optimally doped compound relaxes faster than the overdoped and the parent compound has the slowest relaxation, therefore our findings are in qualitative agreement with the doping-dependent results of transport measurements. We showed that at the finite k_z value at which we probe, interband coupling between electron and hole pockets has to be considered in the case of the optimal doped compound as a possible contribution in addition to intraband relaxation. We also discussed the quantitative difference of two orders of magnitude between the relaxation rates obtained here in the time domain and the ones analyzed in static ARPES from line width analysis, which is in agreement with what was found in the case of cuprate HTSC. Our results for Fe-122 confirm for a second class of HTSC materials that these quantities represent two different observables. In the case of trARPES, relaxation of the laser-excited non-equilibrium electron population is analyzed, while in static ARPES the scattering probability of a single particle excitation is determined. Although from our results we cannot quantify the intra- and interband conditions discussed above, it is remarkable that despite ARPES and trARPES are closely related regarding the technical concept, significant differences arise regarding the data interpretation and qualitative agreement is found instead with results obtained by transport, another dynamical method.
From the analysis on the energy dependent relaxation rates we could clearly identify the presence of a step around the energy $E - E_F = 200\,\text{meV}$,which is best observed for small laser pump fluences. We conclude that this indicates the coupling of the excited electronic system to a bosonic excitation, in agreement with theoretical descriptions [147], and suggest the magnetic origin of a such boson. This observation further supports the recently published work on cuprates **[32]**, for the other class of High-T_c superconductors and, contrary to the cuprates, the boson observed here has no counterpart in the equilibrium electronic structure, consistently with its magnetic nature. This last observation is suggestive of the great potential of the trARPES technique, that can act as a selective probe of electron-boson interactions as $e - b$ coupling leaves its mode-specific fingerprint on the population dynamics.

Chapter 6

TrARPES on 1*T*-TaS_2

Within the picture of strongly correlated materials, transition metal dichalcogenides provide rich opportunities to explore the emerging competition between various ground states. Due to their effective low spatial dimensionality they are more prone to electronic instabilities of the underlying coupled degrees of freedom like e.g. the electronic and lattice excitations, which can have macroscopic impacts on the material properties like phase transitions (see section 2.1.2). The low-temperature manifold of phases such as e.g. superconductivity, charge density wave (CDW), as well as electronically and magnetically ordered states present fascinating emergent properties that are of both fundamental and technological interest. A prototypical example of such ordered systems is the Mott-insulator, discussed in section 2.1.1 in which strong Coulomb forces between localized electrons can drive a nominal metallic system into an insulating ground state. In the particular case of systems in which charge order dominates the macroscopic material properties it is, however, challenging to find direct experimental access to measures that can characterize such states as well as the fundamental interaction processes that give rise to the formation of order. On one hand, analyzing the ultrafast dynamics of this system, driven out of equilibrium by an ultrashort light pulse, might shed new light on the underlying short- and long-range interactions, because different coupling channels can result in the relaxation on experimentally distinguishable (femto- to picosecond) time scales. Impressive agreement between theory and femtosecond time-resolved experiments was obtained by investigating the re-emergence of charge order, from a photoinduced quenched disorder, on the onedimensional organic Mott insulator ET-F_2TCNQ, a system that exhibits negligible electron-phonon interaction and, thus, can be well described by means of pure onedimensional electronic models [154, 155]. However, these dynamics might become more complex when the more general case is addressed, as in two- or three dimensional systems. There, simultaneously strong coupling between different degrees of freedom on comparable energy scales might compete or coexist. Thus a

unifying description of "real world" systems with many degrees of freedom remains challenging [42]. In this frame, $1T - TaS_2$, which displays a CDW transition coexisting with a Mott-Hubbard phase, is a widely and intensely studied model system. Femtosecond time-resolved experiments provided deep insight into this complex interplay between coexisting periodic lattice distortion and charge order, mainly by studying the photoinduced melting dynamics of the cCDW-Mott phase. Upon optical excitation, the system can be driven into a "cross-over" phase [19, 20, 22] that is characterized by an increased spectral weight at the Fermi level and a partial quench of the coherent state, accompanied by the excitation of the CDW amplitude mode [19, 20, 156, 8] and prompt collapse of charge order [8, 48]. Moreover, a recent time-resolved optical study reported on a photoinduced switching from the many-body insulating ground state to a long-living metallic metastable state [11], which can be reached only in non-equilibrium conditions and shows different characteristics than the ones present in any other equilibrium phase.

In the present chapter, we show a systematic temperature- and fluence-dependent trARPES study, discussing the details of the photo-excitation mechanism, aiming at characterizing the photoinduced phase. We then focus on the weak excitation regime and monitor the transient population of the upper Hubbard band (UHB), showing that doublon dynamics occur on a timescale of only a few hopping cycles, ruling out any interaction with the lattice. We therefore point out that this finding might be of help in the formulation of theoretical modeling, as, at least at early stages after photo-perturbation, only the electronic part of the system can be considered, while the phononic part is still in equilibrium. We will then compare our findings with a first theoretical description based on a time-resolved dynamical mean-field theory (tDMFT) approach that qualitatively reproduces our results fairly well when slight static hole doping is included.
Finally, we report on the switching to a photoinduced metastable hidden state starting from the low-T cCDW-Mott phase and characterize it by means of both static and time-resolved photoemission spectroscopy, thus having direct access to the electronic structure of the system. By comparing the characteristics of such a state with the one known from literature [11], we conclude that we have obtained partial switching and discuss it by means of a steady-state anisotropic heat conduction model [157, 11]. Part of the results reported in this chapter can be found in **[158]** and **[159]**.

6.1 Ultrafast response of the cCDW-Mott phase

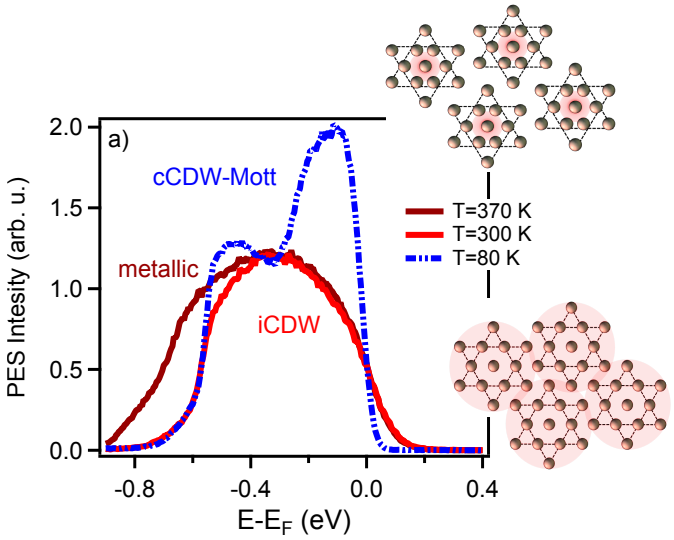

Figure 6.1: Comparison of static photoemission spectra in the metallic- iCDW- and cCDW-Mott-phase, at $T = 370\,\mathrm{K}$, $T = 300\,\mathrm{K}$ and $T = 80\,\mathrm{K}$, respectively. In the latter, the spectral weight at E_F is reduced, and transferred to the LHB, with a peak at $E - E_\mathrm{F} \approx -150\,\mathrm{meV}$. Finite spectral weight at E_F is nevertheless present. The sketch corresponding to the cCDW-Mott phase (top right) shows the contracted "David-star" with the localized charge (pink circle) located on the central 13th Ta atom. Both spectra at high T show prominently metallic character, with a Fermi-like high energy cutoff. The sketch corresponding to the iCDW/metallic phase (bottom right) shows the uncontracted hexagonal arrangement of Ta atoms and the freely moving electrons result in a delocalized charge, suggested by the overlapping big pink circles. Notably the spectrum in the purely metallic ($T = 370\,\mathrm{K}$) is about 150 meV broader. The intensity of the two spectra at high-T has been rescaled for better comparison with the low-T spectrum.

In figure 6.1 three equilibrium spectra in the metallic iCDW-, metallic nCDW- and the insulating cCDW-Mott phase are compared, corresponding to the temperatures of 370 K, 300 K and 80 K, respectively. At 300 K and 370 K the spectrum presents a high energy cutoff at the Fermi energy broadened by a Fermi-Dirac distribution function, signature of the predominant metallic character, while at 80 K, when the system is insulating, the spectral weight is transferred from E_F to the LHB peak situated at about $E - E_\mathrm{F} = -150\,\mathrm{meV}$. However, some finite spectral weight is still present because of our finite energy resolution and due to the non perfect atomical arrangement achieved in a real system, where in each of its phases a certain coexistence of contracted and uncontracted David-stars is present. The spectrum width is the same at $T = 300\,\mathrm{K}$ and $T = 80\,\mathrm{K}$, while at $T = 370\,\mathrm{K}$ it is about 150 meV broader, indicative of a decrease in the work function. Due to the absence of a Fermi cutoff in the low T spectra, we set our en-

ergy scale referring to the energetic position of the $T = 300\,\mathrm{K}$ Fermi cutoff, assuming that it is rigid. From now on, we will refer to the state at 370 K as to the "purely metallic"state, to differentiate from the metallic state at room T.

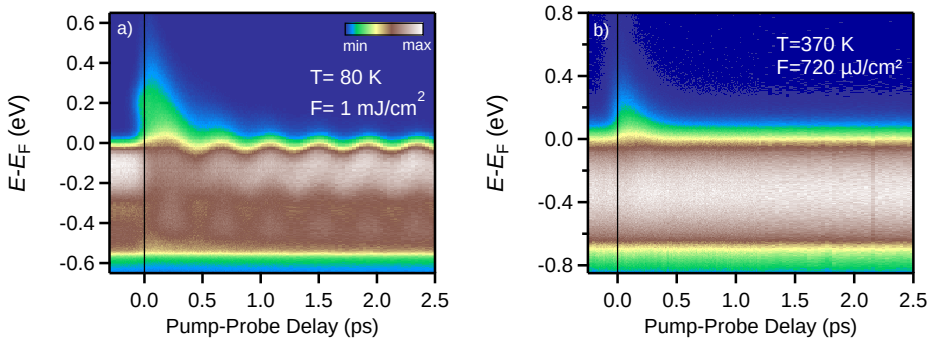

Figure 6.2: trARPES intensity of (a) the cCDW-Mott phase ($T = 80\,\mathrm{K}$) and (b) the metallic phase ($T = 370\,\mathrm{K}$) as function of binding energy and time-delay. In (a) upon photoexcitation one observes i) collapse and subsequent recovery of the LHB; ii) generation and subsequent relaxation of a hot carriers population continuum above E_F; iii) appearance of a coherent spectral feature at $E - E_\mathrm{F} \approx 175\,\mathrm{meV}$; iv) oscillations of the spectral weight due to the coherent excitation of the CDW amplitude mode. In (b) the signature of the coherent oscillations is absent, as the system does not present CDW. Only the generation of a hot carrier population above E_F and its subsequent relaxation is visible.

In figure 6.2 exemplary trARPES intensity spectra in the cCDW-Mott insulating state ($T = 80\,\mathrm{K}$) and purely metallic state ($T = 370\,\mathrm{K}$) are shown as function of binding energy and time delay, for high incident fluences of $1\,\mathrm{mJ/cm^2}$ and $0.7\,\mathrm{mJ/cm^2}$, respectively, where the pump-induced changes are more pronounced. The data in the cCDW-Mott phase (figure 6.2(a)) resemble previous studies under similar conditions [19, 20, 48, 8] and thus show the typical transient modifications which are usually observed. Upon photoexcitation, a sudden quench of the LHB intensity occurs simultaneously to the generation of a hot carrier population continuum up to $E - E_\mathrm{F} = -1.5\,\mathrm{eV}$ and the filling of the formerly gapped spectral region around E_F. The photoinduced, incoherent excitation continuum above E_F is accompanied by the appearance of a coherent spectroscopic signature at binding energies $150\,\mathrm{meV} < E - E_\mathrm{F} < 200\,\mathrm{meV}$. These features subsequently recover/relax, each with a characteristic time scale that we will describe in the following. In addition, a strong modulation of the photoemission intensity signal is present up to tens of ps, originating from the pump-induced coherent excitation of the CDW amplitude mode, which reflects the breathing mode of the star-shaped clusters together with the charge density. The data in the purely metallic state (figure 6.2(b)) show the generation of a hot-electron

population occurring upon pump-excitation, which subsequently relax. The coherent spectroscopic signature, visible in the low-T regime, is completely absent here. Finally, the signature of the coherent oscillations is also not present, in agreement with the absence of the CDW in the system. In the literature, a quickly damped oscillation is reported at $T = 300\,\mathrm{K}$, ascribed to the lack of CDW commensurability in this metallic phase [20].
We will now proceed by analyzing and discussing each single feature separately, focusing in particular on the cCDW-Mott phase. Excitation fluences are given here as incident fluences F and were kept below the critical energy density necessary to drive the system thermally into the nearly-commensurate CDW phase [160].

6.1.1 Collapse of charge order and localized excitation

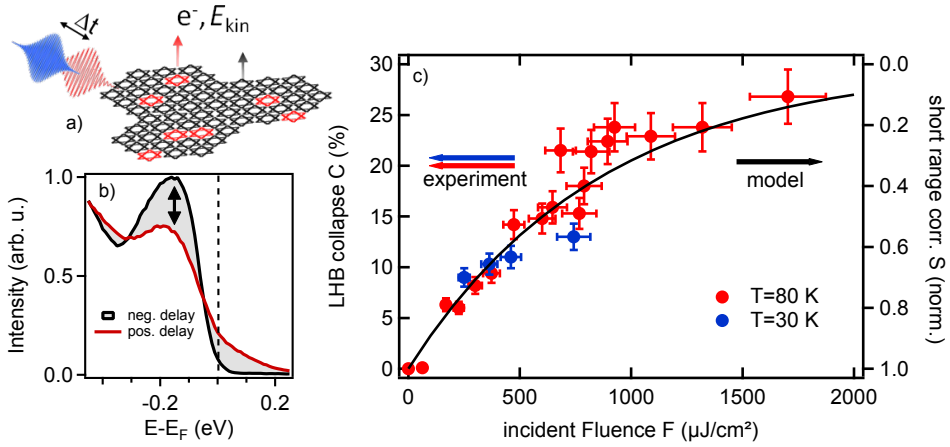

Figure 6.3: (a) Sketch of the femtosecond photoemission experiment in the cCDW-Mott ordered state. The sample is excited by a femtosecond IR pulse to partly turn single polaron sites (black stars) to be metallic (red stars), according to a localized excitation scheme (see text). Subsequent photoemission by a fs UV pulse probes the transient coexisting phases. (b) Photoemission spectra taken at negative and positive delay for an excitation fluence $F > 1\,\mathrm{mJ/cm^2}$. The shaded area and the double sided arrow indicate the photoinduced change and the quench of the LHB maximum upon optical pumping, respectively. (c) Collapse of the LHB signature as a function of incident pump fluence. The solid black line shows the result of the model calculation and the expected quench of short-range correlation S.

Typical photoemission spectra before and after excitation are shown for the low-T Mott phase ($T = 80\,\mathrm{K}$) in figure 6.3(b). Upon optical excitation, a sudden quench of the LHB signature is observed, accompanied by the generation of hot electrons up to $E - E_\mathrm{F} \approx 1.5\,\mathrm{eV}$ and a filling of the formerly gapped spectral region ($E - E_\mathrm{F} \approx -0.2, +0.2\,\mathrm{eV}$), indicating that the Mott phase is partially molten and that the corresponding short range correla-

tions are quenched. We determine the pump-induced maximum collapse C of the LHB spectral signature for different incident pump fluences from the relative difference between the maxima of the LHB peak in the unpumped spectrum at negative delay and pumped spectrum at early positive delay ($\sim 50\,\mathrm{fs}$). The results are shown in percentage in figure 6.3(c) for $T = 30\,\mathrm{K}$ and $T = 80\,\mathrm{K}$, as a function of incident pump fluence. For small excitation fluences $F < 500\,\mu\mathrm{J/cm^2}$, an almost linear dependence is found, indicating a perturbative excitation regime. In this limit, to which we refer to as *weak excitation limit*, the LHB intensity directly corresponds to the amount of excited quasi-particles. The observed quench of the LHB saturates at $F > 1000\,\mu\mathrm{J/cm^2}$ (*strong excitation limit*) and a maximum depletion of 25 percent of the total maximum intensity is found. It should be noted that a discussion of the absolute photoemission intensities is not rigorously possible, as the metallic phase also exhibits a finite spectral weight in the same spectral region (see figure 6.1). Thus, a collapse of the LHB signature by 100 percent (e.g. a transition to the metallic phase) might actually result in a smaller loss in photoemission intensity, e.g. the 25 per cent observed here. We interpret the saturation of this photoemission intensity loss as the (almost) complete loss of these short range interaction responsible for the emergence of the Mott gap and the LHB signature. We therefore refer to the LHB spectral signature intensity as a direct measure of the strength of the correlation in the system, as if it would be an "order parameter" for the charge ordered state.
We assume a localized excitation scheme, in which the IR pulse excites the sample turning part of the single David- star-polaron sites to be metallic, as schematically shown in figure 6.3(a). Under the assumption of a linear response, where every incident photon can excite a single cluster site (and thus quench its corresponding interactions) once, the scaling of the LHB intensity collapse C is given by the ratio between the density of excited clusters n_x with respect to the total cluster density n. Under this assumption, the fluence dependent collapse in figure 6.3(c) can be described by a simple differential equation of the form:

$$\frac{dn_x}{dF} = \frac{(1-R)(1-e^{-c/2\lambda})}{\hbar\omega}\left(\frac{n-n_x}{n}\right) \tag{6.1}$$

that we use to fit our results in figure 6.3(c), where the geometrical cluster density $n = 7 \cdot 10^{13}\,\mathrm{cm^{-2}}$ [161], $\hbar\omega$ is the pump photon energy, $c/2 = 0.298\,\mathrm{nm}$ is a single layer thickness [161] and R, λ are the optical reflectivity and penetration depth, respectively [162]. The solution of Equation 6.1 is shown as a solid line in figure 6.3(c). The curve was rescaled to account for incoherent background and the metallic phase spectral weight by matching its asymptotic value at high F to the asymptotic value of our experimentally determined maximum C. In this way, the so-

lution of Equation 6.1 directly reflects the short range correlation strength $S \propto (1 - C)$. The best fit to the data is obtained for an absorption probability of $\gamma = (1 - R)(1 - e^{-c/2\lambda}) = 2.2 \cdot 10^{-3}$, which is only a factor of 4.6 higher than the literature value of $\gamma = 0.48 \cdot 10^{-3}$ [162]. This difference can easily originate from differences in the optical parameters or systematic errors in determining F. A reduction of short range correlation strength up to 90 percent is observed for high excitation fluences, reflecting an almost complete quench of the coherent state. Thus, one might expect that under these conditions the system is driven non-thermally into its conductive phase.

This first analysis suggests that it is reasonable to consider a localized description, it is helpful to identify the perturbative regime of excitation and indicates that at high pumping fluences an almost complete loss of order is reached. Such facts should be reflected also in the dynamics of the system, thus more insight can be gained by monitoring the time evolution of the non-equilibrium electronic structure. Therefore, in the next step we proceed by analyzing and comparing the relaxation of the hot-electron population at different T, for both the Mott-cCDW and metallic states.

6.1.2 Hot electrons relaxation and recovery of charge order

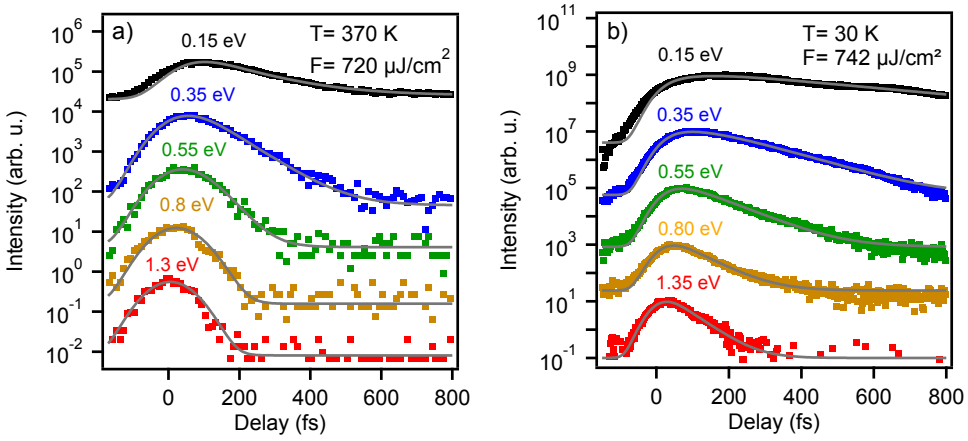

Figure 6.4: Electron population dynamics in selected energy windows above the Fermi level for the purely metallic state at $T = 370\,\mathrm{K}$(a) and the cCDW-Mott phase at $T = 30\,\mathrm{K}$. The intensity is shown on a logarithmic axis and the curves are offset for clarity. The grey solid lines are the corresponding fit to the data.

In order to further verify the localized excitation scheme concluded above and determine the primary energy loss mechanisms that drives the system back into its coherently ordered ground state, we investigate and compare the dynamics of hot photoexcited electrons in both, the purely metallic and

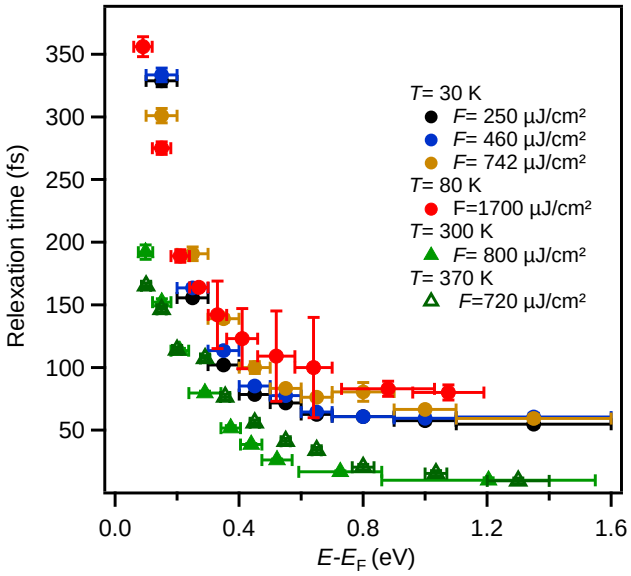

Figure 6.5: Resulting hot electron decay times as a function of excitation fluence and sample temperature. The results for $T = 300\,\mathrm{K}$ are obtained from the data by [19, 20]. Error bars on the energy axis indicate the integrated spectral regions used to obtain the population dynamics.

insulating phase. Analogously to the study illustrated for the iron pnictides, we proceeded by analyzing the population dynamics in selected energy windows above E_F. In figure 6.4 exemplary energy-integrated photoemission intensity curves as function of time delay, for the cCDW-Mott phase at $T = 30\,\mathrm{K}$ (6.4(a)) and in the purely metallic phase at $T = 370\,\mathrm{K}$ (6.4(b)) are shown on a logarithmic scale. By comparing the raw data in the figures, it is clear that the relaxation is faster in the metallic phase in all energy regions and at $T = 30\,\mathrm{K}$, within the highest energy interval, the excited carriers still show significant lifetimes of the order of some tens of fs. This is not surprising, considering that despite the Mott gap collapses, the CDW gap is still present [160] reducing the phase space for relaxation with respect to the metallic gapless system.

We fitted the time-dependent photoemission intensities with a single exponential decay function, convoluted with the pump-probe envelope, to obtain the correspondent relaxation times, as it was done for the iron pnictides energy-dependent data (see section 5.2.1). Exemplary fits are shown in figure 6.4(a) and (b) and the obtained energy-dependent relaxation times are shown in figure 6.5, comparing different fluences in the low-T and the high-T phases. For completeness, the results for the $T = 300\,\mathrm{K}$, obtained by the data from ref. [19, 20] are reported, which match quite good our results at $T = 370\,\mathrm{K}$. In the low T phase we find very similar relaxation times for all in-

vestigated F and even in the strong excitation regime at $F = 1700\,\mu\mathrm{J/cm^2}$, where an almost complete quench of the correlation strength was determined, the timescale for relaxation are the same as for the lowest fluence of $250\,\mu\mathrm{J/cm^2}$. In addition, the relaxation is more than two times slower than the one deduced from the metallic phase, in all energy ranges. In particular, at $E-E_\mathrm{F} > 0.6\,\mathrm{eV}$, where $e-e$ relaxation processes should be dominant (see section 2.2.2), the lifetimes are significantly longer, if compared to the ones determined for the metallic phase. Here, at $E - E_\mathrm{F} = 0.6\,\mathrm{eV}$ the lifetimes amount to 35 fs and tend to further decrease at higher energies, while in the insulating state, in the same energy region, the timescales for relaxation are about 75 fs, more than double, even at the highest excitation fluence.
The absence of fluence dependence for the low-T data and the significant difference in relaxation times obtained in the metallic and insulating phases suggest an efficient suppression of the $e-e$ scattering channels in the cCDW-Mott phase of the system, because otherwise $e-e$ interaction between photoexcited carriers would result in rapid carrier thermalization and a pronounced excitation fluence-dependence of the observed dynamics. This is in agreement with the picture of a localized excitation of carriers, that do not scatter among each other. We conclude that optically excited carriers are localized on a length scale of less than one cluster site and refer to these states as excited cluster orbitals. Furthermore, the transient photoinduced state is significantly different from the high-T metallic phases, even when the short range correlations are almost lifted. The localized nature of the excitation process suggests a real space description of the photoinduced state in which single polaron sites are excited and coexist with unperturbed sites in an unordered manner (figure 6.3(a)). This situation is different from the well-known equilibrium structures that still exhibit nearly- to incommensurate order in the different high temperature phases [18].

To further quantify the relaxation dynamics and the recovery of charge order, we compare the relaxation of the total population excited above E_F with the recovery dynamics of the LHB. We therefore integrate the total photoemission intensity (E_tot) from E_F up to 1.5 eV and compare it with the photoemission intensity integrated around the LHB energetic position as function of delay, as shown in figure 6.6(a) and (b), respectively for the excitation fluence of $1\,\mathrm{mJ/cm^2}$. By fitting the data with a single exponential decay function, convoluted with the pump-probe envelope, we obtain a relaxation time of 325 fs for E_tot, which is almost three times smaller than the recovery time of 800 fs obtained for the LHB. The relaxation of E_tot matches the values of the lifetimes determined close to E_F (below $E-E_\mathrm{F} \sim 0.1\,\mathrm{eV}$) in the energy dependent analysis discussed above (figure 6.5), indicating that the processes occurring in that energy region are the ones dominating the relaxation of the excess energy in the electronic system. As explained in section 2.2.2, close to the Fermi level, dissipation of energy through electron-phonon coupling becomes important, but it is intertwinned in a non trivial manner

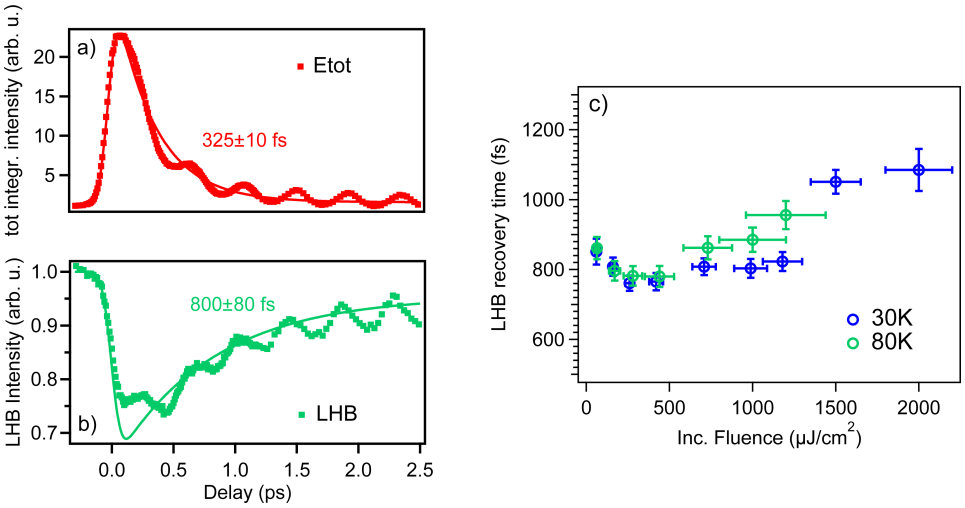

Figure 6.6: Temporal evolution of the total photoemission intensity above the Fermi level E_{tot} (a) and the LHB intensity (b) for $F \approx 1\,\mathrm{mJ/cm^2}$ and $T = 80\,\mathrm{K}$. Solid lines are fit to the data. (c) recovery time of the LHB as a function of fluence for $T = 30\,\mathrm{K}$ and $T = 80\,\mathrm{K}$ obtained with a single exponential fit.

with the effect of secondary excitations. However, very similar timescales were obtained in time resolved electron diffraction experiments [163] on the nearly-commensurate CDW phase of $1T - TaS_2$, which directly probe the lattice dynamics. Such study showed that lattice heating after femtosecond optical excitation due to the energy transfer from the electronic system to phonons occurs on a timescale of 350 fs, proving also in our case, electronic energy relaxation due to electron-phonon interaction. While after $\sim 350\,\mathrm{fs}$ a major amount of the excess energy has been transferred to the lattice system, the electronic system is still in a non-equilibrium state as the LHB intensity did not fully recover. The strong mismatch in the timescales for E_{tot} and the recovery of the LHB shows that while electron-phonon interaction is the major energy loss channel for the electronic systems excess energy, it cannot be solely responsible for the complete relaxation of the system back into its charge ordered ground state.

Since in 1T-TaS$_2$ the emergence of charge order is directly linked to the periodic lattice distortion associated with charge density wave order, it would be reasonable to assume that the recovery of charge order after a sudden quench is also strongly influenced by the lattice. To discuss this point, Figure 6.6 (c) is helpful, which shows the recovery time of the LHB as a function of fluence, for $T = 30\,\mathrm{K}$ and $T = 80\,\mathrm{K}$. At both temperatures, the same qualitative trend is recognized: a slight decrease from 860 fs to 780 fs is found in the low excitation regime, for F up to $500\,\mu\mathrm{J/cm^2}$. After that an increase of the recovery time up to 1.1 ps occurs in the strong

excitation regime. Although an overall variation of about 30% of the recovery times with the excitation fluence is found, no clear monotonous trend can be identified. This excludes a thermal activated recombination process, as higher lattice temperatures would facilitate the formation of a favorable nuclear configuration for polaron-reformation and, therefore, should result in a fast re-establishment of charge order. Thus, in this case, we would expect a reduction of the recovery time with increasing F. Although in the weak excitation regime, the recovery times slightly decrease, there is clearly no difference between the temperatures of 30 K and 80 K, corresponding to almost a tripling of thermal energy. Therefore, we conclude that while electron-phonon interaction is serving as an energy loss mechanism, more complex processes of electronic nature must play an important role for the complete re-establishment of charge ordered ground state of the system.

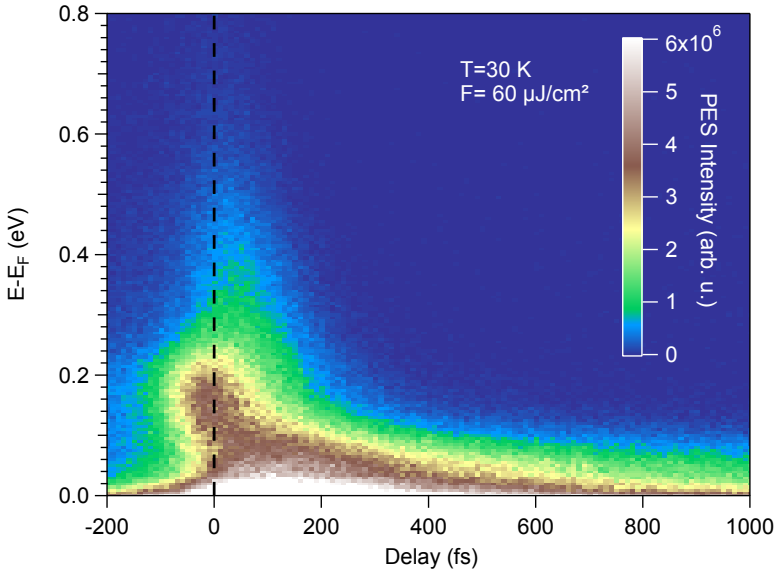

Figure 6.7: False-color representation of the unoccupied part of transient photoemission spectra recorded at low temperature ($T = 30\,\mathrm{K}$) in the weak excitation limit ($F = 60\,\mu\mathrm{J/cm^2}$). Beside an incoherent excitation continuum, the appearance of the spectral signature at $E - E_\mathrm{F} \approx 175\,\mathrm{meV}$ is observed at early delay times. From [**158**]

6.2 Ultrafast population of the UHB

After having discussed the collapse and recovery of charge order and the relaxation of the incoherent population excited above E_F, we will now turn our attention to the coherent spectral signature appearing at $E - E_\mathrm{F} \sim 200\,\mathrm{meV}$ upon photoexcitation of the material in the cCDW-Mott phase. We will focus our discussion on the data obtained in the weak excitation limit (see section 6.1.1), a situation that should virtually reflect the equilibrium properties of the material. Assuming that every incident photon can excite one valence carrier on an individual star site once, according to equation 6.1 and assuming the absorption probability which gives the best fit to the data, the excited carrier density in the first atomic layers was estimated to be less than 3 per cent for $F = 100\,\mu\mathrm{J/cm^2}$.

Under such excitation conditions we observe the appearance of a photoemission peak at $E - E_\mathrm{F} \approx 175\,\mathrm{meV}$, as shown in figure 6.7 in a false color representation. The spectrally incoherent excitation continuum that ranges up to $E - E_\mathrm{F} \approx 1.5\,\mathrm{eV}$ exhibits population maxima that appear at energy-dependent positive delays of a few femtoseconds due to the finite life times of the corresponding electronic states [164, 165, 166]. In contrast, the sharp spectral signature at $E - E_\mathrm{F} \approx 175\,\mathrm{meV}$ responds significantly faster and exhibits a population maximum at zero delay, indicative of a life time of only few fs, not resolvable with our experimental setup. The dis-

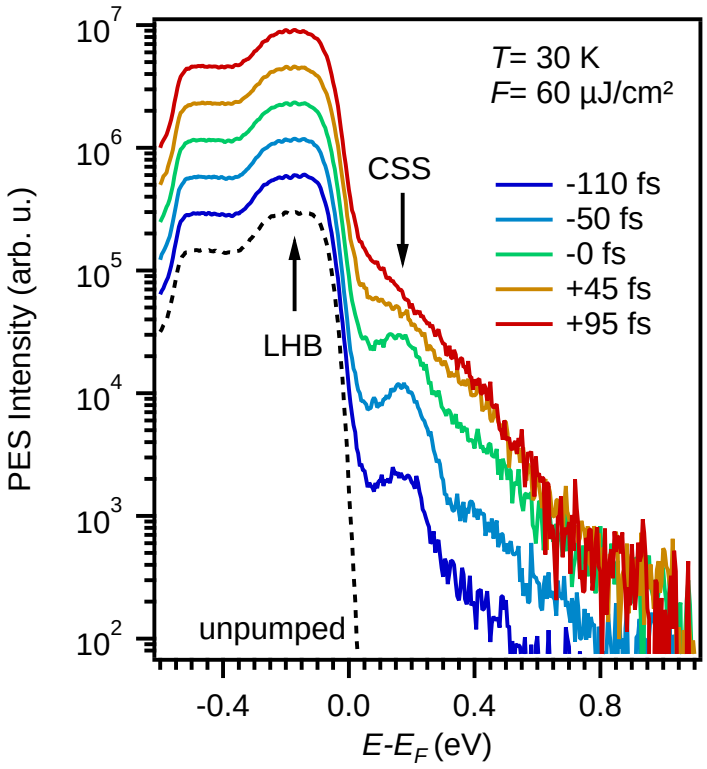

Figure 6.8: Transient photoemission spectra obtained for $T = 30\,\mathrm{K}$ and $F = 60\,\mu\mathrm{J/cm^2}$. The curves are offset for better visibility. From [**158**]

tinct response of such a spectral feature becomes evident when the transient energy distribution curves (EDC) are considered. Figure 6.8 shows EDCs at selected time delays between $\pm 100\,\mathrm{fs}$ and the unpumped spectrum. The spectroscopic contrast, of the order of $< 1\%$ with respect to the LHB intensity, reaches its maximum around zero delay and, along with ultrafast melting of the formerly gapped spectral region around $E - E_\mathrm{F} \approx \pm 0.2\,\mathrm{eV}$, is completely lost after $\approx 100\,\mathrm{fs}$. At later delays in the same energetic region, only the spectrally incoherent signatures analyzed in the previous section remain, arising from the excitation of secondary electrons upon scattering and energetic relaxation of the primary excited electrons.

Fig 6.9 (a) shows EDCs at $T = 30\,\mathrm{K}$ for different excitation fluences, evidencing that the spectral signature is indeed more prominent in the low excitation regime and Fig 6.9 (b) compares EDCs for different temperatures. The peak is present in the low-T cCDW-Mott phase ($T = 30\,\mathrm{K}$,$80\,\mathrm{K}$) and completely absent in the purely metallic phase ($T = 370\,\mathrm{K}$). At $T = 300\,\mathrm{K}$, an onset is visible. In both graphs the spectra were averaged over the delay range $\Delta t = (-125, -65)\,\mathrm{fs}$, in which the spectral signature is most promi-

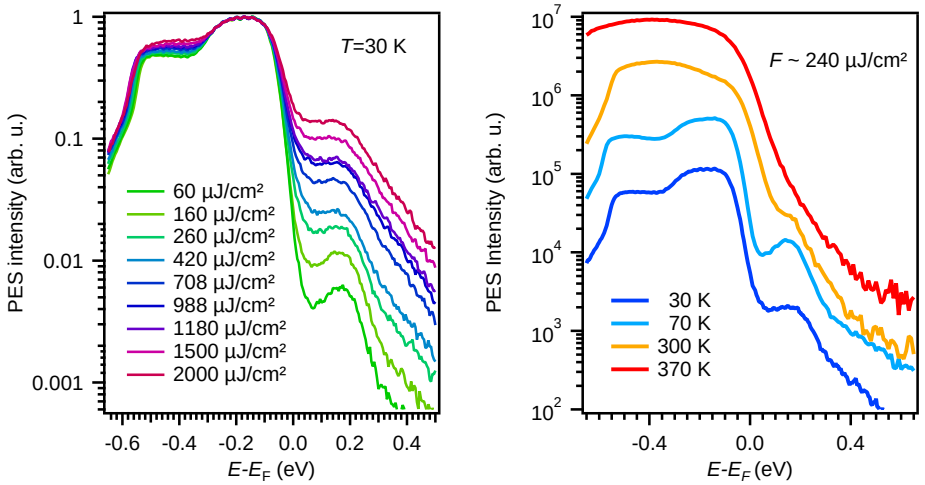

Figure 6.9: transient photoemission spectra as a function of (a) excitation fluence and (b) sample temperature, respectively. The spectra were averaged over the delay range $\Delta t = (-125, -65)$ fs, in which the photoemission peak is most prominent. Curves in (a) are offset for better visibility. From **[158]**

nent. Here we anticipate that the fact that the contrast is maximum at slightly negative delays depends on the positioning of our $\Delta t = 0$ delay in correspondence of the maximum photoemission intensity of the highest energy carriers, which in this case occurs few femtosecond later with respect to the signature under discussion here. We will come back to this point in the next section in more detail. Due to the energetic position of the spectral signature, its absence in the purely metallic phase, time-independent binding energy and ultrafast dynamics discussed throughout the present section, we identify this state as the upper Hubbard band (UHB), in agreement with recent scanning tunneling microscope experiments [167] and inverse photoemission studies [168] that suggest a symmetric gap around E_F and identify the corresponding state to be a backfolded part of the Ta 5d manifold. The signature visible at $T = 300$ K can be justified as the system already entered the nCDW phase and, although it has not developed the Mott-phase yet, intracluster Coulomb repulsion among electrons has started increasing (see section 3) simultaneously with the local formation of cluster sites. Thus, this might well result in a very weak signature, being an onset of the UHB formation.

We remark that this is the first trARPES experiment leading to the distinct observation of this state, which in a Mott system reflects the double occupation of a single lattice site (doublon state, see section 2.1.1). Although previous experiments [20] addressed the presence of a broad feature appearing above the Fermi level in the photoexcited state, the contrast was not

sufficient to enable its analysis both in the energy- and time-domain and such feature was ascribed to a midgap signature.

6.2.1 Temporal evolution of the UHB

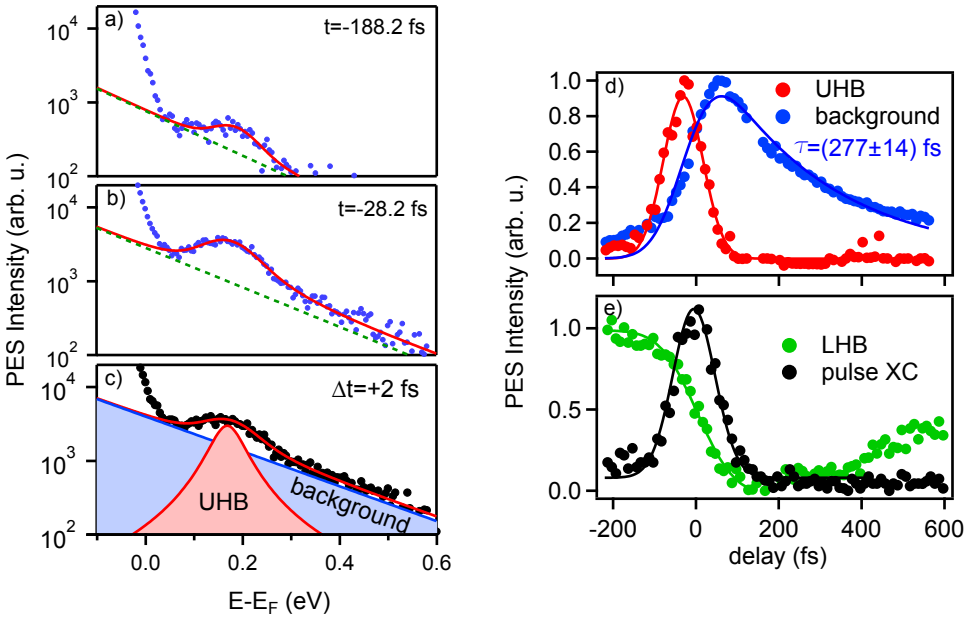

Figure 6.10: (a)-(c) Exemplary fits to the transient EDCs obtained at time delays Δt of -188 fs, -28 fs, $+2$ fs (where both components are highlighted. The superposition of the incoherent exponential background and the Lorentzian line was convoluted with the instrumental energy resolution function. (d) Temporal evolution of the UHB spectral signature in direct comparison to the underlying incoherent background. The solid line are fits to the data. The data in (d) are compared with (e) time-dependent photoemission intensity reproducing the pump and probe XC and the LHB intensity collapse. From [**158**]

In order to further discuss the temporal evolution of the UHB and separate its dynamics from the underlying incoherent background, we decomposed both spectral contributions by fitting the energy distribution curves with an exponential background and a Lorentzian line convoluted with the instrumental resolution function, as exemplary shown in fig. 6.10 (a)-(c) for some selected delays. From this analysis we obtained the peak intensity of the UHB and the underlying background intensity as a function of time-delay, shown in figure 6.10 (d). The background intensity reaches its maximum few tens of fs later that the UHB as the building up of the incoherent hot electron populations close to E_F is influenced by states lifetimes and secondary excitations, as discussed in chapter 5 for the FePn. In contrast, the population of the UHB is formed instantaneously. Such curves were then described with a single exponential decay fit function, convoluted

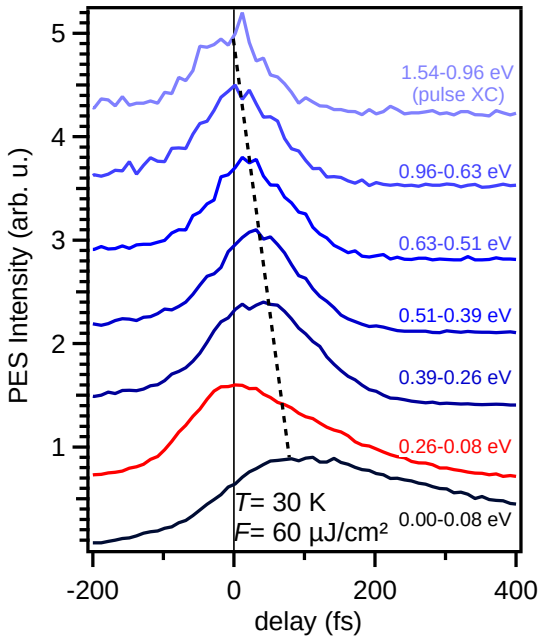

Figure 6.11: Time-dependent photoemission intensities integrated in different energy windows, where the red trace is the resulting curve for the energy region of the UHB and the trace obtained from the highest energy region represents our Pump-probe cross correlation and is used as reference to set the zero on the delay axis. While the maxima of the time-dependent intensities close to the Fermi level are shifted to positive delay, the maximum of the UHB curve is at zero delay.

with a gaussian function representing our pump-probe envelope, in order to obtain their time-dependent relaxation. While the ultrafast response of the UHB shows no significant lifetimes, the underlying background and the spectral gap exhibit slower dynamics with a significant population decay time of 280 fs, in agreement with the previously shown results (figure 6.5 and 6.6a). The fact that the background intensity is still present at positive delay times, while the UHB intensity is already quenched, suggests that the corresponding doublon states can not be populated by secondary excitations and we conclude that their photoinduced dynamics can not be described by incoherent scattering processes considering rigid bands. Within our experimental resolution, the UHB intensity reproduces the laser pulse cross correlation that was obtained from the highest energy carriers. These carriers have in general negligible life time and, thus, their population dynamics mainly resembles the temporal response function of the experiment (Figure 6.10 (e)).

However, we have to remark that in the case of 1T-TaS$_2$ samples, states with finite lifetimes are present even in the highest energy region (close to

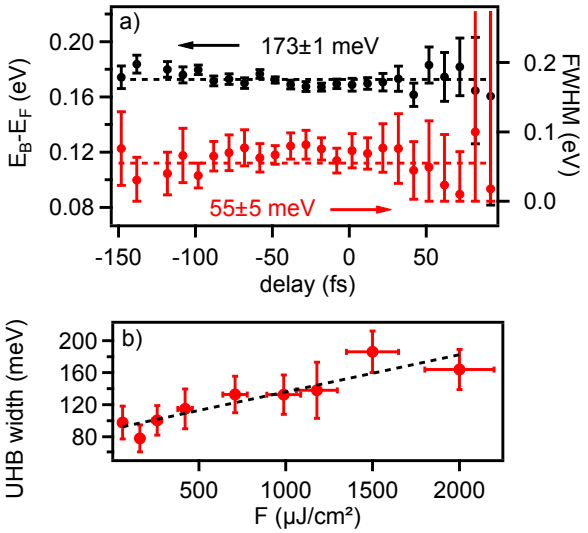

Figure 6.12: (a) Binding energy E_B and photoemission line width (Lorentzian full width at half maximum) of the UHB as a function of delay time. (b) Spectral width of the UHB signature as a function of excitation fluence. From **[158]**

$E - E_F = 1.5\,\text{eV}$). Since such lifetimes are much shorter than the pulse duration, which in this case amounted to $\sim 110\,\text{fs}$, the cross-correlation (XC) curve looks symmetric, but the maximum is shifted to slightly positive delay. This produces a systematic error in the positioning of the zero on our delay axis, which is usually determined from the maximum position of the XC curve . Although we can not exactly quantify the amount of the shift, we can estimate that it should not exceed $\sim$ 20 to 30 fs. Such limit correspond to the minimum observable decays which produce a deviation from the symmetric appearance of the XC curve. In the analysis reported in fig. 6.10(a)-(c) and (d) we could separate the coherent Lorentzian contribution from the incoherent exponential background, responsible for the shift to positive delay, this is the reason why the maximum of the UHB is located at around $\Delta t \approx -30\,\text{fs}$. If we instead compare time-dependent photoemission intensities integrated in different energy windows, as shown in figure 6.11, we observe a shift of the maximum intensity towards positive delays for all curves, which gradually increases approaching the Fermi level, except for the one corresponding to the energy interval which includes the UHB. The maximum of this trace coincides with the maximum of the curve representing our cross correlation, which is a further confirmation that the shift to negative delay observed in the results plot in figure 6.10 (d), comes indeed from the separation of the coherent and incoherent components performed in the previous analysis.

The fast response of the UHB in close vicinity of the Fermi level is signif-

icantly different from what was observed in, e.g. metallic or semiconducting systems, where population decay times of a few hundred of fs can be expected [166, 169]. Figure 6.12 (a) shows the results of the Lorentzian fits in the case of $F = 160\,\mu\mathrm{J/cm^2}$, as a function of delay. The UHB peak position is around $E - E_\mathrm{F} = 173 \pm 1\,\mathrm{meV}$ and is a constant function of delay, as well as the spectroscopic linewidth which results on average $\sim 55 \pm 5\,\mathrm{meV}$. At last figure 6.12 (b) compares the linewidth obtained by fitting the spectra in figure 6.9 (a) for different incident pump fluences, showing an approximately linear increase with increasing excitation. This excludes the photoemission line to arise from an unoccupied rigid band populated by the 6 eV probe pulse. The discrepancy between the values of $55 \pm 5\,\mathrm{meV}$ and $78 \pm 8\,\mathrm{meV}$ for the Lorentzian linewidth obtained for the same F originates from the fact that the data in 6.12 (b) are obtained not from single spectra at a given delay but from spectra integrated over a delay range ($\Delta t = (-125, -65)\,\mathrm{fs}$. The minimum spectroscopic line width of 55 meV would support a minimum life time of $> 8\,\mathrm{fs}$. Moreover, the temporal evolution of the UHB coincides the collapse of the LHB signature that was previously shown to occur quasi-instantaneously, on a time scale of less than 20 fs [48] and since we are able to detect lifetimes of at least $\sim 30\,\mathrm{fs}$, we can consider this to be an upper limit for the life time of the UHB. Thus, the characteristic time scale for the UHB dynamics would roughly correspond to one or few hopping cycle that is expected to occur on a time scale as short as $\hbar/J \approx 14\,\mathrm{fs}$ [20, 170].
Neither the line width nor shape of the UHB change as a function of delay, indicating that the population within the UHB rapidly thermalizes within the experimental resolution. This fingerprint of strong $e - e$ interaction, which leads to fast energetic redistribution of carriers within the electronic subsystem, underlines the fundamental distinct response of the UHB with respect to the incoherent electron population analyzed in the previous section, which showed instead inefficient scattering among the excited carriers. We furthermore observe that the binding energy of the signature does not change with time (figure 6.12 (a)). This excludes the possibility that the signature discussed here arises from polaronic excitations identified earlier by femtosecond optical spectroscopy [22] and verifies the ultrafast decoupling of electronic and lattice degrees of freedom, since polaron formation or disintegration would result in an energetic stabilization on resolvable (phononic) time scales. Indeed, the response of the UHB appears to be faster than a quarter-period of the highest-frequency phonons in 1T-TaS_2 (11.9 THz) [171].

Based on these results we can conclude that the electronic and phononic subsystems are decoupled on early stages after photo-perturbation, which leads to a significant reduction of complexity in the theoretical modeling, as only the electronic part of the system can be considered. While electron-phonon coupling plays a major role serving as, e.g. an energetic loss channel

for the electrons on longer time scales, the dynamics on ultrafast timescales, thermalization of carriers in the UHB and subsequent decay of its occupation do not require such coupling.
It should be stressed that our experimental findings are partly incompatible with the recently established explanation of energy gap formation based solely on orbital texturing effects [113]. Optical excitation of an orbitally ordered system would result in a rapid destruction of the orbital order. Correspondingly, the electronic gap should melt on electronic time scales, as observed previously experimentally [19, 20, 48, 8]. Assuming that our signature arises from the orbitally ordered state, it would indeed be imaginable that optical excitation can result in a temporary population of this signature before it is disintegrated due to the exceedance of a certain excitation level. However, the subsequent cooling process of the electronic subsystem should results in a regeneration of this signature and the state should be repopulated by secondary excitations. Such a behavior is not observed in our experiments. Furthermore, slight shifts of the binding energy or linewidth changes should be observable during the disintegration of the unoccupied state, which are also absent in our experiments. We thus believe that, while orbital order might play a role in electronic band formation, the electronic response occurs in a limit where correlation effects can not be neglected and the integral response of the electronic system to the optical perturbation must be considered.

6.2.2 DMFT calculations

A theoretical description of the phenomenon addressed here in our experiment was provided by our collaborators M. Eckstein at the Max Planck research department of Structural Dynamics in Hamburg and P. Werner and D. Goleš at the University of Fribourg (Switzerland). In the following, we will report the results of such study, that discusses a simple theoretical picture based on a purely electronic model and demonstrate how the inclusion of strong interaction effects is crucial for a description of the short time dynamics.
In the previous section, we concluded that it appears to be safe to neglect coupling to vibrational degrees of freedom on the time scales under discussion. Therefore, the dynamics of a single band Hubbard model on a two-dimensional triangular lattice are considered and interactions with additional bosonic channels are neglected:

$$H = \sum_{i\delta\sigma} J c^{\dagger}_{i+\delta,\sigma} c_{i+\delta,\sigma} + \mu(n_{i\downarrow} + n_{i\uparrow}) + U \sum_{i} (n_{i\uparrow} - \frac{1}{2})(n_{i\downarrow} - \frac{1}{2}). \qquad (6.2)$$

$c^{\dagger}_{i\sigma}$ and $c_{i\sigma}$ denote the creation and annihilation operators for a Fermion on lattice site i with spin σ, J is the hopping integral between neighboring

sites, μ is the chemical potential, n_i is the number of carriers on site i and U is the on-site Coulomb repulsion. The electric field of the pump laser $E(t)$ is applied along the $(1,1)$ direction and enters the Hamiltonian via the Peierls substitution. The parameters were chosen such that, in the absence of an external perturbation ($E(t) = 0$), this Hamiltonian mimics the equilibrium spectra of 1T-TaS_2 [19, 167] with bandwidth $W = 0.36\,\mathrm{eV}$. The dynamics after optical excitation are modeled by perturbing the system with a Gaussian pulse of the form

$$E(t) = E_0 \exp(-4.6(t-t_0)^2/t_0^2)\sin(\omega(t-t_0))$$

where the duration of the pulse t_0 is chosen such that it accommodates a single optical cycle. The frequency ω was chosen to be $\omega/J = 8.0$ and the pulse amplitude was $E_0/(Je) = 2.0$. To solve the electron dynamics, a nonequilibrium dynamical mean field theory (tDMFT) approach [42] is used, which maps a correlated lattice problem onto a self-consistent determined impurity problem [172]. To treat the impurity problem, the lowest order strong coupling expansion, i.e. the noncrossing approximation (NCA) was used. To confirm that the resulting dynamics is qualitatively correct, and not sensitive to the details of the band structure, the one-crossing approximation (OCA) on the Bethe lattice was also employed. Realistic gap sizes are obtained for $U = 0.36\,\mathrm{eV}$ in NCA, and $U = 0.43\,\mathrm{eV}$ in OCA.
The transient occupation dynamics were obtained by computing the partial Fourier transform of the lesser component of the Green's function (occupied density of states):

$$A^<(t,\omega) = Im\left[\int_t^{t+t_{max}} dt' e^{i\omega(t-t')}\right] G^<(t',t).$$

First, the response of the ideal Mott insulator at half band filling ($n = 1$) is discussed and the results are shown in the right panel of figure 6.13(a). The optical excitation results in a partial occupation of the states in the upper Hubbard band over a large energy range that relaxes within the band and results in a slow population build-up at the low energy edge. This finding is not consistent with the experimental observation that shows a quasi-instantaneous occurrence of the UHB signature that does not change its shape with time. It is however in agreement with previous studies [173], which show that the thermalization in an isolated small-gap insulator can lead to an increase in double occupation on the time scale of few inverse hoppings. We note that in contrast to previous theoretical interpretations [19, 20], but in agreement with the experimental data and recent theoretical arguments based on hight temperature expansions [174], the present simulations do not predict a substantial gap filling after photoexcitation.
A more realistic time evolution is given if one considers an effectively hole-doped system. This is a realistic scenario, as pristine high-quality samples

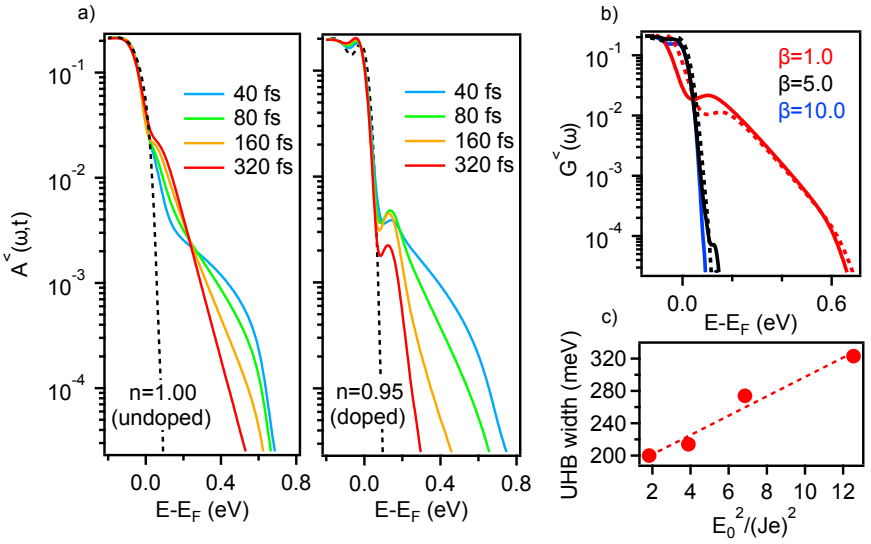

Figure 6.13: Time evolution of the occupation function $G^<(\omega, t)$ for a half-filled band ($n = 1$, left panel) and in the hole-doped case ($n = 0.95$, right panel). The dashed lines show the equilibrium situation before excitation. (b) Equilibrium occupation function $G^<(\omega)$ for $n = 0.98$ (solid lines) and $n = 0.95$ (dashed lines) at different temperatures $\beta = (k_b T)^1$, given in units of W ($\beta = 1$ corresponds to a temperature of 32300 K). (c) Spectral width of the UHB signature at $E - E_F \approx 175$ meV as a function of excitation density E_0^2. The dashed line indicates a linear dependence. From **[158]**

of $1T$-TaS_2 exhibit non-perfect stoichiometric ratios, but they can rather be described as $1T$-$Ta_{(1-x)}S_2$, with x of the order of 0.01 [175]. Such samples, that were also used in our experiments, are characterized by the highest transition temperatures and sharpest resistivity jumps. Assuming that every Ta atom out of a 13-atom superstructure cluster donates four electrons to the surrounding S atoms, we estimate that the effective band filling of the Hubbard bands can range from half filled ($x = 0$, $n = 1$) to quarter-filled ($x = 0.01$, $n = 0.5$). Given that the exact stoichiometric composition of our samples is hard to determine experimentally, we assume a small doping level of $n = 0.95$ to discuss the general influence on the UHB dynamics. The corresponding results are shown in the left panel of figure 6.13(a). In contrast to the half-filled case, the occupation function in the doped case shows a transient increase of the doublon spectral weight, which quickly vanishes. Such evolution is in qualitative agreement with the experimental findings. In agreement with previous works [173, 176] the Hubbard band in the small gap regime thermalizes on the time scale of several inverse hoppings, which was confirmed by checking that the fluctuation-dissipation theorem is fulfilled. Therefore we can compare the results in the long-time limit with the thermal states at elevated temperatures, see figure 6.13 (b). In the half-filled case, the UHB of this small gap system is always substantially occupied

due to the finite overlap of the high-temperature Fermi-Dirac distribution function with the UHB. In the doped case, the Fermi-Dirac distribution is shifted to lower energies and the overlap with the UHB is exponentially suppressed. In such a situation, a significant population in the UHB can only be achieved at extremely high electron temperatures. This also explains the experimental requirement of low excitation densities to observe the ultrafast reduction of the UHB population and is reflected in the experimental finding that the spectral width of the UHB increases linearly with excitation fluence (Fig. 6.12 (b)), which is also reproduced in the theoretical calculation (Fig. 6.13(c)). Notably, even though electron-phonon coupling is important in 1T-TaS_2, we can neglect the phonon dynamics on electronic time scales. In any event, the effect of electron-phonon interactions, as well as short-ranged spin excitations, would be to speed up the relaxation and thermalization [177, 178]. This likely explains the faster dynamics in the experiment, compared to the simulations which neglect this physics.

Large part of the two following section has been reported wordwise from [**159**], which was entirely written by myself.

6.3 Switching to a photoinduced hidden state

A recent time-resolved optical study reported on a photoinduced switching from the many-body insulating ground state to a long-living metallic metastable state in $1T - TaS_2$ [11]. Such a state is not obtained in any of the several equilibrium phases of the material and therefore is referred to as a "hidden" (H) state, which is reached only under non-equilibrium conditions. It was demonstrated that the H state could also be achieved by applying electrical pulses [23, 179, 180] and recent efforts do now aim at microscopic characterization of such a state and the underlying mechanism that leads to its formation [23, 167, 181]. The H state shows metallic properties, suggested by a drop in the resistivity of about two orders of magnitude [11] and confirmed by scanning tunneling microscopy (STM) experiments that, upon switching with electrical pulses, unveiled the formation of textured charge density wave domains, which tunneling spectra indicate final spectral weight at the Fermi level [167]. However, it has been shown that, although the switching to an H state is achieved, different characteristics of such a state can manifest themselves in the presence of different experimental conditions. Different resistivity values with different relaxation properties [180] can be reached upon changing the electric pulse voltage, or different responses in the transient reflectivity [11] shows up for different fluences of the switching laser pulse, or different base temperatures. This is an indication that different configurations of the H state are available under different conditions. In addition, a direct observation of the changes occurring in the electronic structure is not yet available in the literature. In this regard, time- and angle- resolved photoemission, with its ability of accessing the static and transient evolution of the electronic structure, is the ideal tool.

6.3.1 Coherent excitation of the CDW amplitude mode

The H state, probed by tr-optical measurements, mainly manifests itself in a (reversible) modification of the CDW amplitude mode frequencies [11]. Thus, before introducing the photoemission switching experiment, main object of this section, a brief description of the coherently excited oscillations visible in the trARPES spectra is required. Here, we do not aim at a detailed analysis of the coherent oscillations in the system, but only introduce the typical response of the system to the excitation of the CDW, that serves us in the next discussion about the switching to a H state. The analysis of the coherent oscillations can be found in other publications for trARPES [19] and transient optical reflectivity [156, 182, 183].

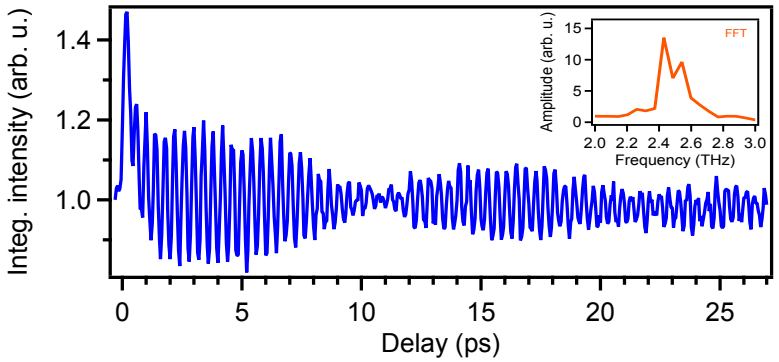

Figure 6.14: Photoemission intensity integrated over an energy window of 40 meV around E_F, as function of time delay. The inset shows the FFT of the data, with two peaks at 2.43 THz and 2.54 THz. From **[159]**

As already introduced in section 6.1,upon optical excitation a strong modulation of the photoemission intensity signal takes place, originating from the pump-induced coherent excitation of the CDW amplitude mode (figure 6.2 (a)), which persists up to tens of ps delay. Such oscillations reflect the breathing mode of the contracted stars and charge density. Figure 6.14 shows the time-dependent intensity of the coherent oscillations obtained by integrating the photoemission signal analogous to figure 6.2 (a) in an interval of 40 meV around E_F. The temperature was 30 K and the excitation fluence was $F = 360\,\mu J/cm^2$. The period of the oscillations is about 0.4 ps, corresponding to a frequency of 2.5 THz, which reflects the breathing mode of the star-shaped clusters together with the charge density. A beating of about 10 ps period suggests the presence of an additional mode. Its frequency is determined by the Fourier transformation of the time-domain signal, as shown in the inset of figure 6.14, where two modes of 2.43 THz and 2.54 THz are found, in agreement with [19], which were assigned to bulk and surface response of the CDW amplitude mode. After 25 ps the oscillations looks strongly damped, in agreement with damping constant determined in [156].

6.3.2 Effect of the switching on the static and time-resolved spectra

We will now show the switching to a metastable H state by strong fs-photoexcitation, starting from the cCDW-Mott insulating (virgin) state and two ways of reverting to the initial equilibrium state by means of infrared ultrashort pulses. The switch (S) was obtained by exposing the system to the pump laser beam with high averaged power, corresponding to an incident fluence of about $F = 3\,mJ/cm^2$ for a minimum of 10 ms (2500 pulses) and up to 200 ms (50000 pulses), similar to [11]. The erase (E) could be

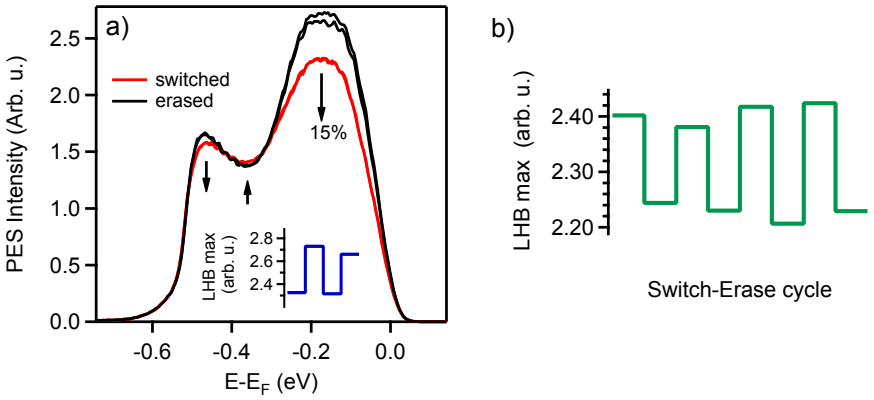

Figure 6.15: Schematics of the switch/erase setup. A flipping mirror (FM) is placed before the compressor in order to use the incoming beam of uncompressed pulses for the E procedure. The optical paths for the delay stage and for alignment onto the sample are omitted for simplicity. a) Comparison of photoemission spectra after switching (red) and after erasing (black) on the same spot. The switching is obtained with compressed pulses at $F = 3\,\mathrm{mJ/cm^2}$ and 50 ms exposure time and the erase with the same beam and exposure time but at $F = 2\,\mathrm{mJ/cm^2}$. The inset shows the corresponding S/E cycle by the sequential loss and recovery of the LHB intensity. b) S/E cycle of another data set where the switching was obtained for 10 ms exposure time and E with the uncompressed beam. From **[159]**

achieved either by exposing the sample for ∼1 s to a train of ps pulses [11], coming from the RegA and bypassing the compressor, or with the same beam and exposure time used for the switching but with less average power, corresponding to $F = 2\,\mathrm{mJ/cm^2}$. The schematics of the laser beams used for this experiment is shown in the experimental setup chapter (see section 4.1). After applying the switching procedure, a flipping mirror was used to pick up the laser beam before entering the compressor and redirected to the same spot on the sample by an alternative optical path. The incident fluence of both the compressed and uncompressed beams could be adjusted by using a combination of non-dispersive filters. Figure 6.15(a) compares static photoemission spectra on the switched (H) and erased virgin (V) states, both achieved using the pump beam (compressed pulses) with an exposure time of 50 ms (12500 pulses) and different incident fluence as explained above. The main feature observed in the H state is a quench of the LHB intensity of about 15% and some minor redistribution of spectral weight within the photoemission spectrum at lower binding energy. These changes remain for an indefinite time (tested up to several hours) without recovering until erased. It was possible to reproduce the H and V state on the same spot in alternating sequence, as shown in the inset of figure 6.15(a). Figure 6.15(b) shows such a S/E cycle for another set of data, where the switching was obtained with 10 ms exposure time and the erasing with the uncompressed

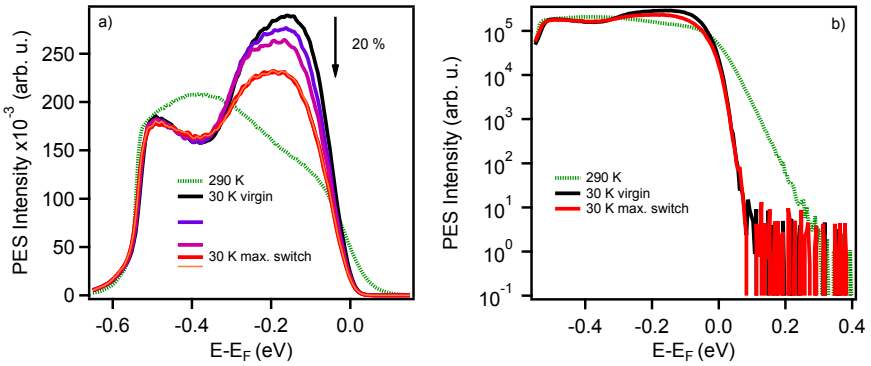

Figure 6.16: Saturation of the switching effect. a) S achieved with $F = 3\,\mathrm{mJ/cm^2}$ and increasing the exposure time. Violet: 10 ms, pink: 120 ms, red: 120 ms (2 times), orange: 200 ms. After reaching 20% drop (red spectrum) the effect is saturated and the spectra measured subsequently perfectly overlap. In b) the spectra in a) are compared with intensity represented on a logarithmic scale. At maximum switching, despite the 20% loss in the LHB intensity, no spectral weight is found towards E_F, suggesting that the system remains in an insulating state. From **[159]**

beam. In this case, the value of the LHB quench is smaller (about 8%) and it should be noted that in both cases the levels of the LHB maxima are not perfectly reproducible, suggesting that the effect does not saturate.

In figure 6.16(a) we show a series of photoemission spectra starting from the V state on which we applied the S beam several times on the same spot with different exposure time. After three subsequent applications of 10 ms and two times 120 ms, respectively, we reached a maximum quench of the LHB of about 20% and further applications with higher exposure time, up to 200 ms, did not produce any additional change, indicating a saturation of the S-induced effects. The same spectra are reported in figure 6.16(b), together with the spectrum in the metallic phase, with the intensity plotted on a logarithmic scale. It is evident that even upon maximum S, no spectral weight is transferred from the LHB into the gapped region towards E_F, indicating that the H state remains insulating and it is therefore different from the one obtained in previous works [11, 167].

In order to verify the impact of the S on the frequency of the coherent CDW amplitude mode, we also performed trARPES measurements on the H and V states, analogous to those presented in figure 6.14 but for a much longer acquisition time window of 60 ps and delay step of the order of one half period of an oscillation cycle. Thereby we obtain a better resolution in the correspondent Fourier transformed frequency spectrum. We proceeded as follow: we first applied the same S procedure as the one for the spectra in figure 6.15(a) and performed the pump-probe measurement with an incident fluence of $140\,\mu\mathrm{J/cm^2}$, sufficient to trigger and detect the coherent oscillations in the photoemission signal, but not high enough to run into

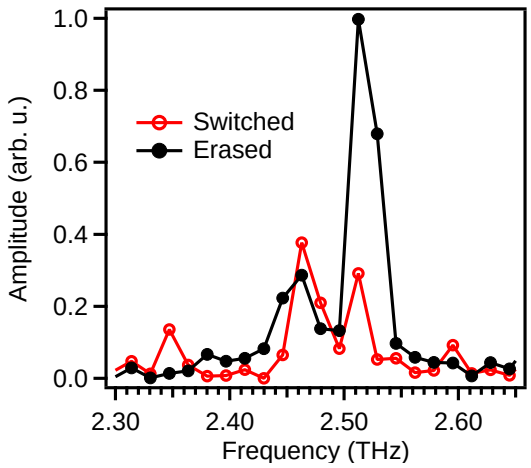

Figure 6.17: Comparison of S and E spectra of the coherent oscillations obtained from FFT of time-dependent data analogous to fig.6.14 but with optimized parameters (see text). The peak at 2.46 THz seems not to be affected by the switching procedure, contrary to the one at 2.51 THz which is drastically reduced. From [**159**]

an undesirable E process due to cumulative pump-induced heating. After verifying the persistence of the H state, by comparing static photoemission spectra before and after the pump-probe measurement, we erased and start an identical time resolved experiment. The results are shown in figure 6.17, comparing the Fast Fourier transformations obtained from the time dependent data (analogous to the inset in figure 6.14) and show that although the peak at lower frequency is basically not affected, the one at 2.51 THz is dramatically reduced in the H state.
From these observations we could conclude that we achieve well defined switching to an H state, which manifests itself in a significant quench of the LHB spectral signature, causing a modification of the electronic structure of the system. Such changes stabilize and do not relax spontaneously to the initial state, but only upon applying an E procedure. Moreover, we observed the fingerprints of the transition to the H state also in the frequencies of the coherently excited CDW amplitude mode. However, the H state reached here shows different properties than the ones observed in [11, 23, 180, 167], as it remains insulating.

6.3.3 Achievment of partial switching

Contrary to the conclusions of previous studies [11, 23, 180, 167], the H state presented in this work is not metallic. At this point it is important to consider the experimental conditions. For the H state obtained with optical pulses [11], the sample was kept at 15 K and a single 35 fs infrared

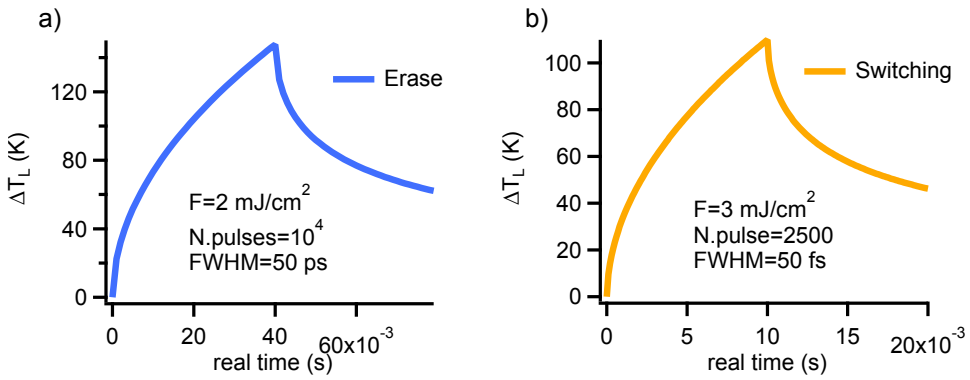

Figure 6.18: Simulation of the photoinduced increase in the lattice temperature ΔT_{L} during (a) the E procedure for the experiment performed by [11] and (b) the switching performed here. The repetition rate was 250 kHz in both cases and the other parameters are reported in the respective graphs.

pulse was used for the switching process. Also for the electrically induced switching, the temperatures were kept below 5 K [23, 167], while we conducted our experiment at 30 K. One should keep in mind that the erasing of the H state occurs as a consequence of Joule heating. Therefore we consider that the energy deposited by the train of switching pulses, results in a sample temperature close to the threshold for the erase process, estimated to around 150 K [11], as shown in figure 6.18 (a). We calculated the transient increase in the lattice temperature (ΔT_{L}) with the same method as employed in [11] and the results are shown in figure 6.18 (b). We obtained $\Delta T_{\mathrm{L}} = 110\,\mathrm{K}$ (the parameters are those described for the S in figure 6.15(a): $F = 3\,\mathrm{mJ/cm^2}$, 2500 pulses), which means a maximum transient lattice temperature of 140 K, very close to the erase threshold. This transient high temperature hinders the switching process, leading to effectively partial S and the system heading off to an H state which probably represents a different local minimum of the free energy of the system. The temperature dependent study of the switching [180] also reports instabilities of the voltage-versus-current behavior starting from $\sim 50\,\mathrm{K}$. We would like to remark that the most limiting parameter here is the starting base temperature, as it has been demonstrated that the complete S can be achieved also by using a train of pulses instead of a single one [11], analogous to our case, provided that the initial temperature is sufficiently low. Although the previous considerations hold, it is fair to mention that the origin of the E obtained with fs pulses but lower F remains unclear. However, although no metallic character is obtained, significant changes in the photoemission spectrum occur, clearly indicated by the significant reduction of the LHB intensity. As explained in the two previous sections, the latter can be regarded as a direct signature for charge order and would therefore point to a quench of

charge order, in agreement with the previous studies [11, 167]. The changes in the frequency spectrum of the CDW amplitude mode (figure 6.17) are also another clear indication of the important modifications of the cCDW structure occurring upon switching. In particular the peak at 2.51 THz is shown to almost completely vanish in the H state. Thus, since the H state under investigation does not develop a metallic character, we can conclude that the high frequency peak is not linked to the metal properties of the system.

6.4 Summary

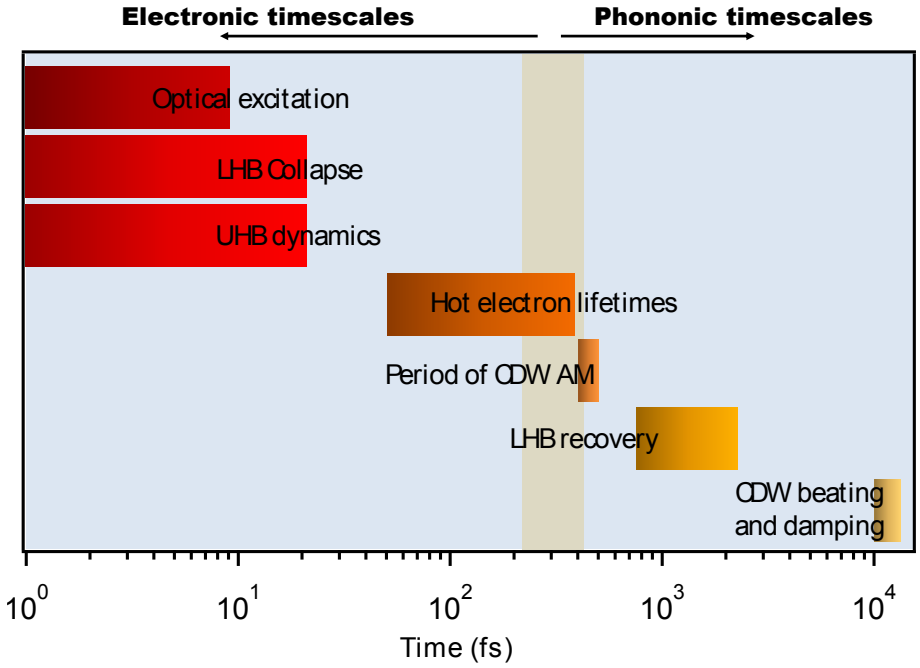

Figure 6.19: Summary of the identified timescales for photo-excited 1T-TaS$_2$ in the cCDW-Mott phase, which extend over five orders of magnitude.

We presented a systematic temperature- and fluence-dependent trARPES study on 1T-TaS$_2$, through which we characterized the transient photoinduced phase and observed the population dynamics of the UHB. The identified timescales are summarized in figure 6.19. The quench of the LHB occurring upon photo-excitation directly reflects the reduction in the correlation strength, that can reach up to 90% in the strong excitation regime. However, from the analysis of the energy-dependent relaxation times as a function of fluence and temperature, we could conclude that the system is not driven into its conductive state and the excitation process is of a localized nature suggesting a real space description of the photoinduced state in which single polaron sites are excited and coexist with unperturbed sites in an unordered manner. From the strong mismatch between the timescales of the LHB recovery and the relaxation of the hot electrons population, we concluded that while electron-phonon interaction is the major energy loss channel for the electronic systems excess energy, it cannot be solely responsible for the complete relaxation of the system into its original ground state, but more complex processes of electronic nature must be important and should be considered for the re-establishment of charge order.

In the weak excitation limit, the UHB was observed, indicating the tran-

sient population of doublon states. We analyzed the time evolution of the UHB and based on our results we concluded that the relevant timescales for photoinduced disorder and the subsequent dynamics in the electronic subsystem of this Mott-insulator are of the order of the electronic hopping cycle $\hbar/J$. The time-domain approach was essential, as it enabled the detection of the doublon state before further excitation, like secondary electrons or phonons, would mask the UHB. The electronic and phononic subsystems are decoupled on early stages after photo-perturbation which (i) is the hallmark of non-equilibrium dynamics and (ii) allows for a significant reduction of complexity by only considering the electronic part of the system. While electron-phonon coupling plays a significant role and serve as, e.g. an energetic loss channel for the electrons on longer time scales, the dynamics on ultrafast timescales, thermalization of carriers in the UHB and subsequent decay of its occupation do not require such coupling. From preliminary results of a theoretical modeling obtained with a tDMFT approach, we concluded that the dynamics of the transient population of the doublon states are governed by the effective band filling and our results are best reproduced in the case of a slightly hole-doped system. This finding might be transferable to other Mott insulators in which simultaneously strong coupling of different degrees of freedom make theoretical modeling challenging.

At last, we presented first switching experiments on this material with the trARPES setup, showing that at T=30 K a metastable H state is reached upon intense photoexcitation, which can be reverted to the initial cCDW-Mott state by applying a train of either picosecond or femtosecond pulses. The H state is characterized by a 20% reduction of the LHB intensity, while the material shows no metallic character at $k_{\parallel} = \Gamma$. We therefore conclude that the H state reached and investigated in the present work is different from the one observed in previous studies [11, 23, 180, 167] and that the metallic state is not reached, due to partial switching in the presence of a transient lattice temperature close to the erase temperature threshold. However, the reduction of the LHB and the changes in the high frequency peak of the CDW amplitude mode, occurring upon switching, are indicative of a reduction in the degree of charge order, in agreement with the results of previous studies [11, 167]. This work demonstrates that H states can be probed by means of trARPES, which is the ideal tool to investigate the microscopic changes of the system directly in the electronic structure as a function of energy, momentum and time-delay.

Chapter 7

Conclusions and Outlook

The present work reported on ultrafast trARPES study on complex chemically doped materials in which $e-e$ correlations and coupling to other degrees of freedom gives rise to the emergence of different competing ground states and novel photoinduced states.

A systematic doping-dependent study was carried on the Fe-based HTSC $\mathbf{Ba(Fe}_{1-x}\mathbf{Co}_x)_2\mathbf{As}_2$ in the normal state. The relaxation of the excited electrons' population around the BZ center was analyzed as function of binding energy and fluence revealing a doping-dependence of the relaxation times that does not monotonously follow the carrier concentration, with the fastest relaxation occurring at optimal doping. This observation, in qualitative agreement with the results obtained from transport measurements [25, 24], originates from the vertical dispersion of the 3D Fermi surface of these compounds and the probe photon energy. We showed that we probe at a finite k_{Z} value between Γ and Z where additional contributions to the relaxation from interband scattering are available in the case of the optimally doped compound but absent in the overdoped. The comparison between scattering rates obtained by static ARPES, probing single-particle lifetimes from occupied states by linewidth analysis, and the ones obtained in the present work by trARPES was extensively discussed. The difference of almost two orders of magnitudes in the correspondent values is in agreement with analogous studies performed on cuprates HTSCs [140] and is the confirmation that these methods probe two different quantities.
The key observation came from the analysis of the energy-dependent relaxation rates, in which a step around the energy of $E - E_{\mathrm{F}} = 200\,\mathrm{meV}$ was identified at low excitation densities. The fluence dependence of the step and the fact that it occurs at the same energy for all dopings, indicates a coupling of the electronic system to a boson, in agreement with theoretical description [146, 147]. From the energy at which the step occurs and comparison with literature, the magnetic origin of such a boson was suggested. This observation further supports the recently published work on

cuprates [32]. Notably, such observation originated from the analysis of the non-equilibrium regime, while in the equilibrium electronic structure, no indication of such coupling is present, contrary to the case of the cuprates.
An additional confirmation of the magnetic nature of the boson could come from studies on hole doped compounds, since neutron scattering data suggest that the mode at $E - E_F = 200\,\text{meV}$ should be absent [151, 152]. Moreover, it would be interesting to perform studies on isovalent doped compounds, to establish whether the electron-boson coupling effect is a more general feature in 122-compounds in general.

A systematic temperature- and fluence-dependent trARPES study on **1*T*-TaS$_2$** in the CDW-Mott phase was presented aiming at the characterization of the transient photoinduced state. The key observation was the transient population of the UHB, most prominent in the weak excitation regime, a spectral feature reflecting the transient population of doubly occupied states. From the analysis of its time evolution, which is of the order of the characteristic timescales of hopping, we concluded on the decoupling of electronic and phononic subsystem at early stages after photo-perturbation. While electron-phonon coupling plays a significant role in the dissipation of the excess energy on longer timescales, the thermalization and occupation's decay of carriers within the UHB do not require such coupling but are only governed by $e - e$ interactions and effective band filling. This finding might be transferable to other Mott insulators in which simultaneously strong coupling of different degrees of freedom make theoretical modeling challenging, as the decoupling of electronic and phononic system at early stages after optical excitation allows for a significant reduction in complexity by only considering the electronic part of the system.
On the same system, switching experiments were performed employing IR ultrashort optical pulses, aiming at reaching the metastable hidden state [11]. Such state was analyzed for the first time by means of static and trARPES and let conclude on the observation of partial switching, leading to significant changes in the electronic structure of the system, although preserving insulating properties. In the frequency spectrum of the excited CDW amplitude mode, the amplitude of the peak at 2.51 THz is drastically reduced, while a second peak at slightly lower frequency is instead unaffected upon switching. Since the system remains insulating, it was concluded that the peak at higher frequency is not related to the metallic properties. From simulations based on the same modeling used in [11], we estimated that the transient laser induced heating during switching is close to the erase temperature threshold, which is the reason for partial switching. Thus, future experiments should aim at overcoming this hindrance and an effective way to do so would be to reduce the starting base temperature. Moreover, employing other materials, like Se-doped 1T-TaS$_2$, exhibiting similar effect but at higher temperature will undoubtedly decrease the experimental challenges.

Bibliography

[1] U. Bovensiepen and P. S. Kirchmann. Elementary relaxation processes investigated by femtosecond photoelectron spectroscopy of two-dimensional materials. *Laser & Photonics reviews*, 6:589, 2012.

[2] E. Morosan, D. Natelson, A. H. Nevidomskyy, and Q. Si. Strongly correlated materials. *Advanced Materials*, 24:4896, 2012.

[3] T. Valla, A. V. Fedorov, P. D. Johnson, and S. L. Hulbert. Many-body effects in angle-resolved photoemission: Quasiparticle energy and lifetime of a Mo(110) surface state. *Phys. Rev. Lett.*, 83:2085, 1999.

[4] A. Damascelli, Z. Hussain, and Z.-X. Shen. Angle-resolved photoemission studies of the cuprate superconductors. *Rev. Mod. Phys.*, 75:473, 2003.

[5] W. S. Lee, S. Johnston, T. P. Devereaux, and Z.-X. Shen. Aspects of electron-phonon self-energy revealed from angle-resolved photoemission spectroscopy. *Phys. Rev. B*, 75:195116, 2007.

[6] P. Richard, T. Sato, K. Nakayama, T. Takahashi, and H. Ding. Fe-based superconductors: an angle-resolved photoemission spectroscopy perspective. *Reports on Progress in Physics*, 74:124512, 2011.

[7] C. Giannetti, M. Capone, D. Fausti, M. Fabrizio, F. Parmigiani, and D. Mihailovic. Ultrafast optical spectroscopy of strongly correlated materials and high-temperature superconductors: a non-equilibrium approach. *Advances in Physics*, 65:58, 2016.

[8] S. Hellmann, T. Rohwer, M. Kalläne, K. Hanff, A. Stange, A. Carr, M. M. Murnane, H. C. Kapteyn, L. Kipp, M. Bauer, and K. Rossnagel. Time-domain classification of charge-density-wave insulators. *Nature Comm.*, 3:999, 2012.

[9] D. Lu, I. M. Vishik, M. Yi, Y. Chen, R. G. Moore, and Shen Z.-X. Angle-resoved photoemission studies of quantum materials. *Annu. Rev. Condens. Matter Phys.*, 3:129, 2012.

[10] H. Schäfer, V. V. Kabanov, M. Beyer, K. Biljakovic, and J. Demsar. Disentanglement of the electronic and lattice parts of the order parameter in a 1D charge density wave system probed by femtosecond spectroscopy. *Phys. Rev. Lett.*, 105:066402, 2010.

[11] L. Stojchevska, I. Vaskivskyi, T. Mertelj, P. Kusar, D. Svetin, Brazovskii S., and D. Mihailovic. Ultrafast switching to a stable hidden quantum state in an electronic crystal. *Science*, 344:177, 2014.

[12] J. A. Sobota, S. Yang, J. G. Analytis, Y. L. Chen, I. R. Fisher, P. S. Kirchmann, and Z.-X. Shen. Ultrafast optical excitation of a persistent surface-state population in the topological insulator Bi_2Se_3. *Phys. Rev. Lett.*, 108:117403, 2012.

[13] D. Fausti, R. I. Tobey, N. Dean, S. Kaiser, A. Dienst, M. C. Hoffmann, S. Pyon, T. Takayama, H. Takagi, and A. Cavalleri. Light-induced superconductivity in a striped order cuprate. *Science*, 331:189, 2011.

[14] K. Nasu, H. Ping, and Mizouchi H. Photoinduced structural phase transitions and their dynamics. *J. Phys.: Condens. Matter*, 13:R693, 2001.

[15] P. Fazekas and E. Tosatti. Charge carrier localization in pure and doped 1T-TaS_2. *Physica B+C*, 99:183, 1980.

[16] S. van Smaalen. The Peierls transition in low-dimensional electronic crystals. *Acta Crystallog. Sect. A*, 61:51, 2005.

[17] F. Clerc, C. Battaglia, H. Cercellier, C. Monney, H. Berger, L. Despont, M. G. Garnier, and P. Aebi. Fermi surface of layered compounds and bulk charge density wave systems. *Journal of Physics: Condensed Matter*, 19:355002, 2007.

[18] B. Sipos, A. F. Kusmartseva, A. Akrap, H. Berger, L. Forró, and E. Tutiš. From Mott state to superconductivity in 1T-TaS_2. *Nature Materials*, 7:960, 2008.

[19] L. Perfetti, P. A. Loukakos, M. Lisowski, U. Bovensiepen, H. Berger, S. Biermann, P. S. Cornaglia, A. Georges, and M. Wolf. Time evolution of the electronic structure of 1T-TaS_2 through the insulator-metal transition. *Phys. Rev. Lett.*, 97:067402, 2006.

[20] L. Perfetti, P. A. Loukakos, M. Lisowski, U. Bovensiepen, M. Wolf, H. Berger, S. Biermann, and A. Georges. Femtosecond dynamics of electronic states in the mott insulator 1T-TaS_2 by time resolved photoelectron spectroscopy. *New Journal of Physics*, 10:053019, 2008.

[21] F. Schmitt, P. S. Kirchmann, U. Bovensiepen, R. G. Moore, L. Rettig, M. Krenz, J.-H. Chu, N. Ru, L. Perfetti, D. H. Lu, M. Wolf, I.R. Fisher, and Z.-X. Shen. Transient electronic structure and melting of a charge density wave in $TbTe_3$. *Science*, 321:1649, 2008.

[22] N. Dean, J. C. Petersen, D. Fausti, R. I. Tobey, S. Kaiser, L. V. Gasparov, H. Berger, and A. Cavalleri. Polaronic conductivity in the photoinduced phase of 1T-TaS_2. *Phys. Rev. Lett.*, 106:016401, 2011.

[23] I. Vaskivskyi, J. Gospodaric, Brazovskii S., D. Svetin, P. Sutar, E. Goreshnik, I. A. Mihailovic, T. Mertelj, and D. Mihailovic. Controlling the metal-to-insulator relaxation of the metastable hidden quantum state in 1T-TaS_2. *Science Adv.*, 1:e1500168, 2015.

[24] F. Rullier-Albenque, D. Colson, A. Forget, and H. Alloul. Hall effect and resistivity study of the magnetic transition, carrier content, and Fermi-liquid behavior in $Ba(Fe_{1-x}Co_x)_2As_2$. *Phys. Rev. Lett.*, 103:057001, 2009.

[25] N. Katayama, Y. Kiuchi, Y. Matsushita, and K. Ohgushi. Variation in electronic state of $Ba(Fe_{1-x}Co_x)_2As_2$ alloy as investigated in terms of transport properties. *Journal of the Physical Society of Japan*, 78:123702, 2009.

[26] M.M. Qazilbash, J.J. Hamlin, R.E. Baumbach, L. Zhang, D. J. Singh, M.B. Maple, and D. N. Basov. Electronic correlations in the iron pnictides. *Nature Physics*, 5:647, 2009.

[27] M. Nakajima, S. Ishida, T. Tanaka, K. Kihou, Y. Tomioka, T. Saito, C. H. Lee, H. Fukazawa, Y. Kohori, T. Kakeshita, A. Iyo, T. Ito, H. Eisaki, and S. Uchida. Normal-state charge dynamics in doped $BaFe_2As_2$: Roles of doping and necessary ingredients for superconductivity. *Sci. Rep.*, 4(5873), 2014.

[28] Q. Si, R. Yu, and E. Abrahams. High-temperature superconductivity in iron pnictides and chalcogenides. *Nature Reviews Materials*, 1:1, 2016.

[29] M. Yi, D. H. Lu, J. G. Analytis, J.-H. Chu, S.-K. Mo, R.-H. He, R. G. Moore, X. J. Zhou, G. F. Chen, J. L. Luo, N. L. Wang, Z. Hussain, D. J. Singh, I. R. Fisher, and Z.-X. Shen. Electronic structure of the $BaFe_2As_2$ family of iron-pnictide superconductors. *Phys. Rev. B*, 80:024515, 2009.

[30] E. D. L. Rienks, T. Wolf, K. Koepernik, I. Avigo, P. Hlawenka, C. Lupulescu, T. Arion, F. Roth, W. Eberhardt, U. Bovensiepen, and J. Fink. Electronic structure and quantum criticality in

$Ba(Fe_{1-x-y}Co_xMn_y)_2As_2$, an ARPES study. *Europhys. Letters*, 103:47004, 2013.

[31] J. Fink, A. Charnukha, E. D. L. Rienks, Z. H. Liu, S. Thirupathaiah, I. Avigo, F. Roth, H. S. Jeevan, P. Gegenwart, M. Roslova, I. Morozov, S. Wurmehl, U. Bovensiepen, S. Borisenko, M. Vojta, and B. Büchner. Non-Fermi-liquid scattering rates and anomalous band dispersion in ferropnictides. *Phys. Rev. B*, 92:201106, 2015.

[32] J. D. Rameau, S. Freutel, A. F. Kemper, M. A. Sentef, J. K. Freericks, I. Avigo, M. Ligges, L. Rettig, Y. Yoshida, H. Eisaki, J. Schneeloch, R. D. Zhong, Z. J. Xu, G. D. Gu, P. D. Johnson, and U. Bovensiepen. Energy dissipation from a correlated system driven out of equilibrium. *Nature Communications*, 7:13761, 2016.

[33] L. D. Landau. The theory of a Fermi liquid. *Soviet Phys. JETP*, 3:920, 1957.

[34] R. O. Jones and O. Gunnarsson. The density functional formalism, its applications and prospects. *Rev. Mod. Phys.*, 61:689, 1989.

[35] N.F. Mott. Metal-insulator transition. *Rev. mod. Phys.*, 40:677, 1968.

[36] N. F. Mott. The basis of the electron theory of metals, with special reference to the transition metals. *Proceedings of the Physical Society. Section A*, 62:416, 1949.

[37] J. H. de Boer and e. J. W. Verwey. Semi-conductors with partially and with completely filled 3d -lattice bands. *Proceedings of the Physical Society*, 49:59, 1937.

[38] J. Hubbard. Electron correlations in narrow energy bands. *Proc. of the Royal Soc. of London*, 276, 1963.

[39] G. Kotliar and D. Vollhardt. Strongly correlated materials: Insights from dynamical mean-field theory. *Physics Today*, 57:53, 2004.

[40] T. Watanabe, H. Yokoyama, Y. Tanaka, and J.-i. Inoue. Superconductivity and a Mott transition in a Hubbard model on an anisotropic triangular lattice. *Journal of the Physical Society of Japan*, 75:074707, 2006.

[41] P. Prelovšek, J. Kokalj, Z. Lenarčič, and R. H. McKenzie. Holon-doublon binding as the mechanism for the Mott transition. *Phys. Rev. B*, 92:235155, 2015.

[42] H. Aoki, N. Tsuji, M. Eckstein, M. Kollar, T. Oka, and P. Werner. Nonequilibrium dynamical mean-field theory and its applications. *Rev. Mod. Phys.*, 86:779, 2014.

[43] G. Grüner. *Density waves in solids*, volume 89. Perseus publishing, 1994.

[44] R. E. Peierls. *Quantum theory of Solids*. Oxford University Press, 1955.

[45] H. Fröhlich. On the theory of superconductivity: the one-dimensional case. *Proceedings of the Royal Society A*, 223:296, 1954.

[46] A. J. Berlinsky. One-dimensional metals and charge density wave effects in these materials. *Reports on Progress in Physics*, 42:1243, 1979.

[47] T. Rower, S. Hellmann, M. Wiesenmayer, C. Sohrt, Stange A., B. Slomski, A. Carr, Y. Liu, L. M. Avila, M. Kalläne, S. Mathias, L. Kipp, K. Rossnagel, and Bauer M. Collapse of long-range charge order tracked by time-resolved photoemission at high momenta. *Nature*, 471:490, 2011.

[48] J. C. Petersen, S. Kaiser, N. Dean, A. Simoncig, H. Y. Liu, A. L. Cavalieri, C. Cacho, I. C. E. Turcu, E. Springate, F. Frassetto, L. Poletto, S. S. Dhesi, H. Berger, and A. Cavalleri. Clocking the melting transition of charge and lattice order in 1T-TaS_2 with ultrafast extreme-ultraviolet angle-resolved photoemission spectroscopy. *Phys. Rev. Lett.*, 107:177402, 2011.

[49] A. Einstein. Generation and conversion of light with regard to a heuristic point of view. *Annalen der Physik*, 17, 1905.

[50] S. Hüfner. *Photoelectron Spectroscopy*. Springer, Heidelberg, 2003.

[51] J. D. Koralek, J. F. Douglas, N. C. Plumb, Z. Sun, A. V. Fedorov, M. M. Murnane, H. C. Kapteyn, S. T. Cundiff, Y. Aiura, K. Oka, H. Eisaki, and D. S. Dessau. Laser based angle-resolved photoemission, the sudden approximation, and quasiparticle-like spectral peaks in $Bi_2Sr_2CaCu_2O_{8+\delta}$. *Phys. Rev. Lett.*, 96:017005, 2006.

[52] M. P. Seah and A. Dench. Quantitative electron spectroscopy of surfaces: A standard data base for electron inelastic mean free paths in solids. *Surface and Interface Analysis*, 1:2, 1979.

[53] T. Kiss, F. Kanetaka, T. Yokoya, T. Shimojima, K. Kanai, S. Shin, Y. Onuki, T. Togashi, C. Zhang, C. T. Chen, and S. Watanabe. Photoemission spectroscopic evidence of gap anisotropy in an f-electron superconductor. *Phys. Rev. Lett.*, 94:057001, 2005.

[54] L. Rettig, R. Cortés, S. Thirupathaiah, P. Gegenwart, H. Jeevan, M. Wolf, J. Fink, and U. Bovensiepen. Ultrafast momentum-dependent response of electrons in antiferromagnetic $EuFe_2As_2$ driven by optical excitation. *Phys. Rev. Lett.*, 108:097002, 2012.

[55] L. Rettig, P. S. Kirchmann, and U. Bovensiepen. Ultrafast dynamics of occupied quantum well states in Pb/Si(111). *New Journal of Physics*, 14:023047, 2012.

[56] P. A. Loukakos, M. Lisowski, G. Bihlmayer, S. Blügel, M. Wolf, and U. Bovensiepen. Dynamics of the self-energy of the Gd(0001) surface state probed by femtosecond photoemission spectroscopy. *Phys. Rev. Lett.*, 98:097401, 2007.

[57] Bovensiepen U., H. Petek, and M. Wolf, editors. *Dynamics at Solis State Surfaces and Interfaces*, volume 1:Current Developements. Wiley-VCH, 2011.

[58] W. Schattke. Electron scattering states for low-energy spectroscopies. *Progress in Surface Science*, 64:89, 2000.

[59] P. Vilmercati, A. Fedorov, I. Vobornik, U. Manju, G. Panaccione, A. Goldoni, A. S. Sefat, M. A. McGuire, B. C. Sales, R. Jin, D. Mandrus, D. J. Singh, and N. Mannella. Evidence for three-dimensional fermi-surface topology of the layered electron-doped iron superconductor $Ba(Fe_{1-x}Co_x)_2As_2$. *Phys. Rev. B*, 79:220503, 2009.

[60] S. Thirupathaiah, S. de Jong, R. Ovsyannikov, H. A. Dürr, A. Varykhalov, R. Follath, Y. Huang, R. Huisman, M. S. Golden, Yu-Zhong Zhang, H. O. Jeschke, R. Valentí, A. Erb, A. Gloskovskii, and J. Fink. Orbital character variation of the Fermi surface and doping dependent changes of the dimensionality in $BaFe_{2-x}Co_xAs_2$ from angle-resolved photoemission spectroscopy. *Phys. Rev. B*, 81:104512, 2010.

[61] B. Burk, R. E. Thomson, J. Clarke, and A. Zettl. Surface and bulk charge density wave structure in 1T-TaS_2. *Science*, 257:362, 1992.

[62] H. Petek and S. Ogawa. Femtosecond time-resolved two-photon photoemission studies of electron dynamics in metals. *Progress in Surface Science*, 56:239, 1997.

[63] M. Weinelt. Time-resolved two-photon photoemission from metal surfaces. *Journal of Physics: Conde*, 14:R1099, 2002.

[64] P.M. Echenique, R. Berndt, E.V. Chulkov, T. Fauster, Goldmann. A., and U. Höfer. Decay of electronic excitations at metal surfaces. *Surface Science Reports*, 52:219, 2004.

[65] P. S. Kirchmann, L. Rettig, X. Zubizzarreta, V. M. Silkin, E. V. Chulkov, and U. Bovensiepen. Quasiparticle lifetimes in metallic quantum-well nanostructures. *Nature Physics*, 6:782, 2010.

[66] J. A. Sobota, S.-L. Yang, A. F. Kemper, J. J. Lee, F. T. Schmitt, W. Li, R. G. Moore, J. G. Analytis, I. R. Fisher, P. S. Kirchmann, T. P. Devereaux, and Z.-X. Shen. Direct optical coupling to an unoccupied dirac surface state in the topological insulator Bi_2Se_3. *Phys. Rev. Lett.*, 111:136802, 2013.

[67] W.-L. Chan, M. Ligges, A. Jailaubekov, L. Kaake, L. Miaja-Avila, and X.-Y. Zhu. Observing the multiexciton state in singlet fission and ensuing ultrafast multielectron transfer. *Science*, 334:1541, 2011.

[68] X. Cui, C. Wang, A. Argondizzo, S. Garret-Roe, B. Gumhalter, and H. Petek. Transient excitons at metal surfaces. *Nature Physics*, 10:505, 2014.

[69] L. Rettig. *Ultrafast Dynamics of Correlated Electrons*. PhD thesis, Freien Universität Berlin, 2012.

[70] B. Rethfeld, A. Kaiser, M. Vicanek, and G. Simon. Ultrafast dynamics of nonequilibrium electrons in metals under femtosecond laser irradiation. *Phys. Rev. B*, 65:214303, 2002.

[71] M. Lisowski, P.A. Loukakos, U. Bovensiepen, J. Stähler, and M. Wolf. Ultra-fast dynamics of electron thermalization, cooling and transport effects in Ru(001). *Applied Physics A: Material science & processing*, 78, 2004.

[72] E. Knoesel, A. Hotzel, T. Hertel, M. Wolf, and G. Ertl. Dynamics of photoexcited electrons in metals studied with time-resolved two-photon photoemission. *Surface Science*, 368:76, 1996.

[73] C. L. Smallwood, W. Zhang, T. L. Miller, C. Jozwiak, H. Eisaki, D.-H. Lee, and A. Lanzara. Time- and momentum-resolved gap dynamics in $Bi_2Sr_2CaCu_2O_{8+\delta}$. *Phys. Rev. B*, 89:115126, 2014.

[74] L. Rettig, R. Cortés, J.-H. Chu, Fisher I. R., F. Schmith, R. G. Moore, Z-X Shen, P. S. Kirchmann, M. Wolf, and U. Bovensiepen. Persistent order due to transiently enhanced nesting in an electronically excited charge density wave. *Nature Communications*, 7:10459, 2016.

[75] L. Perfetti, P. A. Loukakos, M. Lisowski, U. Bovensiepen, H. Eisaki, and M. Wolf. Ultrafast electron relaxation in superconducting $Bi_2Sr_2CaCu_2O_{8+\delta}$ by time-resolved photoelectron spectroscopy. *Phys. Rev. Lett.*, 99:197001, 2007.

[76] I. Gierz, J. C. Petersen, M. Mitrano, C. Cacho, I. C. E. Turcu, E. Springate, A. Stöhr, A. Köhler, U. Starke, and A. Cavalleri. Snapshots of non-equilibrium Dirac carrier distributions in graphene. *Nature Materials*, 12:1119, 2013.

[77] S. Ulstrup, J. C. Johannsen, F. Cilento, J. A. Miwa, A. Crepaldi, M. Zacchigna, C. Cacho, R. Chapman, E. Springate, S. Mammadov, F. Fromm, C. Raidel, T. Seyller, F. Parmigiani, M. Grioni, P. D. C. King, and P. Hofmann. Ultrafast dynamics of massive Dirac fermions in bilayer graphene. *Phys. Rev. Lett.*, 112:257401, 2014.

[78] L. X. Yang, G. Rohde, T. Rohwer, A. Stange, K. Hanff, C. Sohrt, L. Rettig, R. Cortés, F. Chen, D. L. Feng, T. Wolf, B. Kamble, I. Eremin, T. Popmintchev, M. M. Murnane, H. C. Kapteyn, L. Kipp, J. Fink, M. Bauer, U. Bovensiepen, and K. Rossnagel. Ultrafast modulation of the chemical potential in $BaFe_2As_2$ by coherent phonons. *Phys. Rev. Lett.*, 112:207001, 2014.

[79] U. Bovensiepen, A. Melnikov, I. Radu, O. Krupin, K. Starke, M. Wolf, and E. Matthias. Coherent surface and bulk vibrations induced by femtosecond laser excitation of the Gd(0001) surface state. *Phys. Rev. B*, 69:235417, 2004.

[80] M. Lisowski, P. A. Loukakos, A. Melnikov, I. Radu, L. Ungureanu, M. Wolf, and U. Bovensiepen. Femtosecond electron and spin dynamics in Gd(0001) studied by time-resolved photoemission and magneto-optics. *Phys. Rev. Lett.*, 95:137402, 2005.

[81] I. Avigo, R. Cortés, L. Rettig, S. Thirupathaiah, H. S. Jeevan, P. Gegenwart, T. Wolf, M. Ligges, M. Wolf, J. Fink, and U. Bovensiepen. Coherent excitations and electron-phonon coupling in $Ba/EuFe_2As_2$ compounds investigated by femtosecond time- and angle-resolved photoemission spectroscopy. *Journal of Physics: Condensed Matter*, 25:094003, 2013.

[82] Y. Kamihara, T. Watanabe, M. Hirano, and H. Hosono. Iron-based layered superconductor $LaO_{1-x}F_xFeAs$ ($x = 0.05 - 0.12$) with $T_c =$ 26K. *J. Am. Chem. Soc.*, 130:3296, 2008.

[83] J. Paglione and R. L. Greene. High-temperature superconductivity in iron-based materials. *Nat Phys*, 6:645, 2010.

[84] A. Chubukov and P. J. Hirschfeld. Iron-based superconductors, seven years later. *Physics Today*, 68:46, 2015.

[85] Igor I. Mazin. Superconductivity gets an iron boost. *Nature*, 464(7286):183, 2010.

[86] H. Luetkens, H.-H. Klauss, M. Kraken, F. J. Litterst, T. Dellmann, R. Klingeler, C. Hess, R. Khasanov, A. Amato, C. Baines, M. Kosmala, O. J. Schumann, M. Braden, J. Hamann-Borrero, N. Leps, A. Kondrat, G. Behr, J. Werner, and B. Buchner. The electronic phase diagram of the $LaO_{1-x}F_xFeAs$ superconductor. *Nature Materials*, 8:305, 2009.

[87] J. Dai, Q. Si, J. Zhu, and E. Abrahams. Iron pnictides as a new setting for quantum criticality. *Proceedings of the National Academy of Sciences*, 106:4118, 2009.

[88] E. Abrahams and Q. Si. Quantum criticality in the iron pnictides and chalcogenides. *Journal of Physics: Condensed Matter*, 23:223201, 2011.

[89] K. Hashimoto, K. Cho, T. Shibauchi, S. Kasahara, Y. Mizukami, R. Katsumata, Y. Tsuruhara, T. Terashima, H. Ikeda, M. A. Tanatar, H. Kitano, N. Salovich, R. W. Giannetta, P. Walmsley, A. Carrington, R. Prozorov, and Y. Matsuda. A sharp peak of the zero-temperature penetration depth at optimal composition in $BaFe_2(As_{1-x}P_x)_2$. *Science*, 336:1554, 2012.

[90] J. Chu, J. G. Analytis, K. De Greve, P. L. McMahon, Z. Islam, Y. Yamamoto, and I. R. Fisher. In-plane resistivity anisotropy in an underdoped iron arsenide superconductor. *Science*, 329:824, 2010.

[91] J. G. Analytis, H-H. Kuo, R. D. McDonald, M. Wartenbe, P. M. C. Rourke, N. E. Hussey, and I.R. Fisher. Transport near a quantum critical point in $BaFe_2(As_{1-x}P_x)_2$. *Nature Physics*, 10:194, 2014.

[92] M. Nakajima, T. Liang, S. Ishida, Y. Tomioka, K. Kihou, C. H. Lee, A. Iyo, H. Eisaki, T. Kakeshita, T. Ito, and S. Uchida. Unprecedented anisotropic metallic state in undoped iron arsenide $BaFe_2As_2$ revealed by optical spectroscopy. *Proceedings of the National Academy of Sciences*, 108:12238, 2011.

[93] C. Meingast, F. Hardy, R. Heid, P. Adelmann, A. Böhmer, P. Burger, D. Ernst, R. Fromknecht, P. Schweiss, and T. Wolf. Thermal expansion and grüneisen parameters of $Ba(Fe_{1-x}Co_x)_2As_2$: A thermodynamic quest for quantum criticality. *Phys. Rev. Lett.*, 108:177004, 2012.

[94] Y. Nakai, T. Iye, S. Kitagawa, K. Ishida, S. Kasahara, T. Shibauchi, Y. Matsuda, H. Ikeda, and T. Terashima. Normal-state spin dynamics in the iron-pnictide superconductors $BaFe_2(As_{1-x}P_x)_2$ and $Ba(Fe_{1-x}Co_x)_2As_2$ probed with NMR measurements. *Phys. Rev. B*, 87:174507, 2013.

[95] C. Lester, Jiun-Haw Chu, J. G. Analytis, S. C. Capelli, A. S. Erickson, C. L. Condron, M. F. Toney, I. R. Fisher, and S. M. Hayden. Neutron scattering study of the interplay between structure and magnetism in $Ba(Fe_{1-x}Co_x)_2As_2$. *Phys. Rev. B*, 79:144523, 2009.

[96] Q. Huang, Y. Qiu, Wei Bao, M. A. Green, J. W. Lynn, Y. C. Gasparovic, T. Wu, G. Wu, and X. H. Chen. Neutron-diffraction measurements of magnetic order and a structural transition in the parent $BaFe_2As_2$ compound of FeAs-based high-temperature superconductors. *Phys. Rev. Lett.*, 101:257003, 2008.

[97] J. Fink, S. Thirupathaiah, R. Ovsyannikov, H. A. Dürr, R. Follath, Y. Huang, S. de Jong, M. S. Golden, Yu-Zhong Zhang, H. O. Jeschke, R. Valentí, C. Felser, S. Dastjani Farahani, M. Rotter, and D. Johrendt. Electronic structure studies of $BaFe_2As_2$ by angle-resolved photoemission spectroscopy. *Phys. Rev. B*, 79:155118, 2009.

[98] D. J. Singh. Electronic structure and doping in $BaFe_2As_2$ and LiFeAs: Density functional calculations. *Phys. Rev. B*, 78:094511, 2008.

[99] M. Yi, D. Lu, J.-H. Chu, J. G. Analytis, A. P. Sorini, A. F. Kemper, B. Moritz, S.-K. Mo, R. G. Moore, M. Hashimoto, W.-S. Lee, Z. Hussain, T. P. Devereaux, I. R Fisher, and Z-X Shen. Symmetry-breaking orbital anisotropy observed for detwinned $Ba(Fe_{1-x}Co_x)_2As_2$ above the spin density wave transition. *Proceedings of the National Academy of Sciences*, 108(17):6878, 2011.

[100] E.C. Blomberg, M.A. Tanatar, R.M. Fernandes, I. I. Mazin, B. Shen, H.-H. Wen, M.D. Johannes, J. Schmalian, and R. Prozorov. Sign-reversal of the in-plane resistivity anisotropy in hole-doped iron pnictides. *Nature Comm.*, 4:1914, 2013.

[101] X. Lu, J. T. Park, R. Zhang, H. Luo, A. H. Nevidomskyy, Q. Si, and P. Dai. Nematic spin correlations in the tetragonal state of uniaxial-strained $Ba(Fe_{2-x}Ni_x)_2As_2$. *Science*, 345:657, 2014.

[102] D. K. Pratt, W. Tian, A. Kreyssig, J. L. Zarestky, S. Nandi, N. Ni, S. L. Bud'ko, P. C. Canfield, A. I. Goldman, and R. J. McQueeney. Coexistence of competing antiferromagnetic and superconducting phases in the underdoped $Ba(Fe_{0.953}Co_{0.047})_2As_2$ compound using x-ray and neutron scattering techniques. *Phys. Rev. Lett.*, 103:087001, 2009.

[103] T. Goltz, V. Zinth, D. Johrendt, H. Rosner, G. Pascua, H. Luetkens, P. Materne, and H.-H. Klauss. Microscopic coexistence of magnetism and superconductivity in charge-compensated $Ba_{1-x}K_xFe_{1-y}Co_y)_2As_2$. *Phys. Rev. B*, 89:144511, Apr 2014.

[104] V. Brouet, M. Marsi, B. Mansart, A. Nicolaou, A. Taleb-Ibrahimi, P. Le Fèvre, F. Bertran, F. Rullier-Albenque, A. Forget, and D. Colson. Nesting between hole and electron pockets in $Ba(Fe_{1-x}Co_x)_2As_2$ ($x = 0 - 0.3$) observed with angle-resolved photoemission. *Phys. Rev. B*, 80:165115, 2009.

[105] M. Yi, Y. Zhang, Z.-K. Liu, X. Ding, J.-H. Chu, A. F. Kemper, N. Plonka, B. Moritz, M. Hashimoto, S.-K. Mo, Z. Hussain, T. P. Devereaux, I. R. Fisher, H. H. Wen, Shen Z.-X., and D. H. Lu. Dynamic competition between spin-density wave order and superconductivity in underdoped $Ba_{1-x}K_xFe_2As_2$. *Nat. Comm.*, 5:3711, 2014.

[106] P. Fazekas and E. Tosatti. Electrical, structural and magnetic properties of pure and doped 1T-TaS_2. *Phil. Mag. B*, 39:229, 1979.

[107] R. E. Thomson, B. Burk, A. Zettl, and John Clarke. Scanning tunneling microscopy of the charge-density-wave structure in 1T-TaS_2. *Phys. Rev. B*, 49:16899, 1994.

[108] B. Burk, R. E. Thomson, A. Zettl, and John Clarke. Charge-density-wave domains in 1T-TaS_2 observed by satellite structure in scanning-tunneling-microscopy images. *Phys. Rev. Lett.*, 66:3040, 1991.

[109] L. Perfetti, T. A. Gloor, F. Mila, H. Berger, and M. Grioni. Unexpected periodicity in the quasi-two-dimensional Mott insulator 1T-TaS_2 revealed by angle-resolved photoemission. *Phys. Rev. B*, 71:153101, 2005.

[110] M. Arita, H. Negishi, K. Shimada, F. Xu, A. Ino, Y. Takeda, K. Yamazaki, A. Kimura, S. Qiao, S. Negishi, M. Sasaki, H. Namatame, and M. Taniguchi. Photoemission study of valence band dispersions in charge density wave material 1T-TaS_2. *Physica B: Condensed Matter*, 351:265, 2004.

[111] K. Rossnagel and N. V. Smith. Spin-orbit coupling in the band structure of reconstructed 1T-TaS_2. *Phys. Rev. B*, 73:073106, 2006.

[112] B. Dardel, M. Grioni, D. Malterre, P. Weibel, Y. Baer, and F. Lévy. Spectroscopic signatures of phase transitions in a charge-density-wave system: 1T-TaS_2. *Phys. Rev. B*, 46:7407, 1992.

[113] T. Ritschel, J. Trinckauf, K. Koepernik, B. Büchner, M. v. Zimmermann, H. Berger, Y. I. Joe, P. Abbamonte, and J. Geck. Orbital textures and charge density waves in transition metal dichalcogenides. *Nature Physics*, 11:328, 2015.

[114] P. S. Kirchmann. *Ultrafast electron dynamics in low dimensional materials*. PhD thesis, Freie Universität Berlin, 2008.

[115] S. Freutel. *Transiente Änderungen der elektronischen Struktur von $Bi_2Sr_2CaCu_2O_{8+\delta}$*. PhD thesis, Universität Duisburg-Essen, 2015.

[116] M. Sandhofer. *Elektron-Phonon Kopplung und impulsaufgelöste elektronische Eigenschaften des Pb/Si(111) Hybridsystems*. PhD thesis, Universität Duisburg-Essen, 2015.

[117] Coherent. *Operator's Manual, Verdi V-18 Diode-Pumped Lasers*. Operator's Manual, Verdi V-18 Diode-Pumped Lasers, 2007.

[118] Coherent. *Micra-5 Laser Operator's Manual*. Santa Clara, CA 95054 USA, 2009.

[119] Coherent. *RegA Model 9000 Laser Operator's Manual*. Santa Clara, CA 95054 USA, 1997.

[120] C. Rullière. *Laser Spectroscopy*. Springer, Berlin, 1998.

[121] P. S. Kirchmann, L. Rettig, D. nandi, U. Lipowski, M. Wolf, and U. Bovensiepen. A time-of-flight spectrometer for angle-resolved detection of low energy electrons in two dimensions. *Appl. Phys. A*, 91:211, 2008.

[122] B. Mansart, D. Boschetto, A. Savoia, F. Rullier-Albenque, A. Forget, D. Colson, A. Rousse, and M. Marsi. Observation of a coherent optical phonon in the iron pnictide superconductor $Ba(Fe_{1-x}Co_x)_2As_2$ ($x =$ 0.06 and 0.08). *Phys. Rev. B*, 80:172504, 2009.

[123] B. Mansart, D. Boschetto, A. Savoia, F. Rullier-Albenque, F. Bouquet, E. Papalazarou, A. Forget, D. Colson, A. Rousse, and M. Marsi. Ultrafast transient response and electron-phonon coupling in the iron-pnictide superconductor $Ba(Fe_{1-x}Co_x)_2As_2$. *Phys. Rev. B*, 82:024513, 2010.

[124] L. Stojchevska, P. Kusar, T. Mertelj, V. V. Kabanov, X. Lin, G. H. Cao, Z. A. Xu, and D. Mihailovic. Electron-phonon coupling and the charge gap of spin-density wave iron-pnictide materials from quasiparticle relaxation dynamics. *Phys. Rev. B*, 82:012505, 2010.

[125] T. Mertelj, P. Kusar, V. V. Kabanov, L. Stojchevska, N. D. Zhigadlo, S. Katrych, Z. Bukowski, J. Karpinski, S. Weyeneth, and D. Mihailovic. Quasiparticle relaxation dynamics in spin-density-wave and superconducting $SmFeAsO_{1-x}F_x$ single crystals. *Phys. Rev. B*, 81:224504, 2010.

[126] Elbert E. M. Chia, D. Talbayev, Jian-Xin Zhu, H. Q. Yuan, T. Park, J. D. Thompson, C. Panagopoulos, G. F. Chen, J. L. Luo, N. L. Wang, and A. J. Taylor. Ultrafast pump-probe study of phase separation and

competing orders in the underdoped (Ba,K)Fe_2As_2 superconductor. *Phys. Rev. Lett.*, 104:027003, 2010.

[127] L. Rettig, R. Cortés, H. S. Jeevan, P. Gegenwart, T. Wolf, J. Fink, and U. Bovensiepen. Electron-phonon coupling in 122 Fe pnictides analyzed by femtosecond time-resolved photoemission. *New Journal of Physics*, 15:083023, 2013.

[128] I. Avigo, S. Thirupathaiah, M. Ligges, T. Wolf, J. Fink, and U. Bovensiepen. Doping dependence and electroncboson coupling in the ultrafast relaxation of hot electron populations in $Ba(Fe_{1-x}Co_x)_2As_2$. *New Journal of Physics*, 18:093028, 2016.

[129] C. Liu, T. Kondo, R. M. Fernandes, A. D. Palczewski, E. D. Mun, N. Ni, A. N. Thaler, A. Bostwick, E. Rotenberg, J. Schmalian, S. L. Bud'ko, P. C. Canfield, and A. Kaminski. Evidence for a Lifshitz transition in electron-doped iron arsenic superconductors at the onset of superconductivity. *Nature Physics*, 6:419, 2010.

[130] S. Thirupathaiah, E. D. L. Rienks, H. S. Jeevan, R. Ovsyannikov, E. Slooten, J. Kaas, E. van Heumen, S. de Jong, H. A. Dürr, K. Siemensmeyer, R. Follath, P. Gegenwart, M. S. Golden, and J. Fink. Dissimilarities between the electronic structure of chemically doped and chemically pressurized iron pnictides from an angle-resolved photoemission spectroscopy study. *Phys. Rev. B*, 84:014531, 2011.

[131] A. Koitzsch, D. Inosov, J. Fink, M. Knupfer, H. Eschrig, S. V. Borisenko, G. Behr, A. Köhler, J. Werner, B. Büchner, R. Follath, and H. A. Dürr. Valence-band and core-level photoemission spectroscopy of $LaFeAsO_{1-x}F_x$. *Phys. Rev. B*, 78:180506, Nov 2008.

[132] M. Neupane, P. Richard, Y.-M. Xu, K. Nakayama, T. Sato, T. Takahashi, A. V. Federov, G. Xu, X. Dai, Z. Fang, Z. Wang, G.-F. Chen, N.-L. Wang, H.-H. Wen, and H. Ding. Electron-hole asymmetry in the superconductivity of doped $BaFe_2As_2$ seen via the rigid chemical-potential shift in photoemission. *Phys. Rev. B*, 83:094522, 2011.

[133] S. Ideta, T. Yoshida, I. Nishi, A. Fujimori, Y. Kotani, K. Ono, Y. Nakashima, S. Yamaichi, T. Sasagawa, M. Nakajima, K. Kihou, Y. Tomioka, C. Lee, A. Iyo, H. Eisaki, T. Ito, S. Uchida, and R. Arita. Dependence of carrier doping on the impurity potential in transition-metal-substituted FeAs-based superconductors. *Phys. Rev. Lett.*, 110:107007, 2013.

[134] M. Rotter, M. Tegel, D. Johrendt, I. Schellenberg, W. Hermes, and R. Pöttgen. Spin-density-wave anomaly at 140 K in the ternary iron arsenide $BaFe_2As_2$. *Phys. Rev. B*, 78:020503, 2008.

[135] C. Liu, A. D. Palczewski, R. S. Dhaka, Takeshi Kondo, R. M. Fernandes, E. D. Mun, H. Hodovanets, A. N. Thaler, J. Schmalian, S. L. Bud'ko, P. C. Canfield, and A. Kaminski. Importance of the Fermi-surface topology to the superconducting state of the electron-doped pnictide $Ba(Fe_{1-x}Co_x)_2As_2$. *Phys. Rev. B*, 84:020509, 2011.

[136] J. Fink. Influence of Lifshitz transitions and correlation effects on the scattering rates of the charge carriers in iron-based superconductors. *EPL*, 113:27002, 2016.

[137] M. Lisowski, P. A. Loukakos, U. Bovensiepen, and M. Wolf. Femtosecond dynamics and transport of optically excited electrons in epitaxial Cu films on Si(111)-7x7. *Appl. Phys. A*, 79:739, 2004.

[138] U. Bovensiepen. Coherent and incoherent excitations of the Gd(0001) surface on ultrafast timescales. *Journal of Physics: Condensed Matter*, 19:083201, 2007.

[139] M. Ligges, I. Rajkovic, P. Zhou, O. Posth, C. Hassel, G. Dumpich, and D. von der Linde. Observation of ultrafast lattice heating using time resolved electron diffraction. *Appl. Phys. Lett.*, 94:101910, 2009.

[140] S.-L. Yang, J. A. Sobota, D. Leuenberger, Y. He, M. Hashimoto, D. H. Lu, H. Eisaki, P. S. Kirchmann, and Z.-X. Shen. Inequivalence of single-particle and population lifetimes in a cuprate superconductor. *Phys. Rev. Lett.*, 114:247001, 2015.

[141] J. J. Quinn and R. A. Ferrell. Electron self-energy approach to correlation in a degenerate electron gas. *Phys. Rev.*, 112:812, 1958.

[142] S. Kasahara, T. Shibauchi, K. Hashimoto, K. Ikada, S. Tonegawa, R. Okazaki, H. Shishido, H. Ikeda, H. Takeya, K. Hirata, T. Terashima, and Y. Matsuda. Evolution from non-Fermi- to Fermi-liquid transport via isovalent doping in $BaFe_2(As_{1-x}P_x)_2$ superconductors. *Phys. Rev. B*, 81:184519, 2010.

[143] L. W. Harriger, H. Q. Luo, M. S. Liu, C. Frost, J. P. Hu, M. R. Norman, and P. Dai. Nematic spin fluid in the tetragonal phase of $BaFe_2As_2$. *Phys. Rev. B*, 84:054544, 2011.

[144] A. Patz, T. Li, S. Ran, R. M. Fernandes, J. Schmalian, S. L. Bud'ko, P. C. Canfield, I. E. Perakis, and J. Wang. Ultrafast observation of critical nematic fluctuations and giant magnetoelastic coupling in iron pnictides. *Nature Communication*, 5(3229), 2014.

[145] A. A. Kordyuk, V. B. Zabolotnyy, D. V. Evtushinsky, A. N. Yaresko, B. Büchner, and S. V. Borisenko. Electronic band structure of ferro-

pnictide superconductors from ARPES experiment. *J Supercond Nov Magn*, 26:2837, 2013.

[146] M. Sentef, A. F. Kemper, B. Moritz, J. K. Freericks, Z-X. Shen, and T. P. Devereaux. Examining electron-boson coupling using time-resolved spectroscopy. *Phys. Rev. X*, 3:041033, 2013.

[147] A. F. Kemper, M. A. Sentef, B. Moritz, J. K. Freericks, and T. P. Devereaux. Effect of dynamical spectral weight redistribution on effective interactions in time-resolved spectroscopy. *Phys. Rev. B*, 90:075126, 2014.

[148] S. Engelsberg and J. R. Schrieffer. Coupled electron-phonon system. *Phys. Rev.*, 131:993, 1963.

[149] L. Boeri, O. V. Dolgov, and A. A. Golubov. Is $LaFeAsO_{1-x}F_x$ an electron-phonon superconductor? *Phys. Rev. Lett.*, 101:026403, 2008.

[150] L. Boeri, M. Calandra, I. I. Mazin, O. V. Dolgov, and F. Mauri. Effects of magnetism and doping on the electron-phonon coupling in $BaFe_2As_2$. *Phys. Rev. B*, 82:020506, 2010.

[151] M. Liu, L. W. Harriger, Luo, M. Wang, R. A. Ewings, T. Guidi, H. Park, K Haule, G. Kotliar, S. M. Hayden, and P. Dai. Nature of magnetic excitations in superconducting $BaFe_{1.9}Ni_{0.1}As_2$. *Nature Phys*, 8:376, 2012.

[152] M. Wang, C. Zhang, X. Lu, G. Tan, H. Luo, Y. Song, M. Wang, X. Zhang, E. A. Goremychkin, T. G. Perring, T. A. Maier, Z. Yin, K. Haule, G. Kotliar, and P. Dai. Doping dependence of spin excitations and its correlations with high-temperature superconductivity in iron pnictides. *Nature Communication*, 4, 2874, 2013.

[153] J. Schäfer, D. Schrupp, E. Rotenberg, K. Rossnagel, H. Koh, P. Blaha, and R. Claessen. Electronic quasiparticle renormalization on the spin wave energy scale. *Phys. Rev. Lett.*, 92:097205, 2004.

[154] S. Wall, D. Brida, S. R. Clark, H. P. Ehrke, D. Jaksch, A. Ardavan, S. Bonora, H. Uemura, Y. Takahashi, T. Hasegawa, H. Okamoto, G. Cerullo, and A. Cavalleri. Quantum interference between charge excitation paths in a solid-state Mott insulator. *Nature Phy*, 7:114, 2011.

[155] M. Mitrano, G. Cotugno, S. R. Clark, R. Singla, S. Kaiser, J. Stähler, R. Beyer, M. Dressel, L. Baldassarre, D. Nicoletti, A. Perucchi, T. Hasegawa, H. Okamoto, D. Jaksch, and A. Cavalleri. Pressure-dependent relaxation in the photoexcited mott insulator ET-F_2TCNQ:

Influence of hopping and correlations on quasiparticle recombination rates. *Phys. Rev. Lett.*, 112:117801, 2014.

[156] J. Demsar, L. Forró, H. Berger, and D. Mihailovic. Femtosecond snapshots of gap-forming charge-density-wave correlations in quasi-two-dimensional dichalcogenides 1T-TaS_2 and 2H-$TaSe_2$. *Phys. Rev. B*, 66:041101, 2002.

[157] J. H. Bechtel. Heating of solid targets with laser pulses. *Journal of Applied Physics*, 46:1585, 1975.

[158] M. Ligges, I. Avigo, Golež D., H. Strand, L. Stojchevska, M. Kalläne, K. Rossnagel, M. Eckstein, P. Werner, and U. Bovensiepen. Ultrafast doublon dynamics in photo-excited 1T-TaS_2. *arXiv*, 1702.05300v1, 2017.

[159] I. Avigo, I. Vaskivskyi, M. Ligges, M. Kalläne, K. Rossnagel, L. Stojchevska, D. Mihailovic, and U. Bovensiepen. Accessing and probing of the photoinduced hidden state in 1T-TaS_2 with time- and angle-resolved photoemission spectroscopy. *Proc. of SPIE, Spintronics IX*, 9931:99313V, 2016.

[160] S. Hellmann, M. Beye, C. Sohrt, T. Rohwer, F. Sorgenfrei, H. Redlin, M. Kalläne, M. Marczynski-Bühlow, F. Hennies, M. Bauer, A. Föhlisch, L. Kipp, W. Wurth, and K. Rossnagel. Ultrafast melting of a charge-density wave in the mott insulator 1T-TaS_2. *Phys. Rev. Lett.*, 105:187401, 2010.

[161] A. Yamamoto. Hexagonal domainlike structure in 1T-TaS_2. *Phys. Rev. B*, 27:7823–7826, 1983.

[162] A. R. Beal, H. P. Hughes, and W. Y. Liang. The reflectivity spectra of some group va transition metal dichalcogenides. *Journal of Physics C: Solid State Physics*, 8(24):4236, 1975.

[163] M Eichberg, H. Schäfer, M. Krumova, M. Beyer, J. Demsar, H. Berger, G. Moreira, German Sciaini, and R. J. Dwayne Miller. Snapshots of cooperative atomic motions in the optical suppression of charge density waves. *Nature*, 468:799, 2010.

[164] H. Ueba and B. Gumhalter. Theory of two-photon photoemission spectroscopy of surfaces. *Progress in Surface Science*, 82:193, 2007. Dynamics of Electron Transfer Processes at Surfaces.

[165] T. Hertel, E. Knoesel, M. Wolf, and G. Ertl. Ultrafast electron dynamics at Cu(111): Response of an electron gas to optical excitation. *Phys. Rev. Lett.*, 76:535, 1996.

[166] M. Bauer, A. Marienfeld, and M. Aeschlimann. Hot electron lifetimes in metals probed by time-resolved two-photon photoemission. *Progress in Surface Science*, 90(3):319, 2015.

[167] D. Cho, S. Cheon, K.-S. Kim, S.-H. Lee, Y.-H. Cho, S.-W. Cheong, and H. W. Yeom. Nanoscale manipulation of the Mott insulating state coupled to charge order in 1T-TaS_2. *Nature Comm.*, 7:10453, 2016.

[168] H. Sato, M. Arita, Y. Utsumi, Y. Mukaegawa, M. Sasaki, A. Ohnishi, M. Kitaura, H. Namatame, and M. Taniguchi. Conduction-band electronic structure of 1T-TaS_2 revealed by angle-resolved inverse-photoemission spectroscopy. *Phys. Rev. B*, 89:155137, 2014.

[169] J. Shah. *Ultrafast spectroscopy of semiconductors and semiconductor nanostructures*. Springer, Berlin Heidelberg, 2 edition, 1999.

[170] M. Eckstein and M. Kollar. Measuring correlated electron dynamics with time-resolved photoemission spectroscopy. *Phys. Rev. B*, 78:245113, 2008.

[171] L. V. Gasparov, K. G. Brown, A. C. Wint, D. B. Tanner, H. Berger, G. Margaritondo, R. Gaál, and L. Forró. Phonon anomaly at the charge ordering transition in 1T-TaS_2. *Phys. Rev. B*, 66:094301, 2002.

[172] A. Georges, G. Kotliar, W. Krauth, and M. J. Rozenberg. Dynamical mean-field theory of strongly correlated fermion systems and the limit of infinite dimensions. *Rev. Mod. Phys.*, 68:13, 1996.

[173] P. Werner, K. Held, and M. Eckstein. Role of impact ionization in the thermalization of photoexcited Mott insulators. *Phys. Rev. B*, 90:235102, 2014.

[174] E. Perepelitsky, A. Galatas, J. Mravlje, R. Žitko, E. Khatami, B. S. Shastry, and A. Georges. Transport and optical conductivity in the Hubbard model: A high-temperature expansion perspective. *Phys. Rev. B*, 94:235115, 2016.

[175] T. Endo, S. Nakao, W. Yamaguchi, T. Hasegawa, and K. Kitazawa. Influence of CDW stacking disorder on metal-insulator transition in 1T-TaS_2. *Solid State Communications*, 116:47, 2000.

[176] M. Eckstein and P. Werner. Thermalization of a pump-excited Mott insulator. *Phys. Rev. B*, 84:035122, 2011.

[177] P. Werner and M. Eckstein. Field-induced polaron formation in the Holstein-Hubbard model. *EPL (Europhysics Letters)*, 109:37002, 2015.

[178] M. Eckstein and P. Werner. Ultra-fast photo-carrier relaxation in Mott insulators with short-range spin correlations. *Scientific Reports*, 6:21235, 2016.

[179] M. J. Hollander, Y. Liu, W.-J. Lu, L.-J. Li, Y.-P. Sun, J. A. Robinson, and S. Datta. Electrically driven reversible insulatorcmetal phase transition in 1T-TaS_2. *Nano Lett.*, 15:1861, 2015.

[180] I. Vaskivskyi, I. A. Mihailovic, Brazovskii S., J. Gospodaric, T. Mertelj, P. Svetin, D.and Sutar, and D. Mihailovic. Fast electronic resistance switching involving hidden charge density wave states. *Nature Comm.*, 7:11442, 2016.

[181] M. Yoshida, R. Suzuki, Y. Zhang, M. Nakano, and Y. Iwasa. Memristive phase switching in two-dimensional 1T-TaS_2 crystals. *Science A*, 1:e1500606, 2015.

[182] Y. Toda, K. Tateishi, and S. Tanda. Anomalous coherent phonon oscillations in the commensurate phase of the quasi-two-dimensional 1T-TaS_2 compound. *Phys. Rev. B*, 70:033106, 2004.

[183] T. Onozaki, Y. Toda, S. Tanda, and R. Morita. Coherend double-pulse excitation of charge-density-wave oscillation. *Japanese Journal of Applied Physics*, 46:870, 2007.

List of publications

Publications in the framework of this thesis

I. Avigo, S. Thirupathaiah, E. D. L. Rienks, L. Rettig, A. Charnukha, M. Ligges, R. Cortés, J. Nayak, H. S. Jeevan, T. Wolf, Y. Huang, S. Wurmehl, M. I. Sturza, P. Gegenwart, M. S. Golden, L. X. Yang, K. Rossnagel, M. Bauer, B. Büchner, M. Vojta, M. Wolf, C. Felser, J. Fink, U. Bovensiepen
Electronic structure and ultrafast dynamics of FeAs-based superconductors by angle- and time-resolved photoemission spectroscopy
Phys. Status Solidi B **254**, 1600382 (2017). DOI:10.1002/pssb.201600382

I. Avigo, S. Thirupathaiah, M. Ligges, T. Wolf, J. Fink & U. Bovensiepen
Doping dependence and electron-boson coupling in the ultrafast relaxation of hot electron populations in $Ba(Fe_{1-x}Co_x)_2As_2$
New Journal of Physics **18**, 093028 (2016). DOI:10.1088/1367-2630/18/9/093028

I. Avigo, I. Vaskivskyi, M. Ligges, M. Kalläne, K. Rossnagel, L. Stojchevska, D. Mihailovič & U. Bovensiepen
Accessing and probing of the photoinduced hidden state in $1T$-TaS_2 with time- and angle-resolved photoemission spectroscopy
Proc. of SPIE, Spintronics IX **9931**, 99313V (2016). DOI:10.1117/12.2239258

J. Fink, A. Charnukha, E. D. L. Rienks, Z. H. Liu, S. Thirupathaiah, I. Avigo, F. Roth, H.S. Jeevan, P. Gegenwart, I. Morozov, S. Wurmehl, U. Bovesiepen, S. Borisenko, M. Vojta, & B. Büchner
Non-Fermi-liquid scattering rates and anomalous band dispersion in ferropnictides
Physical Review B **92**, 201106(R) (2015). DOI:0.1103/PhysRevB.92.201106

E.D.L.Rienks, T. Wolf, K. Koepernik, I. Avigo, P. Hlawenka, C. Lupulesco, T. Arion, F. Roth, W. Eberhardt, U. Bovensiepen & J. Fink
Electronic structure and quantum criticality in $Ba(Fe_{1-x-z}Co_xMn_y)_2As_2$, an ARPES study
Europhysics Letters **103**, 47004 (2013). DOI:10.1209/0295-5075/103/47004

I. Avigo, R. Cortés, L. Rettig, S. Thirupathaiah, H. S. Jeevan, P. Gegenwart, T. Wolf, M. Ligges, M. Wolf, J. Fink, & U. Bovensiepen
Coherent excitations and electron phonon coupling in $Ba/EuFe_2As_2$ compounds investigated by femtosecond time- and angle-resolved photoemission spectroscopy
Journal of Physics: Condensed Matter **25**, 094003 (2013). DOI:10.1088/0953-8984/25/9/094003

M. Ligges, I. Avigo, D. Golež, H. Strand, l. Stojchevska, M. Kalläne, K. Rossnagel, M. Eckstein, P. Werner & U. Bovensiepen
Ultrafast dublon dynamics in photo-excited $1T$-TaS_2
submitted to *Physical review letters*
available online at https://arxiv.org/abs/1702.05300v1

Publications concerning other topics

T.Frigge, B. hafke, T. Witte, B. krenzer, C. Streubühr, A. Samad syed, V. Mikšić Trontl, I. Avigo, P. Zhou, M. ligges, D. von der Linde, U. bovensiepen, M. Horn-von hoegen, S. Wippermann, A. Lücke, S. Sanna, U. Gerstmann & W. G. Schmidt
Optically excited structural transitions in atomic wires on surfaces at the quantum limit
In press by *Nature* (2017)

J.D. Rameau, S. Freutel, A. F. Kemper, M. A. Sentef, J. K. Freericks, I. Avigo, M. Ligges, L. Rettig, Y. Yoshida, H. Eisaki, J. Shneeloch, R. D. Zhong, Z. J. Xu, G. D. Gu, P. D. Johnson & U. Bovensiepen
Energy dissipation from a correlated system driven out of equilibrium
Nature Communications 7, 13761 (2016). DOI:10.1038/ncomms13761

A. Samad Syed, V. Mikšić Trontl, M. Ligges, S. Sakong, P. Kratzer, D. Lükermann, P. Zhou, I. Avigo, H. Pfnür, C. Tegenkamp & U. Bovensiepen, Unoccupied electronic structure and momentum-dependent scattering dynamics in Pb/Si(557) nanowire arrays
Physical Review B **92**, 134301 (2015). DOI:10.1103/PhysRevB.92.134301

J. D. Rameau, S. Freutel, L. Rettig, I. Avigo, M. Ligges, Y. Yoshida, H. Eisaki, J. Schneeloch, R. D. Zhong, Z. J. Xu, G. D. Gu, P. D. Johnson & U. Bovensiepen
Photoinduced changes in the cuprate electronic structure revealed by femtosecond time- and angle-resolved photoemission
Physical Review B **89**, 115115 (2014)

Acknowledgements

Such a work wouldn't have been possible without the help and support of many people, to whom this section is dedicated and to whom I am happy to give credits.
At first I would like to thank my supervisor Uwe Bovensiepen, who gave me the possibility of working in his group and finally obtain my PhD. Thank you Uwe for your support, especially during my pregnancy and the year I spent home, which obviously delayed the conclusion of this route. You have always been kind and comprehensive with me and I really appreciate that. Thank you also for all the discussions, exchange of ideas and even for the hard times when you were pushing me, because without a big efforts, one cannot reach big results.
A very special thank goes to Manuel Ligges, for the huge support not only from the scientific but also human point of you. You always had interesting and useful scientific advices and inputs from which I always profited and learnt. I, together with the other "mates", always had great times with you and even when everything seemed dark and the difficulties impossible to overcome, you were always there dedicating at least few minutes of your (always very precious and limited) time to talk to us and try to find a way out.
I am very grateful to Laurenz Rettig, who was on his way of finishing his PhD when I was starting mine and although it was a very busy and hectic time for him, he was available to share his experience and deep knowledge of the experimental setup with us, providing all the basics from where to start with.
I would like to thank Jörg Fink, with whom I spent two beam times at Bessi II, for the successful collaboration on the iron pnictides project and the exciting discussions. Special thanks go to Setti Thirupathaiah, whose support during the trARPES measurements on the iron pnictides was really precious, and to Igor Vaskivskyi who joined us for a couple of weeks in Duisburg to help us performing the switching experiment on $1T$-TaS_2. I really had a great time with you guys, thanks.
Very special thanks go to my former colleagues from the photoemission team, Simon, Mathias and Ishita for the support, the discussions and the really nice time spent together inside and outside of the lab. Thanks to

all the members of the AG Bovensiepen, also the one who already left, and in particular Ping, Mehdi, Frank, Jens, Florian, Carla, Mathieu, Samad, Andrea and Klaus.
A special thank to Federica and her beautiful family. I really appreciate the help you gave me in taking care of Sóley, when I needed to spend few hours more working on this dissertation. Grazie.
Finally my infinite gratitude goes to my parents, my beloved husband and my little Sóley for all the support and love which I always received even in the darkest moments when I was about to give up. Grazie infinite, vi amo con tutto il cuore.